5-2021

Process-Structure-Property Relationships in 3D-Printed Epoxy Composites Produced via Material Extrusion Additive Manufacturing

Nadim S. Hmeidat
University of Tennessee, Knoxville, nhmeidat@vols.utk.edu

To the Graduate Council:

I am submitting herewith a dissertation written by Nadim S. Hmeidat entitled "Process-Structure-Property Relationships in 3D-Printed Epoxy Composites Produced via Material Extrusion Additive Manufacturing." I have examined the final electronic copy of this dissertation for form and content and recommend that it be accepted in partial fulfillment of the requirements for the degree of Doctor of Philosophy, with a major in Mechanical Engineering.

Brett G. Compton, Major Professor

We have read this dissertation and recommend its acceptance:

Uday Vaidya, Chad Duty, Claudia J. Rawn

Accepted for the Council:

Dixie L. Thompson

Vice Provost and Dean of the Graduate School

(Original signatures are on file with official student records.)

Process-Structure-Property Relationships in 3D-Printed Epoxy Composites Produced via Material Extrusion Additive Manufacturing

A Dissertation Presented for the

Doctor of Philosophy

Degree

The University of Tennessee, Knoxville

Nadim S. Hmeidat

May 2021

Dedication

I dedicate this doctoral dissertation to my precious parents, Saleh and Eman Hmeidat, who have sacrificed so much for me and supported me all through my life. I am deeply grateful for their support, love and sacrifices.

to my beautiful, lovely wife, Rufaida, who has continually supported, motivated and encouraged me to be where I am today, and whom I am happy to share life with.

to my gorgeous son, Eyas, who has been the greatest friend and constant source of joy during the last two years of this PhD journey,

to my beloved siblings, Amal, Marah, Shatha, Dr. Mohammed, Waseem and Ahmed, who have believed in me unconditionally and never left my side,

and finally to my beloved uncles, Mr. Qaseem Aburish and Dr. Mahmoud Aburish-Hmidat, who have inspired me to achieve my educational goals.

Acknowledgments

First and foremost, praises and thanks to the God, Almighty, for His showers of blessings throughout my academic life and for giving me strength and ability to complete this work successfully.

This work would not have been possible without the efforts, support and guidance of many people. I foremost must acknowledge and thank my advisor, Prof. Brett G. Compton. Throughout my time at the University of Tennessee (UTK), Prof. Compton has offered an abundance of teaching, support and guidance, for which I am truly grateful. His success, work style and mentoring has always inspired me and helped me to become self-motivated and hard-working. I am also thankful to him for giving me opportunities to work on several projects, which helped me grow as a researcher and become more independent. I am proud to call myself a Compton group member and I am blessed to have found such a remarkable advisor and friend. I sincerely thank the distinguished members of my committee, including Prof. Uday Vaidya, Prof. Chad Duty and Prof. Claudia Rawn, for their willingness to serve in this capacity, and for their helpful comments to improve this work.

Special thanks to my lab mates, Cody Pack, Willie Kemp, Stian Romberg, Madeline Wimmer for all the helpful discussions and support throughout my PhD journey. Thank you to both Daniel Elkins and Hutch Peter for their help in taking the fiber length measurements, and to Jackson Wilt for his help with the COMSOL analysis associated with this project.

I am very thankful to Dr. Hicham Ghossein, Dr. Philip Barnett, Dr. Christine Ajinjeru, Dr. Vidya Kishore, Dylan Hoskins, and James Brackett for the helpful discussions during my time at UTK, Jake Dvorak and Zane Palmer for their timely help with sample machining.

I would also like to acknowledge my collaborators Dr. Edward Trigg, Dr. Hilmar Koerner from Air Force Research Laboratory (AFRL), Dr. Louisa Smieska, Dr. Arthur Woll from

Cornell University, and Dr. Samantha Talley and Dr. Robert Moore from Virginia Tech University for their invaluable assistance with the X-ray scattering work of this project. I would also like to acknowledge Dr. Vipin Kumar from Oak Ridge National Laboratory for providing the X-ray computed tomography analysis of this project.

My time and research at UTK have been generously supported by a few organizations that I would like to gratefully acknowledge here. This dissertation research was sponsored by the University of Tennessee, the UT Science Alliance through the Joint Directed Research and Development Program (JDRD), Honeywell Federal Manufacturing and Technologies through Contract DE-NA0002839, administrated by Dr. Jamie Messman, Mr. Steven Patterson, and Dr. Eric Eastwood. Part of the dissertation research was funded by the National Science Foundation (NSF) under grant no. CMMI-1825815. I also received partial support from the Tennessee Higher Education Commission Center for Materials Processing.

I would like to thank the administrative personnel in the MABE department at UTK for their ample logistical support during my PhD journey. This especially includes Tammy Johnson, Rhnea Reagan, Ruthann Moyers, Callie Laughlin, Ryan Wilhite and Julie Knoefel.

Finally, to all those I have unintentionally left out that have helped and supported me along the way, I thank you.

Abstract

Extrusion-based additive manufacturing (AM) technologies, such as direct ink writing (DIW), offer unique opportunities to create composite materials and novel multi-material architectures that are not feasible using other AM technologies. DIW is a novel 3D-printing approach in which viscoelastic inks, with favorable rheological properties, are extruded through fine nozzles and patterned in a filament form at room temperature.

Recent developments in DIW of polymer composites have led to expanding the range of materials used for printing, as well as introducing novel deposition strategies to control filler orientation and create improved functional/structural composite materials. Despite these substantial advancements, the successful and optimal utilization of any AM technology necessitates a deeper understanding of the process-structure-property relationships for each material system employed. To shed light onto the process-structure-property relationship in 3D-printed polymer composites, this dissertation focuses on understanding relationships between ink composition (i.e., filler morphology and loading), ink processing conditions, ink rheology, printing parameters (i.e., nozzle size and print speed), filler orientation/arrangements, and mechanical properties in 3D-printed epoxy-based composites produced via DIW.

In this work, printable epoxy-based composite inks have been developed for DIW utilizing filler materials with different morphologies, including nanoclay (NC) platelets, fumed-silica (FS) spheroidal nanoparticles, silicon carbide (SiC) whiskers and chopped-carbon-fibers (CFs). First, the rheological requirements for successful DIW are studied using an epoxy/NC system as a model material, and the effects of the deposition process on the arrangements of NC platelets and mechanical anisotropy in 3D-printed nanocomposites are investigated. Second, the impact of filler morphology and printing parameters on the extent of mechanical

anisotropy and filler orientation in 3D-printed composites are explored. Third, the effects of the ink formulation and processing parameters on the evolution of fiber length distribution (FLD) and mechanical behavior of 3D-printed CF composites are investigated. Furthermore, the effects of printing parameters on mechanical anisotropy and fiber orientation distribution (FOD) in 3D-printed CF composites are explored.

Overall, this work provides a broad framework for enabling more rigorous engineering design of 3D-printed polymer composites via material extrusion AM, as well as guiding the optimal selection of processing/printing parameters that govern microstructure and performance in 3D-printed polymer composites.

Table of Contents

1 Motivation, Objectives and Thesis Outline **1**

1.1 Motivation 2

1.2 Objectives 4

1.3 Thesis Outline 5

2 Introduction **7**

2.1 Additive Manufacturing 8

2.2 Polymer AM technologies 8

2.3 Extrusion-based polymer AM 10

2.3.1 Fused filament fabrication (FFF) and its composites 10

2.3.2 Direct ink writing (DIW) 13

2.4 DIW requirements 15

2.4.1 Ink rheology 15

2.4.2 Filler materials 17

2.5 3D-printed thermoset composites and mechanical properties 18

2.6 Filler alignment and anisotropy 23

3 Effects of DIW deposition on filler arrangements and mechanical anisotropy in 3D-printed epoxy nanocomposites **26**

3.1 Abstract 27

3.2 Introduction 28

3.3 Experimental 32

3.3.1 Materials 32

3.3.2 Ink formulations . . . 32
3.3.3 3D printing . . . 33
3.3.4 Ink rheology . . . 35
3.3.5 Thermal characterization . . . 36
3.3.6 Mechanical characterization . . . 36
3.3.7 Microscopic characterization . . . 37
3.4 Results and Discussion . . . 37
3.4.1 Ink rheology . . . 37
3.4.2 3D printing and sample fabrication . . . 40
3.4.3 Mechanical behavior . . . 45
3.4.4 Thermal behavior . . . 49
3.4.5 Anisotropy due to printing . . . 57
3.4.6 NC arrangements . . . 61
3.5 Summary and Conclusions . . . 64
3.6 Acknowledgements . . . 66

4 Effects of filler morphology, nozzle size and print speed on mechanical anisotropy in 3D-printed epoxy composites 67

4.1 Abstract . . . 68
4.2 Introduction . . . 69
4.3 Experimental Details . . . 73
4.3.1 Materials . . . 73
4.3.2 Formulation . . . 75
4.3.3 Ink rheology . . . 75
4.3.4 3D-printing and curing schedule . . . 78
4.3.5 Mechanical testing . . . 79
4.3.6 Microscopy . . . 79
4.3.7 X-ray scattering . . . 80
4.4 Results . . . 80
4.4.1 Rheological behavior and printing . . . 80

4.4.2 Mechanical behavior . . . 82
4.4.3 Microscopic characterization . . . 88
4.4.4 X-ray scattering . . . 91
4.5 Analysis and Discussion . . . 95
4.5.1 Rheology of composite inks . . . 95
4.5.2 Anisotropy master curves . . . 95
4.5.3 Interaction between fillers . . . 99
4.6 Summary and Conclusions . . . 100
4.7 Acknowledgments . . . 102

5 Processing and mechanical characterization of carbon fiber – reinforced epoxy composites for material extrusion additive manufacturing 103
5.1 Abstract . . . 104
5.2 Introduction . . . 104
5.3 Experimental . . . 109
5.3.1 Materials . . . 109
5.3.2 Ink formulation . . . 109
5.3.3 Fiber length measurements . . . 110
5.3.4 Ink rheology . . . 112
5.3.5 3D printing . . . 112
5.3.6 Mechanical characterization . . . 114
5.3.7 Microscopy . . . 115
5.3.8 X-ray computed tomography . . . 115
5.4 Results and Discussion . . . 116
5.4.1 Fiber length evolution in CF inks . . . 116
5.4.2 Fiber length evolution in CF/NC inks . . . 119
5.4.3 Rheological behavior . . . 121
5.4.4 Printing behavior . . . 124
5.4.5 Mechanical behavior vs. mixing time . . . 125
5.4.6 Microscopy . . . 129

5.4.7 Mechanical property prediction vs. mixing time . . . 132
5.4.8 Mechanical anisotropy . . . 135
5.4.9 Fiber orientation distribution . . . 140
5.5 Summary and Conclusions . . . 142
5.6 Acknowledgments . . . 143

6 Conclusions **144**
6.1 Overall conclusions . . . 145
6.2 Mechanical properties . . . 149
6.3 Publications . . . 151

Bibliography **153**

Appendices **170**
A Supplemental Information . . . 171
A.1 Rheological and printing behavior of epoxy/fumed silica inks . . . 171
A.2 Finite-element-based COMSOL analysis . . . 174
A.3 Print paths . . . 177
A.4 Rheology of single-filler ink materials . . . 178
A.5 Extrusion pressure values – Chapter 4 . . . 180
A.6 Fracture surfaces . . . 181
A.7 Polarized optical microscopy (POM) of epoxy/fumed silica 3D-printed composites . . . 182
A.8 Annular average of 2D scattering pattern . . . 183
A.9 Scanning electron microscopy of carbon fiber bundles . . . 184
A.10 Fiber length measurements . . . 185
A.11 Extrusion pressure values – Chapter 5 . . . 186
A.12 Density of printed epoxy/CF/NC composites vs. mixing time . . . 187
A.13 Weibull fit parameters . . . 188
A.14 Linear fitting parameters for the plots in Figure A.13– Chapter 5 . . . 189
A.15 Anisotropy master curves . . . 190

A.16 Fiber orientation distribution (FOD) 191

Vita **192**

List of Tables

2.1 Composition and mechanical properties of epoxy-based fiber-reinforced composites produced via DIW 21

3.1 Compositions of epoxy/NC formulations 34
3.2 Rheological properties of epoxy/NC formulations 41
3.3 Mechanical properties of cast and 3D-printed epoxy nanocomposites 47
3.4 Thermogravimetric data for epoxy/NC composites in air atmospheres 53
3.5 Thermogravimetric data for epoxy/NC composites in nitrogen atmospheres . 53

4.1 Properties and morphology of individual ink constituents 76
4.2 Composition of inks formulated for direct ink writing 77
4.3 Flexural properties of FS– and NC–based 3D-printed specimens 86
4.4 Flexural properties of SiC–based 3D-printed specimens 87
4.5 Herman's orientation factor, f_x, in NC-containing composites 94
4.6 Fitting parameters for power law anisotropy model 98

5.1 Compositions of epoxy/CF ink formulations 111
5.2 Volume averaged fiber length and Weibull distribution parameters for all inks formulated 113
5.3 Effect of mixing time on the rheological properties of epoxy/NC and epoxy/NC/CF inks 123
5.4 Flexural properties of printed epoxy/NC/CF composites at different mixing times 128
5.5 Properties of composite constituents 134

5.6 Flexural properties of printed epoxy/NC/CF composites at different print parameters 139

A.1 Rheological properties of epoxy/FS ink formulations 172

A.2 Extrusion pressure values for each material system and print parameters . . 180

A.3 Extrusion pressure values for the NC/CF ink at different mixing time and print parameters 186

A.4 Linear fitting parameters for the plots in Figure A.13 189

A.5 Fiber orientation, fiber count and relative frequency distribution in printed NC/CF composites printed at $\nu/D = 9.6$ s^{-1} and $\nu/D = 65.7$ s^{-1}. 191

List of Figures

2.1 CAD model of a teacup with further images showing how additive manufacturing works [123] 9

2.2 Schematic illustration of the fused filament fabrication (FFF) technology [65] 11

2.3 Schematic illustration of direct ink writing (DIW) technology 14

2.4 DIW rheological requirements: (a) viscosity as a function of shear rate and (b) log-log plots of storage and loss moduli as a function of shear stress for Newtonian and shear-thinning ink fluids 16

2.5 Property space map of strength versus modulus for 3D-printed fiber-reinforced epoxy composites fabricated via DIW [14, 91, 22, 18, 77, 92, 83, 84]. 20

2.6 (a) Schematic illustration of the alignment of high-aspect-ratio fillers within the nozzle during DIW deposition, and (b) epoxy/SiC/Carbon-fiber printed walls, revealing highly oriented carbon fibers oriented in the print direction. Adapted from [22]. 24

3.1 (a) Schematic illustration of direct ink writing 3D-printing. (b) 3D-printed epoxy/NC rectangular specimens for both flexural and DMA test characterization, with transverse specimens on the left and longitudinal specimens on the right. (c) 3D-printed University of Tennessee logo with honeycomb infill. (d) Top, side, and end view optical micrographs of a transverse flexure specimen printed using the 12.5 wt.% NC ink formulation. 30

3.2 Rheological behavior of all epoxy/NC formulations investigated. (a) Log-log plots of apparent viscosity as a function of shear rate. (b) The shear thinning exponent, n, and the consistency index, K, computed by fitting the linear portions of the viscosity curves in (a) with the power-law fluid model described by equation (1). (c) Log-log plots of storage and loss moduli as a function of oscillatory shear stress. (d) The plateau elastic modulus and the shear yield stress values for each formulation, measured from (c). 38

3.3 Optical micrographs of the as-printed ends of representative longitudinal flexural bars along with corresponding optical micrographs of cross-sections of the same bars. (a) and (d) contain 7.5 wt.% NC, (b) and (e) contain 10 wt.% NC, and (c) and (f) contain 12.5 wt.% NC. These micrographs demonstrate that all formulations can form fully dense components without any voids trapped between filaments. 42

3.4 Optical micrographs showing printing-related voids in a longitudinal flexure specimen containing 12.5 wt.% NC. (a) Low-mag image of the fracture surface of a pore-free sample. (b) Low-mag image of the fracture surface of a sample containing a regular array of interfilamentary voids resulting from a lower ink flow rate during printing. (c) High-mag micrograph of the pore-free surface shown in (a). (d) High-mag micrograph of the surface containing voids. The approximate filament size is indicated by the white oval. Empty pores are indicated with red arrows, while filled pores are indicated with black arrows. 44

3.5 Bar plots of the average values of (a) flexural modulus, (b) flexural strength and (c) strain-to-failure for all tested specimens. The room temperature storage modulus values measured by DMA are also shown in (a) for comparison. The flexural properties of the epoxy/FS printed specimens are also shown on the right side of the bar plots, indicated by FS. Error bars indicate the standard deviation in measured values 46

3.6 (a) Optical image of the end view of a printed epoxy/NC/Amicure single-road. The black boxes denote the regions of interest for nanoindentation testing. (b) Elastic modulus values of 20 x 20 indentations separated by 5 μm. (c) Elastic modulus values of 2 x 9 indentations separated by 40 μm. The single-road was printed at a print speed of 20 mm/s using a nozzle diameter of 609 μm. 48

3.7 Optical micrographs of representative fracture surfaces of cast and printed flexure specimens containing (a) 0 wt.%, (b) 2.5 wt.%, (c) 5 wt.%, (d) and (g) 7.5wt.%, (e) and (h) 10 wt.%, and (f) and (i) 12.5 wt.% NC. No inter-filamentary voids are observed, indicating complete coalescence of printed filaments. 50

3.8 Scanning electron micrographs showing features of the point of failure initiation on the fracture surfaces of (a) a longitudinal specimen containing 10 wt.% NC, (b) a transverse specimen containing 10 wt.% NC, (c) a longitudinal specimen containing 10 wt.% FS, and (d) a transverse specimen containing 10 wt.% FS. 51

3.9 Thermograms and primary derivative plots for the epoxy/NC formulations in (a) and (b) air, and (c) and (d) nitrogen atmospheres. 52

3.10 3-pt. flexure DMA measurements. (a) Representative storage moduli as a function of temperature for all epoxy/NC formulations. (b) The corresponding loss tangent curves. 55

3.11 Glass transition temperatures, T_g, measured from the peak of the loss tangent curves. 56

3.12 Optical transmitted light micrographs for polished thin slices (< 1 mm thick) cut from cast and printed specimens. (a) 0 wt.% cast, (b) 2.5 wt.% cast, (c) 5 wt.% cast, (d) 5 wt.% printed, (e) 7.5 wt.% printed, (f) 10 wt.% printed, (g) 12.5 wt.% printed epoxy/NC, and (h) 10 wt.% FS, printed. The left-hand column shows normal transmitted light, while the right-hand column shows the same samples observed using crossed polarizers. The patterned birefringence observed in (d)-(g) is indicative of preferred orientation in the NC as a result of the printing process. 58

3.13 Optical microscopy images in cross-polarized light mode (transmission) of thin slices printed with NC/Amicure: (a) a slice of a single-road cut from a printed log-pile structure encased in an epoxy resin, and (b) a slice of multiple overlapped roads cut from a printed flexural bar as in Figure 4.6. The optical micrographs in (b) are taken at 0°, 20°, 30°, 45° orientation angles relative to the orientation direction of the polarizer. All specimens were printed with a nozzle diameter of 609 μm at a print speed of 20 mm/s 60

3.14 Side-by-side comparison between (a) μSAXS mapping and (b - c) POM micrographs of a 3D printed NC/Amicure slice. The μSAXS image shows the extent of orientation imposed on the NC platelets by the printing process. The μSAXS data is reproduced from [114]. The arrows in (c) indicate the print sequence and the deformed region of printed roads. Samples were printed at 20 mm/s with a nozzle diameter of 609 μm. 63

4.1 (a) Direct ink writing (DIW) process using a 410-μm-diameter nozzle (b) Cartoon depicting the approximate velocity profiles that result from extrusion and translation during printing. (c – e) Photographs of triangular honeycombs printed with nozzle sizes of (c) 233 μm, (d) 609 μm and (e) 1041 μm. (f – h) Optical micrographs showing print features as a function of nozzle diameter. (i) Rectangular mechanical test specimens composed of fumed silica (FS), nanoclay (NC), SiC/FS and SiC/NC, printed with a 609-μm-diameter nozzle. Only longitudinal specimens are shown. 72

4.2 Scanning electron micrographs showing different morphologies of the as-received filler materials incorporated in this work. (a) fumed silica (FS) particles, (b) nanoclay (NC) platelets and (c) rod-like SiC-whiskers. 74

4.3 Rheological behavior of different epoxy-filled systems as it pertains to formulating printable inks for direct ink writing (DIW) process. (a) log-log plots of apparent viscosity as a function of shear rate and (b) the corresponding storage and loss moduli (i.e. viscoelastic properties) versus oscillatory shear stress for the inks shown in (a). The shear yield stress values are measured from the crossover point between the two moduli shown in (b). 81

4.4 Flexural properties of longitudinal and transverse specimens as a function of nozzle diameter for epoxy-based composites containing different filler materials. Flexural modulus (top) and flexural strength (bottom) are shown, respectively, for: (a and b) FS, (c and d) NC, (e and f) SiC/FS, and (g and h) SiC/NC composites. All composites were printed at a constant print speed of 20 mm/s. 83

4.5 Flexural properties of longitudinal and transverse specimens as a function of print speed for epoxy-based composites containing different filler materials. Flexural modulus (top) and flexural strength (bottom) are shown, respectively, for: (a and b) FS, (c and d) NC, (e and f) SiC/FS, and (g and h) SiC/NC composites. All samples were printed at a constant deposition nozzle diameter of 609 μm. 85

4.6 Representative optical transmitted light micrographs of polished thin slices ($<$ 1 mm thick) cut from printed specimens containing NC filler, observed using crossed polarizers. Specimens printed with nozzle diameters of (a) 233 μm, (b) 609 μm and (c) 1041 μm. These samples show strong periodic variations in birefringence that have length scales comparable to the diameter of the nozzle used for printing. The axis of the printed filaments is normal to the plane of the image. 89

4.7 Representative SEM micrographs of selected fracture surfaces for longitudinal flexural specimens with SiC/FS ink at varying print speeds: (a) 10, (b) 20 and (c) 40 mm/s. (d – f) Binary images of corresponding SEM micrographs analyzed with ImageJ to enable quantitative correlation between print speed and whisker alignment. White pixels indicate SiC-whiskers and black pixels indicate epoxy matrix. The print direction is normal to the plane of the image, thus SiC whiskers are observed to become more oriented (indicated by fewer in-plane whiskers) in the print direction as print speed increases (from left-to-right). 90

4.8 (a-c) SAXS 2D patterns for printed FS composites and (d-f) NC composites with nozzle diameters of 233 μm, 609 μm, and 1041 μm, in which the print direction is oriented along the horizontal axis. 92

4.9 (a-c) WAXS 2D patterns for printed FS composites and (d-f) NC composites with nozzle diameters of 233 μm, 609 μm, and 1041 μm, in which the print direction is oriented along the horizontal axis. Scattering at 0.51 $\mathring{A}^{-1}$ is denoted by an arrow in (d). 93

4.10 Plots of mechanical anisotropy versus normalized translation rat in (a) modulus and (b) strength for all the samples tested. Solid lines are the fit of the power-law model given in Eq. 4.5. 97

4.11 The difference in strength between the NC and FS composites (blue), and between the SiC/NC and SiC/FS (red) composites as a function of normalized translation rate. Dashed lines represent the linear regression of each data set. Plotted in this manner, the data suggest that NC is less influenced by normalized translation rate in the presence of SiC whiskers. 101

5.1 Schematic illustrations of (a) direct ink writing (DIW) process, and (b) effect of fiber length on ink processability and mechanical performance in fiber-reinforced composites. The shaded area demonstrates a typical range of fiber lengths in short carbon-fiber composites, which exhibits an excellent combination of material processability and mechanical behavior. (c) and (d) show carbon fibers before and after mixing. 108
5.2 Fiber length evolution during processing of CF inks: (a) FLDs for inks with different CF contents mixed for one mixing time (540s) and (b) FLDs for inks with constant CF content (9.15 vol%) mixed for different times 117
5.3 (a - b) CDFs of the corresponding FLDs shown in Fig. 1a and b, respectively, along with fitted Weibull distributions (solid lines). (c) Weibull fit parameters computation (Eq. 5.1) for inks with constant CF content of 9.15 vol% mixed for different times, along with dashed lines representing the linear regression of each dataset. (d) A summary of volume average fiber length values in all CF inks for different mixing times and CF contents. 118
5.4 Fiber length evolution during processing of CF/NC inks: (a) FLDs for CF/NC inks mixed for different times, (b) CDFs of the corresponding FLDs shown in (a), along with fitted Weibull distributions (solid lines). (c) Weibull fit parameters computation (Eq. 5.1) for the CF/NC inks mixed for different times, along with dashed lines representing the linear regression of each dataset. (d) A comparison between the volume averaged fiber lengths measured for inks containing 9.15 vol% CF and mixed for different times, in the presence and absence of NC. 120
5.5 Rheological behavior of epoxy-filled inks as a function of mixing time. (a) Log-log plots of apparent viscosity as a function of shear rate. (b) The corresponding storage and loss moduli as a function of oscillatory shear stress for the inks shown in (a). 122

5.6 (a) Representative optical micrographs of as-printed CF/NC longitudinal flexural test specimens. (b and c) Top-view optical micrographs of as-printed longitudinal specimens for mixing times of 180 s and 720 s, as well as (d and e) end views of the same bars, and (f-i) optical micrographs of printed complex geometries for the same mixing times of 180 s and 720 s. 126
5.7 Flexural strength and stiffness of 3D-printed CF/NC longitudinal specimens as a function of mixing time. 127
5.8 (a-d) Representative optical micrographs of the parallel-views of fracture surfaces for CF/NC longitudinal specimens showing variations in the pull-out lengths. (e-h) Representative optical micrographs of the end-views of the corresponding fracture surfaces shown in (a-d). 130
5.9 Representative SEM micrographs of selected fracture surfaces for CF/NC unidirectional flexural specimens printed with varying mixing times: (a) 180 s, (b) 360 s, (c) 540 s and (d) 720 s. 131
5.10 (a) χ_2 as a function of mixing time, and (b) model predictions (dashed lines) of the longitudinal composite strength as a function of mixing time and χ_1 value, plotted along with the experimental strength values. 136
5.11 Flexural properties of longitudinal and transverse CF/NC composites printed with constant mixing time (720 s) and varying ν/D ratios. (a) Flexural modulus and (b) flexural strength. (c) and (d) Corresponding master curves of mechanical anisotropy as a function of ν/D ratio. 137
5.12 (a) xCT reconstructions showing the scanned domain of the printed specimen and the coordinate system used. (b-c) X-ray computed tomography scan data for the printed composites with $\nu/D = 9.6$ s^{-1} and $\nu/D = 65.7$ s^{-1}, respectively, with fibers colored by their angle with the Z-axis (i.e., print direction).(d) Histogram of fiber orientation calculated from xCT reconstructions. 141

6.1 Property space map of strength versus modulus, which compare our printed epoxy-based composites in this work to other polymer composites fabricated by DIW. 150
A.1 Rheological behavior of epoxy/fumed silica (FS) inks: (left) log-log plots of apparent viscosity as a function of shear rate and (right) the corresponding storage and loss moduli versus oscillatory shear stress. 172
A.2 Optical micrographs of the as-printed ends of representative epoxy/FS longitudinal rectangular bars: (a) contains 5 wt.% FS, (b) contains 7.5 wt.% FS, and (c) contains 10 wt.% FS. 173
A.3 COMSOL analysis of the flow of the 10 wt% NC epoxy-based ink through a tapered printing nozzle with an outlet diameter of 609 μm: (a) pressure contours and (b) velocity magnitude within the deposition nozzle. 175
A.4 COMSOL analysis of the flow of the 10 wt% NC epoxy-based ink through a tapered printing nozzle with an outlet diameter of 609 μm. Distributions of (a) the velocity magnitude (m/s) and (b) the shear rate (1/s) at the outlet of the deposition nozzle. 2D profiles of (c) the velocity and (d) the shear rate as a function of radial distance in the deposition nozzle 176
A.5 2D schematic illustrations of the print paths employed in this work: (a) the longitudinal print path and (b) the transverse print path. It can be observed that the printed filaments or lines are oriented parallel and orthogonal relative to the length of the sample for the longitudinal and transverse print paths, respectively. 177
A.6 Rheological behavior of epoxy-based mixtures with single-filler material. (a) log-log plots of apparent viscosity as a function of shear rate and (b) the corresponding storage and loss moduli versus oscillatory shear stress for the inks shown in (a). The shear yield stress values are measured from the crossover point between the two moduli shown in (b). 179

A.7 Optical micrographs of representative fracture surfaces for longitudinal and transverse flexural specimens printed with the NC ink at varying nozzle sizes and print speeds. These micrographs demonstrate that all prints with different combinations of nozzle size and print speed yield fully-dense parts without any intrafilamentary voids, providing that the extrusion pressure was chosen appropriately. There is no evidence of the original print path or any delamination between layers, indicating complete coalescence and strong adhesion between printed filaments. 181
A.8 Representative optical transmitted light micrographs of polished thin slices (<1 mm thick) cut from printed specimens containing FS filler, observed using crossed polarizers. Specimens printed with nozzle diameters of (a) 233 μm, (b) 609 μm and (c) 1041 μm. These printed FS specimens do not exhibit any birefringence whatsoever, regardless of nozzle size. The approximate filament size is indicated by the red oval, which corresponds to the size of nozzle used for printing. The axis of the printed filaments is normal to the plane of the image. 182
A.9 Representative fit of scattering intensity between 0.5 $\mathring{A}^{-1} < q < 0.55\ \mathring{A}^{-1}$ as a function of azimuthal angle. Scattering data were fit using a Gaussian function centered about 0°. 183
A.10 SEM micrographs of the chopped carbon fibers used in this study. (a) Carbon fiber bundles and (b) single carbon fiber in the printed composite. 184
A.11 (a) Distributed carbon fibers after centrifugal planetary mixing and diluting in acetone. (b) Fiber length measurements in optical microscopy. 185
A.12 Density measurements of the 3D-printed and cured CF/NC composites (9.15 vol.% CF). 187
A.13 (a) Weibull shape parameter (k) as a function of mixing time, and (b) Weibull scale parameter, λ, as a function of mixing time. Dashed lines represent the linear regression of each dataset. 188
A.14 Master curves of mechanical anisotropy as a function of ν/D ratio in (a) modulus and (b) strength for epoxy-filled material systems. 190

Chapter 1

Motivation, Objectives and Thesis Outline

1.1 Motivation

Fused filament fabrication (FFF), an extrusion-based additive manufacturing (AM) method, is the most common type of 3D printing, which only uses thermoplastic polymer materials. FFF involves extruding a semi-molten thermoplastic material through a heated nozzle in a layer-by-layer fashion. Generally, 3D printed thermoplastics and thermoplastic composites via FFF suffer from poor layer-to-layer bonding, unavoidable porosity and inferior mechanical properties due to the thermal gradients that develop during printing [23, 31, 3, 11]. Despite the rapid advancements that are being made in thermoplastic AM, thermoset polymer materials have shown great promise as feedstock materials for the extrusion-based direct ink writing (DIW) AM technology (also known as Robocasting).

Thermoset materials offer high strength and stiffness, desirable thermal properties and increased compatibility with existing structural and functional filler materials. The potential use of thermoset polymers as ink feedstocks for DIW is attractive because chemical cross-links can form between printed layers and adjacent roads to improve the inter-layer and inter-road bonds compared to the printed thermoplastics [21, 22, 20]. The development of improved structural [14, 91, 22, 18, 94, 92, 83, 85] and functional [21, 20, 80] thermoset feedstock materials for DIW has been a major focus area by many researchers; however, a deep understanding of the fundamental processes during ink formulation and printing which govern microstructure and performance in 3D printed composites remains largely unexplored. This dissertation attempts to shed light onto the process–structure–property relationship in 3D printed thermoset composites produced via DIW. Establishing such a relationship is necessary to apply any engineering design principles to the design of AM components.

DIW involves extruding thermoset materials through fine deposition nozzles at room temperature, wherein the entire part is printed and subsequently thermally cured [22, 20, 21]. However, the success of DIW is dependent on the ability to design stable viscoealstic ink feedstocks with favorable rheological properties [22]. The ink material must exhibit strong shear-thinning and a yield stress behavior to enable efficient flow through fine nozzle diameters and shape retention after deposition, without curing on-the-fly [22]. Such rheological properties are usually imparted to thermoset resins through the incorporation of high-aspect-ratio

and high-surface-area filler materials [22, 14, 20]. In addition, as in any extrusion-based process, the shear and extensional flows that develop in the deposition nozzle during DIW induce preferential alignment on high-aspect-ratio filler materials in the ink [14, 91, 22, 83]. Therefore, filler orientation can be locally controlled within a printed part via tailoring the print path [2, 22].

For structural applications, several studies have focused on the development of printable fiber-reinforced epoxy-based inks for DIW, achieving printed fiber composites with exceptional strength and stiffness values along the print direction [22, 83, 92]. However, in these studies, fiber fillers alone, such as discontinuous carbon fibers and silicon carbide (SiC) whiskers, were found to be insufficient in epoxy resins to produce appreciable solid-like behavior and enable DIW printing. Therefore, a rheology modifier (i.e. viscosifier) was added along with fibers to induce thixotropy and enhance printability. The rheology modifiers that have been used most frequently for DIW are fumed silica (FS) [14, 91, 18, 72] and nanoclay (NC) platelets [22, 92, 83, 84]. To date, it has not been systematically studied what effects a rheology modifier has on the printability of a thermoset resin in the absence of fiber reinforcements. Furthermore, the effects of the deposition process on the orientation/arrangements of nanoscale fillers (i.e. NC, graphene flakes, carbon nanotubes, etc.), as well as the resulting effects on the thermomechanical properties and anisotropy in 3D printed composites have not been investigated in depth yet.

The orientation of high-aspect-ratio filler materials during DIW printing leads to a strong mechanical anisotropy in printed composites [22, 91, 92, 83]. This printing-induced anisotropy is a critical issue that impedes the straightforward design of composite parts for AM. Recent efforts have been taken to enable greater control over filler orientation and to achieve prescribed level of anisotropy in printed composites. These efforts have mainly focused on the utility of novel printhead designs and coupling DIW with external fields during printing, such as magnetic [69], acoustic [19, 18, 80] or shear [94] fields. In spite of these exceptional efforts, the specific fundamental relationships between filler morphology, print parameters (i.e. nozzle size and print speed), and resulting mechanical anisotropy in 3D printed composites have not been investigated yet. To 3D print a part via DIW, one must select a nozzle size and print speed. The effects of these necessary choices on filler

orientation and mechanical anisotropy in printed composites have not been systematically explored in this context yet. In addition, different filler morphologies have been utilized in the prior studies for developing DIW inks, such as platelet-like (i.e. NC, graphene), spheroidal-like (i.e. FS) and rod-like (i.e. SiC and CF). However, the extent to which these distinct morphologies, along with selected print parameters affect anisotropy in printed composites is not yet investigated. The current work will investigate these aspects utilizing the following filler materials: FS, NC, SiC and CF.

Furthermore, formulating structural DIW inks is typically done under high-shear mixing processes to enable sufficient dispersion of ink constituents and prevent potential issues with nozzle clogging. However, for certain filler materials, specifically CFs, their morphology is large and more fragile compared to other fillers, such as SiC whiskers, leading to potential fiber length attrition due to fiber interactions during mixing. It is important to highlight that the mechanical performance of fiber-reinforced composites is highly dependent on factors, such as fiber content, fiber length distribution (FLD) and fiber orientation distribution (FOD) [39, 41, 110]. Thus, to enable an understanding of the mechanical behavior of such printed composites, the linkage between fiber content, processing/printing parameters, the resulting FLD and FOD, and mechanical properties of 3D printed composites needs to be established.

1.2 Objectives

This dissertation seeks to elucidate process–structure–property relationships in 3D-printed epoxy composites produced via DIW. The specific objectives of this work are as follows:

- Investigating the effects of DIW deposition on filler arrangements and mechanical anisotropy in 3D-printed epoxy nanocomposites.

- Characterizing the effects of filler morphology, nozzle size and print speed on the extent of filler orientation, mechanical properties (i.e. strength and stiffness), and anisotropy in 3D-printed epoxy composites.

- Investigating the effects of ink formulation and processing parameters on fiber length distribution (FLD), printing behavior, fiber orientation distribution (FOD) and mechanical behavior in 3D-printed short carbon fiber-reinforced epoxy composites.

The fundamental questions underlying our research objectives include the following: (*i*) *How does a rheology modifier affect the printability of a thermoset resin in the absence of fiber reinforcements?* (*ii*) *Does the deposition process in DIW impart microstructural ordering on high-aspect-ratio nano-scale filler materials (i.e. nanoclays)?* (*iii*) *How does the deposition process in DIW influence the thermomechanical properties and anisotropy in 3D printed epoxy composites?* (*iv*) *How does the choice of print parameters (i.e. nozzle size and print speed) affect the strength and stiffness of 3D-printed composites comprised of isotropic and anisotropic filler materials?* (*v*) *How does the formulation process of fiber-filled DIW inks affect fiber length distribution (FLD), printability and mechanical properties of 3D printed fiber composites?* (*vi*) *How does the alteration of print parameters impact the resulting fiber orientation distribution (FOD) and mechanical anisotropy in 3D-printed short carbon fiber-reinforced epoxy composites?* By answering these questions we hope to provide a basis for future optimization of material systems and printing/processing parameters to enable more robust design of 3D-printed composite parts.

1.3 Thesis Outline

Chapter 2 provides a background information on additive manufacturing – specifically extrusion-based technologies and 3D-printed polymer composites – to give context to the current work.

Chapter 3 begins by investigating the rheological requirements for successful DIW using an epoxy/nanoclay (NC) material system in the absence of fiber reinforcements. It also investigates the effects of NC content on the printing behavior, the resulting thermomechancial properties, and anisotropy in printed nanocomposites as characterized by flexural testing, nanoindentation mapping, dynamic mechanical analysis (DMA), thermogravimetric analysis (TGA) and polarized light microscopy (POM). This chapter also expands into investigating the effects of the deposition process on the alignment and

arrangements of NC platelets within a printed composite using POM and scanning micro-beam small-angle X-ray scattering (μSAXS). This chapter concludes by establishing explicit correlations between optical birefringence patterns associated with the printing process, local/bulk mechanical properties, and filler arrangements within a 3D printed epoxy/NC composite.

Chapter 4 expands the work into investigating fundamental relationships between filler morphology, print parameters (i.e. nozzle size and print speed) and the extent of mechanical anisotropy in 3D printed epoxy-based composites. Printable epoxy-based inks are formulated for DIW using filler materials with different morphologies. Test specimens are printed using different nozzle sizes and print speeds. The mechanical properties and anisotropy of printed composites are characterized by testing specimens parallel and transverse to the print direction using 3pt-flexural testing. The composites microstructure, print patterns and degree of filler orientation are evaluated through POM, small– and wide–angle x-ray scattering (SAXS & WAXS) and scanning electron microscopy (SEM).

Chapter 5 aims at investigating the effects of ink formulation and processing parameters on the evolution fiber length distribution (FLD) during processing of epoxy/chopped-CF inks for DIW. The processing parameters that are taken into account are: (*i*) CF volume content, (*ii*) the presence or absence of a rheology modifier (i.e. NC platelets), and (*iii*) shear mixing time. FLD is measured for a wide range inks, and the distributions are fit with a Weibull-type distribution function. Tradeoffs between FLD, ink processability, ink rheology, printing behavior and mechanical properties are highlighted. Additionally, the effects of printing parameters (nozzle size and print speed) on mechanical anisotropy and fiber orientation distribution (FOD) in printed composites are explored. Mechanical properties of printed composites are characterized via 3pt-flexural testing, and microstructure is investigated using optical and scanning electron microscopy (SEM), and x-ray computed tomography. Finally, the fitted Weibull parameters are fed into a composite model that incorporates FLD and FOD, and model predictions are found to be in excellent agreement with experimental observations.

Finally, Chapter 6 sums up the important findings of this work.

Chapter 2

Introduction

2.1 Additive Manufacturing

Additive manufacturing (AM), commonly referred to as three-dimensional printing (3DP), rapid prototyping (RP) or freeform fabrication, is an emerging technology that enables the fabrication of components with unprecedented geometric complexity and material architectures. A key requirement for any AM process is the design of a virtual three-dimensional Computer-Aided Design (3D CAD) model. An example is shown in Figure 2.1 for AM of a teacup. The 3D CAD model is needed to fully describe the desired part geometry and where the material is to be located within a design space [107]. Using a slicing software, the CAD model is sliced into finite number of cross-sections (i.e. 2D contours) that also define the tool path (or print path), as shown in Figure 2.1. The generated data is then converted to a standard AM file, known as Standard Tessellation Language (STL), that AM processes use for printing. As opposed to subtractive processes, in which the material is removed bit-by-bit from a bulk to form the desired geometry, the part in AM is built in an incremental, layer-by-layer fashion. Each printed layer in the physical part represents a thin cross-section of the geometry derived from the original CAD model. However, as the build progresses, the printed layers must be adhered to one another to achieve void-free and robust structures.

AM was first developed by Chuck Hull in the mid-1980's when he invented the technology of Stereolithography for 3D-printing of photopolymers. AM technologies have evolved since then and now can process a wide range of materials, including metals [101, 37, 57], ceramics [112, 66], polymers [30, 29, 116, 118] and biomaterials [12, 55, 131].

2.2 Polymer AM technologies

Polymer AM technologies include [107]: (*i*) stereolithography (SLA), (*ii*) photopolymer jetting (Polyjet), (*iii*) selective laser sintering (SLS), (*iv*) fused filament fabrication (FFF), and (*v*) direct ink writing (DIW). In both SLA and Polyjet processes, liquid photopolymer precursors are exposed to an ultraviolet (UV) laser to enable cross-linking during or directly after deposition [78]. SLS process uses powdered thermoplastic polymer feed-stocks that are

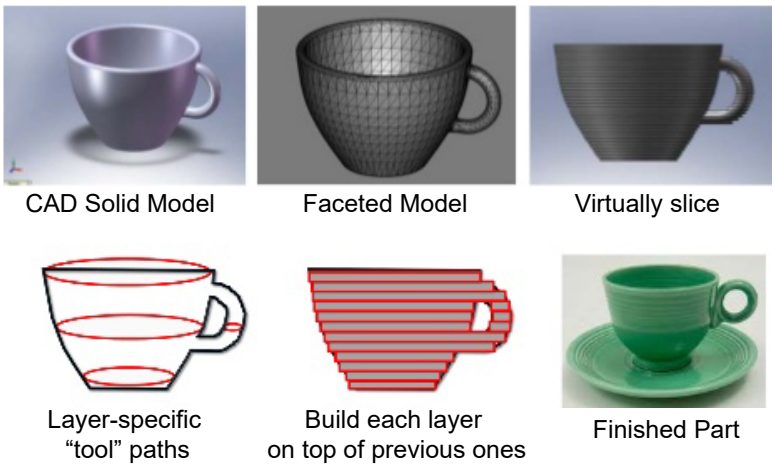

Figure 2.1: CAD model of a teacup with further images showing how additive manufacturing works [123]

selectively sintered or fused in a powder bed using a laser beam [45]. In FFF processes — including fused deposition modeling (FDM) and big area additive manufacturing (BAAM) — thermoplastic feedstocks, either in the form of pellets or filaments, are semi-molten in a heated nozzle and then directly deposited via extrusion onto a substrate [4, 67, 29, 31, 23, 56]. Finally, DIW utilizes viscoelastic thermoset feed-stocks, such as epoxies and silicones, that can be deposited through small nozzle diameters via extrusion at room temperature [73, 22, 21, 20]. In the next sections, we will only focus on the extrusion-based polymer AM technologies, which include both FFF and DIW.

2.3 Extrusion-based polymer AM

2.3.1 Fused filament fabrication (FFF) and its composites

FFF processes are the most common types of extrusion-based 3D printing, but limited to the use of thermoplastic polymers, like Acrylonitrile Butadiene Styrene (ABS), Poly(lactic acid) (PLA), and Nylon. FFF processes typically involve melting and extruding the thermoplastic material through a heated deposition nozzle, and the deposited layers cool and solidify upon printing, as shown in Figure 2.2. As a consequence, high thermal gradients and residual stresses can develop in printed parts, leading to void formation, poor layer-to-layer bonding, warping and inferior mechanical properties [110, 31, 67, 3, 23]. To improve the mechanical performance and thermal properties of printed thermoplastics, researchers in the field have added filler materials into thermplastic resins.

For example, Love et al. showed that the incorporation of carbon fibers (CFs) (up to 13 vol%) into a thermoplastic ABS resin can drastically diminish warping in printed parts by reducing the coefficient of thermal expansion (CTE) of the neat ABS resin by 88.72% along the deposition direction [76]. The work also showed that printed ABS/CF composites exhibited higher tensile strength (∼194% increase), stiffness (∼335% increase), and thermal conductivity (∼124.3% increase) than neat ABS when tested parallel to the deposition direction [76].

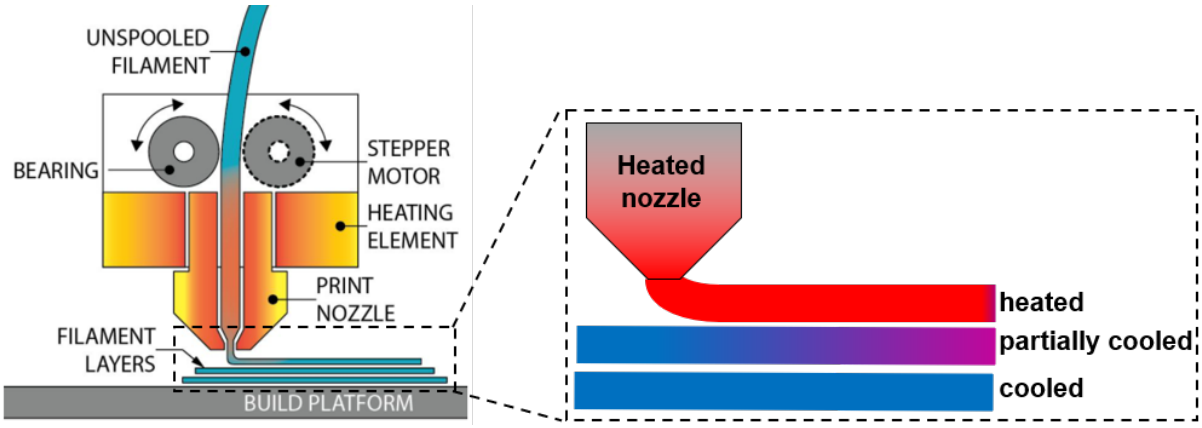

Figure 2.2: Schematic illustration of the fused filament fabrication (FFF) technology [65]

Zhong et al. incorporated glass fibers (up to 18 wt%) into an ABS resin, leading to an increase of 140% in the tensile strength along the print direction; however, the presence of glass fibers was found to reduce the flexibility of the ABS filaments [133]. Tekinalp et al. showed that short CFs align in the print direction during printing ABS/CF composites (up to 40 wt% CF), improving the strength by 115% and the stiffness by ∼700% along the print direction over neat ABS [110]. Although highly oriented CFs were achieved in printed ABS/CF composites, increased porosity caused lower tensile properties than those of their compression-molded counterparts [110]. It was also found that the average fiber length in printed ABS/CF composites decreased with increasing CF content, as a result of fiber breakage during compounding the CF and ABS resin under high-shear mixing [110]. Yeole et al. compared CF-reinforced polyphenylene sulfide (PPS) composites with 50 wt% CF produced via single-screw FFF printing, injection, and compression traditional molding processes [130]. In their work, it was shown that FFF composites display comparable tensile properties to compression-molded composites, while injection-molded composites exhibit a 119% and 55% increase in the strength and stiffness, respectively, over FFF composites [130]. Fiber attrition was observed in the three different composites, with FFF composites exhibiting the highest volume porosity, which was the reason behind reducing their mechanical properties [130].

Ning et al. investigated the effect of fiber length on the mechanical properties of ABS/CF composites printed via FFF at a CF loading of 5 wt% [86]. Their results showed that printed composites with fiber lengths of 150 μm achieved higher tensile strength and modulus than printed composites with fiber lengths of 100 μm [86].

Other structural filler materials were also employed, for example, Shofner et al. added 10 wt% of single-walled carbon nanotubes (CNTs) to an ABS resin and showed that CNTs adopt preferred alignment during printing, improving the tensile strength and modulus along the print direction by 39% and 61%, respectively, over the ABS resin [104]. Weng et al. showed that the addition of only 5 wt% of organic modified montmorillonite (OMMT) to an ABS resin improved the tensile strength by 43%, the elastic modulus by 200% and the glass-transition temperature by 13% over neat ABS [122].

Although the above studies demonstrate that the addition of filler materials to thermoplastic resins can drastically improve the mechanical properties along the print direction, poor interlaying bonding and prominent porosity remains a challenge in printed thermoplastic polymers. As opposed to thermoplastic feed-stocks, thermoset polymer materials – those that undergo an irreversible chemical crosslinking when heated – offer excellent combined mechanical, chemical and thermal properties, as well as increased compatibility with existing structural and functional filler materials. Thermoset polymers have shown significant promise as feed-stocks for DIW AM technology.

2.3.2 Direct ink writing (DIW)

DIW is a novel, low-cost extrusion-based AM technology that is commonly used for 3D printing of polymers. This method uses ink feedstocks with tailored rheological properties that can be extruded through sub-millimeter deposition nozzles ($\geq$ 50 μm) and patterned in a filamentary form, as schematically shown in Figure 2.3. This approach enables self-stable 3D objects with micro-to-macro length scales to be printed, and the resolution of the printed part can be controlled by the size of the extrusion nozzle. DIW deposits the feedstock material using appropriate syringe-like cartridges that are controlled via either pneumatic pressure or displacement-based mechanical plungers. During deposition, a 3-axis motion stage is used to move the nozzle (*i.e* print head) at a given translation rate in the X-Y-Z plane (Figure 2.3) based on the geometry of the part. DIW was initially introduced under the name of "Robocasting" for the deposition of ceramic slurries by Cesarano, J and Calvert, P in the 1990's [link], and then was expanded for the deposition of reinforced thermosetting polymers [91, 14, 13]. Recently, DIW has been employed for the deposition of metal-based inks [127, 126], polydimethylsiloxane (PDMS) [58], recyclable inks [103], functional inks [21, 20, 73], ceramic-based inks [74, 66] and others. The feed-stock in DIW, depending on the base resin, can be deposited at room temperature and then cured through either gelation, liquid evaporation or heat, or it can be exposed to some heat or ultraviolet light during deposition to induce cure [73].

This work will mainly focus on thermoset ink materials, specifically epoxy-based inks, for room temperature DIW. To formulate a thermoset ink for DIW, three key constituents

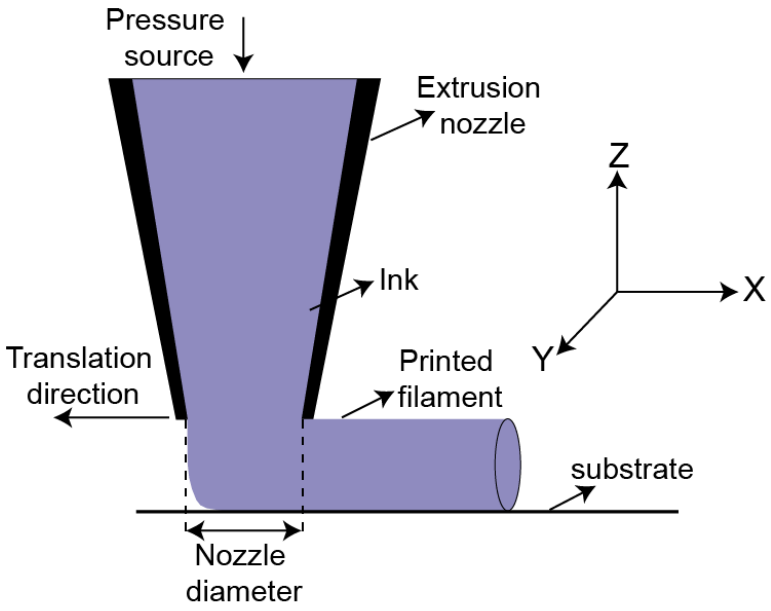

Figure 2.3: Schematic illustration of direct ink writing (DIW) technology

are needed: (*i*) thermoset base resin, (*ii*) crosslinker or catalyst, and (*iii*) additives (structural and/or functional filler materials). These constituents are usually mixed together in a high-shear planetary mixer to enable sufficient dispersion of fillers into the base resin and prevent potential nozzle clogging during printing [22]. The resulting ink material (*i.e.* mixture) must possess certain favorable rheological properties to enable deposition at room temperature [73, 22, 20]. Section 2.4 provides a detailed discussion about the rheological properties and filler materials required for DIW printing.

2.4 DIW requirements

2.4.1 Ink rheology

The nature of room temperature DIW printing places unique requirements on the rheology of the ink material to be printed. The ink material developed for DIW must exhibit strong shear-thinning behavior to enable efficient flow through fine deposition nozzles. In addition, the ink material must exhibit a solid-like behavior with a sufficiently high storage (i.e. elastic) modulus (G') and shear yield stress (τ_y), so that the part can maintain its shape upon printing, without immediate curing after deposition [20, 22, 73, 74, 98, 105].

Figure 2.4 shows representative plots of the rheological properties typically observed with DIW inks. Figure 2.4a displays the viscosity (η) as a function of shear rate ($\dot{\gamma}$). The shear-thinning behavior can be observed in Figure 2.4a, which is characterized by a decrease in the viscosity of the ink by several orders of magnitude as the applied shear rate increases. Typical shear rates experienced during DIW range from $\dot{\gamma} = 0.01$ to $\dot{\gamma} = 50\ s^{-1}$. Figure 2.4b shows representative plots of the storage (G') and loss (G'') moduli as a function of shear stress (τ). G' represents the elastic behavior of the ink material, and G'' represents the viscous behavior of the ink material. For a shear-thinning ink, at low shear stresses, G' is higher than G'', indicating that the ink behaves predominantly as a solid-like fluid. However, as the applied shear stress exceeds a certain value, G' decreases monotonically to a value below that of G'', indicating that the ink begin to behave more as a viscous-like fluid. This transition from solid-like to viscous-like behavior corresponds to the shear yield stress (τ_y),

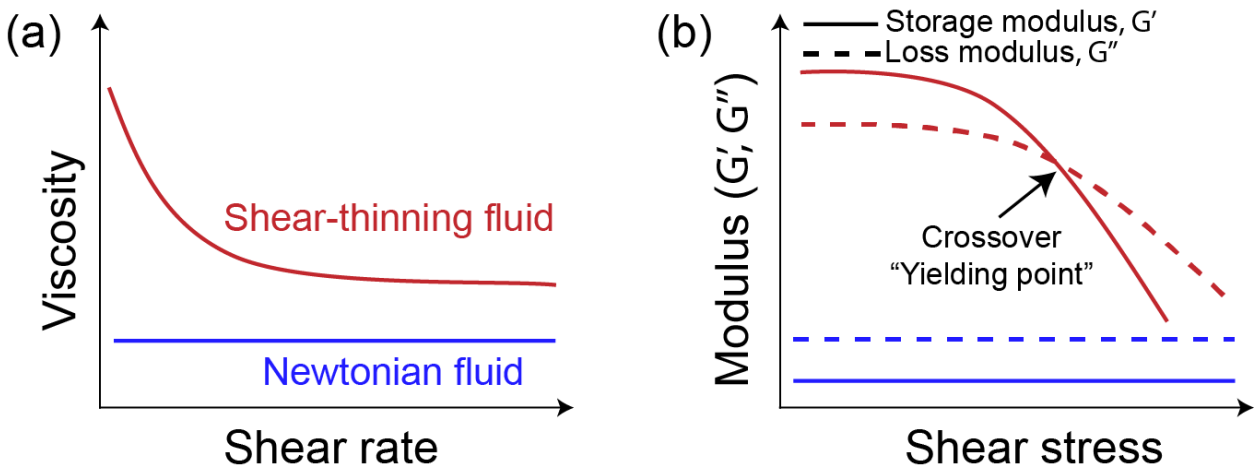

Figure 2.4: DIW rheological requirements: (a) viscosity as a function of shear rate and (b) log-log plots of storage and loss moduli as a function of shear stress for Newtonian and shear-thinning ink fluids

which can be measured from the crossover point between the two moduli ($G' = G''$). Inks with high shear yield stress values are usually preferable, since they are capable of holding their shape upon deposition and resisting deformation under gravitational force, thereby minimizing material spreading and flowing. However, higher extrusion pressures or mechanical forces are required to enable flow of such inks through a nozzle.

For viscous fluids, such as most epoxy resins, the viscosity is constant over a certain range of shear rate (Figure 2.4a), characteristic of a Newtonian behavior. As a result, G'' is higher than G' across the range of shear stress, and both moduli are stress-independent (Figure 2.4b). Although this fluid can be easily extruded through a small nozzle diameter, it does not have the capability to remain stable after deposition.

These rheological properties are frequently measured using a rotational rheometer with parallel plate measuring system. The ink material is loaded between two parallel plates with prescribed gap size, one of which rotates at a known rate. The shear-thinning behaviour is usually characterized using continuous flow sweeps at controlled shear rates, while storage and loss moduli are measured using oscillatory stress sweeps in stress controlled mode [22, 20, 83, 105].

2.4.2 Filler materials

These rheological properties (i.e., strong shear-thinning and yield stress behavior) required for DIW are usually imparted to epoxy resins by high-aspect-ratio and high-surface-area filler materials. Such fillers increase the viscosity and stiffness of the base resin at rest through interfacial interactions between the filler and base resin, leading to increased print stability after deposition [98, 21, 20, 22, 105]. The rheology modifiers (i.e. viscosifiers) that have been utilized most frequently are functionalized nanoclay (NC) platelets [22, 94, 83, 85, 84, 92, 21, 20] and fumed silica (FS) particles [91, 14, 18, 69]. Many other filler materials have been added along with these viscosifiers in epoxy resins to enable DIW of both structural and functional composites. Of these, discontinuous carbon fibers (CFs) [22, 92, 83, 94, 88], Silicon carbide (SiC) whiskers [22], short Kevlar fibers [84], glass microballoons (GMBs) [85, 88], graphene platelets [20], NdFeB magnetic particles [21], etc.

The filler materials utilized can serve to impart both beneficial rheological properties for DIW, and desirable mechanical reinforcement in the printed, cured composite. This is possible through properly tailoring ink constituents and filler loadings. Moreover, these filler materials have different morphologies, which may lead to meaningful differences in rheological behavior and resulting mechanical anisotropy in printed composites.

To disperse fillers into the base resin (i.e. matrix), high-shear mixing processes are typically employed. For certain filler morphologies, such as fibers, fiber breakage can occur during formulating due to fiber-fiber and fiber-matrix interactions, resulting in a fiber length distribution (FLD) in the ink formulation [110, 39]. FLD along with fiber content are important parameters that significantly influence the mechanical behavior of fiber-reinforced polymer composites [39, 41, 92, 83]. While high fiber contents are desirable for higher strength and stiffness values, more mixing time is required to achieve sufficient dispersion, which lead to a decrease in the mean fiber length [110]. This leads to a tradeoff between fiber length and fiber loading. However, to enable efficient load transfer to the fibers by the matrix and allow sufficient translation of fiber property, fibers need to be longer than a critical value [41]. The critical fiber length (L_c) can be defined as the minimum fiber length at which an effective load transfer is transmitted to the fibers by the matrix. L_c is dependent on fiber diameter, the ultimate strength of the fiber and the interfacial shear strength between the fiber and matrix [39]. It is hypothesized that the FLD can be controlled via rational selection of mixing time, fiber content and other ink constituents (i.e. rheology modifiers).

2.5 3D-printed thermoset composites and mechanical properties

With thermoset DIW inks, since the part can be printed entirely at room temperature and subsequently thermally cured in a secondary step, the dependency of mechanical properties on thermal history can be significantly reduced. This approach allows thorough chemical crosslinking between layers which is hypothesized to lead to more cohesive interlayer bonding than FFF [22, 21, 77, 92, 83]. Additionally, enabled by deposition at room temperature, DIW

offers significant reduction in energy consumption compared to FFF processes, where the thermoplastic material is subjected to repeated heating and cooling cycles throughout the printing process.

Epoxies have been used most frequently as the DIW ink base. For example, the first demonstration of material extrusion AM of epoxy composites was performed by Calvert et al. in 1997 [14]. In that study, the team formulated epoxy-based inks for DIW utilizing varying fractions of CF with varying fiber lengths and in the presence of FS to impose shear-thinning behavior. The modulus and strength of printed composites showed dependence on both fiber length and CF content, and fiber orientation was shown to follow the direction of printing. In a subsequent study, Peng et al. formulated glass-fiber-reinforced epoxy inks for DIW in the presence of FS nanofiller [91]. In that study, flexure test specimens were printed with varying print-head speeds and raster angles (i.e. print paths) relative to the length of the specimen [91]. Their results showed that the degree of fiber orientation increases with increasing print-head speed while keeping the flow rate constant. As a result of increased fiber alignment, the flexural modulus improved by 50% as the print-head speed increased by a factor of 2.5 [91]. In addition, anisotropy was observed in measured flexural modulus as a result of preferred fiber orientation relative to the print path (or raster angle) [91].

Furthermore, Compton and Lewis formulated epoxy inks filled with SiC, CF and NC filler materials, achieving Young's modulus up to 24.5 GPa along the print direction [22]. Additionally, strong mechanical anisotropy was observed in tensile specimens printed longitudinal and transverse to the print direction [22]. They attributed this observation to the highly aligned and oriented fibers in the direction of printing [22].

Malek et al. used ultrahigh-modulus pitch-based CFs in an epoxy resin filled with NC and achieved elastic modulus up to 57 GPa in the direction of printing [77]. More recently, Nawafleh and Celik utilized a vibration-assisted print head to enable printing epoxy/NC/CF inks with a high loading of CF (up to 46 vol%), achieving flexural strength values up to 400 MPa and stiffness up to 53 GPa in the print direction [83]. The strength versus modulus values for current 3D printed fiber-reinforced epoxy composites are plotted in Figure 2.5 and summarized in Table 2.1.

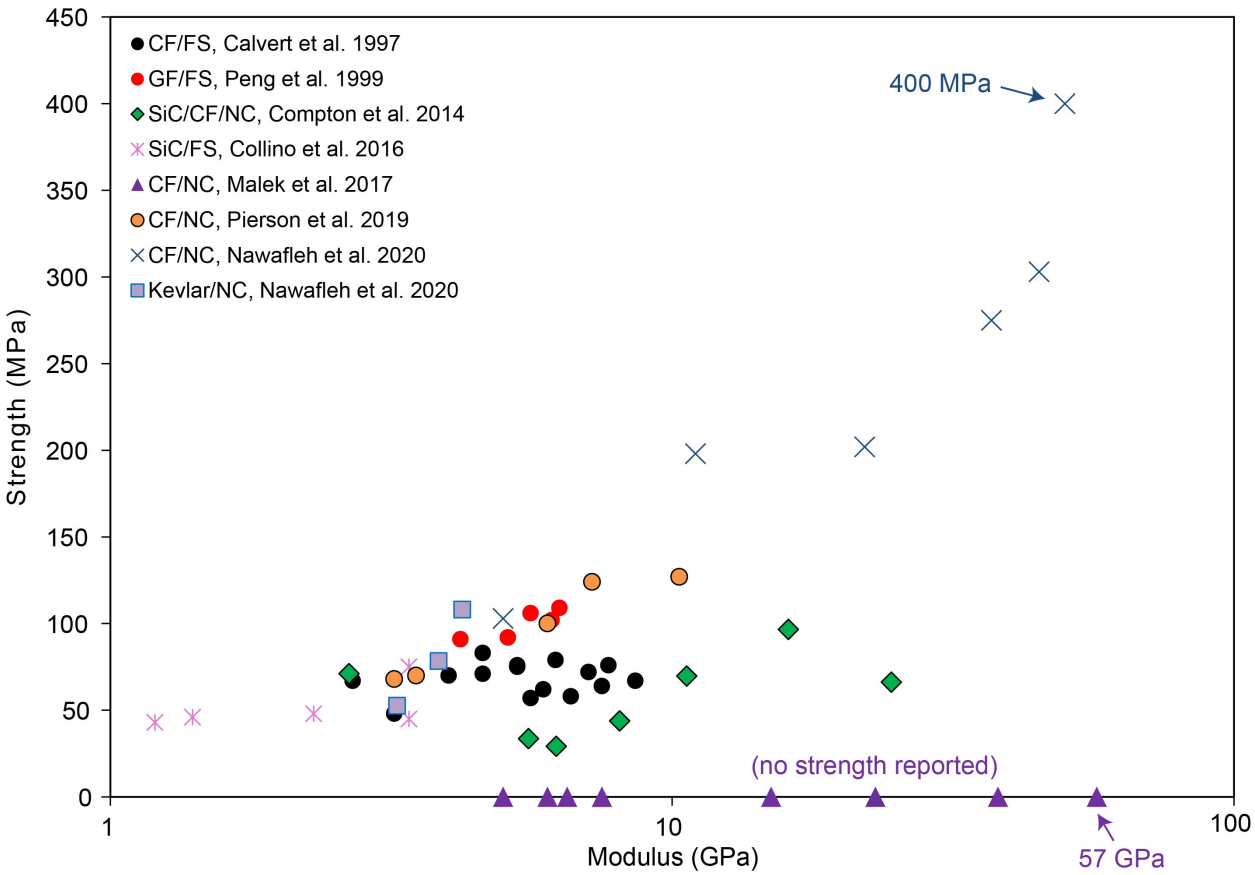

Figure 2.5: Property space map of strength versus modulus for 3D-printed fiber-reinforced epoxy composites fabricated via DIW [14, 91, 22, 18, 77, 92, 83, 84].

Table 2.1: Composition and mechanical properties of epoxy-based fiber-reinforced composites produced via DIW

Epoxy Resin /curing agent	Viscosifier/ content (wt%)	Fiber type	Fiber content (vol%)	Fiber length (μm)	Composite modulus (GPa)	Composite strength (MPa)	Source
MY720/ DDS	FS/8	CF	0	-	2.7	67	[14]
			10.2	200	5.3	75	
			13.8	200	6.2	79	
			21.6	200	7.7	76	
			10.2	85	4	70	
			10.2	110	4.6	83	
			10.2	170	4.6	71	
		10.2	220	5.3	76		
			13.8	85	5.9	62	
			13.8	110	5.6	57	
			13.8	170	6.6	58	
			13.8	220	7.5	64	
Epon828/ Jeffamine	FS/8	CF	0	-	3.2	48	[14]
			13.8	220	7.1	72	
		21.6	220	8.6	67		
Epon828/ Jeffamine	FS/8	GF	18		4.2	91	[91]
			18		5.1	92	
			18	30-70	5.6	106	
		18		6.1	102		
			18		6.3	109	

Table 2.1. (Continued)

Epoxy Resin /curing agent	Viscosifier/ content (wt%)	Fiber type	Fiber content (vol%)	Fiber length (μm)	Composite modulus (GPa)	Composite strength (MPa)	Source
Epon826/ VS03	NC	SiC	0	12	5.55	33.6	[22]
			0		6.22	29.2	
			17.3		10.6	69.8	
			17.3		16.1	96.6	
			20.3		8.06	43.9	
			20.3		24.5	66.2	
Epon826/ VS03	FS/6	SiC	0	20-63	1.2	43	[18]
			0.8		1.4	46	
			0.8		2.3	48	
			1.9		3.4	45	
			0.8		3.4	75	
Epon826/ VS03	NC/5	CF	0	-	3.2	68	[92]
			0.6	1171	3.5	70	
			2.3	413	6	100	
			3.9	370	7.2	124	
			5.5	315	10.3	127	
Epon826/ VS03	NC	CF	5	50	5	103	[83]
			12		11	198	
			21		22	202	
			28		37	275	
			36		45	303	
			46		50	400	

2.6 Filler alignment and anisotropy

The prior studies demonstrated that high-aspect-ratio filler materials align in the print direction during extrusion-based 3D-printing [14, 91, 22, 92, 110]. Filler alignment (see Figure 2.6) occurs as a result of the high shear and extensional flow fields that the ink material experiences as being extruded through the deposition nozzle [22]. This shear-induced alignment leads to strong anisotropy in 3D printed composites that significantly complicates the straightforward design of additively manufactured composite parts.

The alignment of high-aspect-ratio filler materials during extrusion has been studied for decades. Jeffrey showed that plate- and rod-like fillers adopt a stable alignment (with their longer axis oriented along the flow direction) in purely extensional flows, however, in a simple shear flow, elliptical fillers continue to rotate (Jeffrey orbitals), resulting in a non-static filler alignment [62]. More recently, other authors extended Jeffery's analysis to concentrated short-fiber suspensions and to enable the prediction of the distribution of fiber orientation, as well as the thermal and mechanical properties of the fiber composites [36, 1].

Typically, the degree of filler alignment is dependent on several factors such as, filler aspect-ratio, ink viscosity, filler volume fraction and processing parameters (i.e. nozzle geometry, translation rate and extrusion rate). For example, Goettler found that fiber orientation is highly dictated by the the total amount of extensional strain that is subjected to the flowing material [48]. The total extensional strain is determined by the area reduction ratio, which is defined as the ratio of the diameter of the fluid reservoir to the diameter of extrusion die [48]. Farkash et al. reported a strong correlation between fiber orientation and the aspect ratio of the extrusion channel (or die), and a weak correlation between fiber alignment and flow rate [34]. Additionally, an increase in filler alignment was observed with increasing filler aspect-ratio, as well as with increasing the viscosity of the carrier fluid [82, 41, 34]. Many researchers observed a decrease in the degree of filler alignment with increasing filler loading [10, 71, 82].

In the context of extrusion-based AM, Compton and Lewis showed that short carbon fibers highly align in the printed direction for printed epoxy-based composites [22], Tekinalp et al. reported a high degree of fiber orientation along the print direction for printed ABS

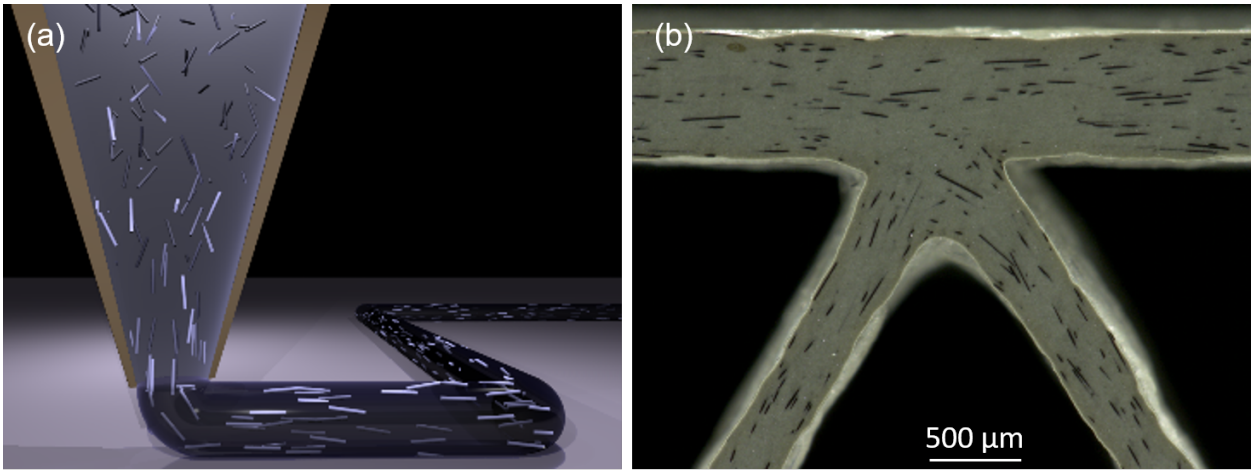

Figure 2.6: (a) Schematic illustration of the alignment of high-aspect-ratio fillers within the nozzle during DIW deposition, and (b) epoxy/SiC/Carbon-fiber printed walls, revealing highly oriented carbon fibers oriented in the print direction. Adapted from [22].

thermoplastic composites [110], and Peng et al. showed an increased alignment of glass-fibers along the direction of deposition with increasing the translation speed of the print-head while keeping the extrusion rate constant [91]. In a very recent study, Haney et al. reported an increase in the alignment of graphene (GNP) platelets with increasing the translation speed of the print-head, and hence increasing the electrical conductivity of printed epoxy/GNP composites [54]. It is noted that the alteration of printing parameters in DIW (i.e. nozzle size, print speed and extrusion pressure) leads to a change of the shear forces acting on the extruded ink material during deposition, which, in turn, affect the final degree of filler alignment in the printed composites [22, 91, 54].

To enable greater control over filler orientation and resulting anisotropy in 3D printed composites, multiple routes have been implemented. For example, Raney and Compton et al. have implemented a novel, rotational print-head during DIW extrusion, imparting a helical arrangement of carbon fibers in printed epoxy composites [94]. In this manner, the resulting helical angle of fibers relative to the axis of printed filament can be spatially controlled through proper regulation of the ratio of rotation rate to translation rate. Collino et al. have shown that the alignment of microfibers can be spatially controlled within printed epoxy filaments using an acoustic focusing nozzle during a DIW process [18]. In addition, Melchert et al. employed acoustic fields to control the arrangements of conductive short CFs in a flexible photopolymer, enabling tuned electrical conductivity in printed composites [80]. Kokkinis et al. utilized external magnetic fields to spatially control the composition and the alignment of magnetically functionalized alumina platelets in printed polymer composites [69].

Chapter 3

Effects of DIW deposition on filler arrangements and mechanical anisotropy in 3D-printed epoxy nanocomposites

This chapter is revised based on a paper published by Hmeidat et al.: **Hmeidat, N. S.**, Kemp, J. W., & Compton, B. G. (2018). High-strength epoxy nanocomposites for 3D printing. *Composites Science and Technology*, 160:9–20. Link [59].

The Scanning micro-beam small-angle X-ray scattering figure (Figure 3.14a) is adapted from a published paper by Trigg et al.: Trigg, E. B., **Hmeidat, N. S.**, Smieska, L. M., Woll, A. R., Compton, B. G., & Koerner, H. (2021). Revealing filler morphology in 3D-printed thermoset nanocomposites by scanning microbeam X-ray scattering. *Additive Manufacturing*, 37, 101729. Link [114].

3.1 Abstract

Clay-based nanoscale filler materials are commonly used as viscosifiers (i.e. rheology modifiers) in fiber-filled polymer inks developed for direct ink writing (DIW). The high-surface-area of nanocaly (NC) results in high interfacial area shared with the polymer resin, imparting desirable rheological properties (i.e. shear-thinning and shear yield stress) required for deposition. However, little is known about the effects of the deposition process on the orientation of nanoscale fillers (i.e. NC), and the resulting effects on thermomechanical properties of printed composites. In this work, we characterize the effects of the content of a functionalized NC on the rheological properties and printing behavior of an epoxy resin in the absence of fiber reinforcements. Furthermore, we investigate the effects of the deposition process on the orientation of NC platelets, as well as the resulting thermo-mechanical properties and anisotropy in 3D-printed epoxy/NC composites. The rheological properties of ink formulations containing up to 12.5 wt.% NC are measured using parallel plate rheometry, and the thermo-mechanical properties of the printed composites are measured using 3-pt flexural testing, nanoindentation mapping, dynamic mechanical analysis, and thermo-gravimetric analysis. Print patterns and filler orientation are studied using polarized light microscopy (POM) and micro-beam small-angle X-ray scattering (μSAXS). Good printing behavior was observed in NC inks with shear yield stress and plateau elastic modulus values greater than $\sim$300 Pa and $\sim$60 kPa, respectively. The deposition process is shown to impart preferential orientation to the NC platelets associated with (1) the shear fields during

extrusion and (2) the road-to-road shear upon deposition onto the substrate, resulting in mechanical anisotropy in printed composites. Flexural strength values range from 80 MPa to 100 MPa for cast samples and printed samples tested transverse to the printing direction, and up to 143 MPa for printed samples tested parallel to the print direction. Despite the observed anisotropic strength values, the strength in each direction is significantly greater than values reported for 3D printed thermoplastic composites, suggesting that the epoxy/NC system has high potential for further development as a 3D printing feedstock material. Finally, correlations between visible optical birefringence patterns associated with the printing process, local mechanical properties, and NC arrangements within a printed component are presented.

3.2 Introduction

Nano-scale layered silicates, such as nanoclay (NC), show great promise as filler materials to improve the strength, stiffness, toughness, gas barrier, and flame retardant properties of polymer resins [9, 43, 70, 134, 52]. The exceptional property enhancements are mainly attributed to the high surface-to-volume ratio and platelet morphology of NC, which results in high interfacial area and interaction volume between the filler and matrix, and enables the platelets to be oriented through certain processing routes like solvent casting [28], and high shear extrusion [42]. The NC/epoxy system, in particular, has received considerable attention because of the desirable mechanical, thermal, and chemical properties of cross-linked epoxy resins, and the favorable interaction chemistry between the epoxy prepolymer and the NC materials [9, 70, 134, 16, 81, 90, 100]. However, the high surface area of the NC platelets leads to large increases in viscosity when added to epoxy resins [81], which can present challenges during processing using traditional methods such as casting or infiltration.

Recently, Compton and Lewis demonstrated that NC platelets can be used in epoxy/short fiber composite inks for direct ink writing (DIW) additive manufacturing (AM) to impart nearly ideal rheological properties (a high degree of shear thinning, and yield stress behavior) for extrusion-based 3D printing [22]. Since this work, there has been significant effort in 3D printing of polymer matrix composites in general [118, 33, 61, 89], and rapid progress in 3D

printing of epoxy-based composite materials containing silica, NCs, fibers, and functional materials [18, 20, 21, 38, 72, 77], specifically. These works have demonstrated significant improvements in elastic modulus (up to 57 GPa in tension) [77] and control of filler orientation and architecture [18, 94] compared to earlier work [22, 14, 91], but basic 3D-printable epoxy/NC systems have not been thoroughly characterized and investigated in the context of AM. In this work we investigate effects of NC content on the rheology, printing behavior, and thermomechanical properties of an epoxy-based DIW feedstock in the absence of fibers or functional filler materials. We also investigate the effects of the deposition process on the orientation of NC platelets and anisotropy in the resulting printed epoxy/NC nanocomposites.

AM is the process of building components in an incremental, additive fashion through either direct material deposition or selective material consolidation within a vat or powder bed. Traditional polymer AM technologies use either thermoplastic feedstocks that are liquefied in a heated deposition nozzle prior to deposition, as is the case with fused deposition modeling (FDM), fused filament fabrication (FFF), and big area additive manufacturing (BAAM), or are selectively sintered in a powder bed using a laser (selective laser sintering - SLS), or they utilize liquid polymer precursors that cross-link when exposed to ultraviolet light during or directly after deposition, as is the case for stereolithography (SLA) and polymer jetting. DW 3D printing is somewhat different in that viscoelastic feedstocks are deposited via extrusion through fine nozzles at room temperature without requiring melting prior to, or curing immediately after, deposition. In this process, shown schematically in Figure 3.1a, the feedstocks must possess sufficient yield stress and shear thinning behavior that they can be readily extruded through fine nozzles, but quickly recover high viscosity and elastic behavior in order to maintain shape after deposition [73, 111]. Because the process proceeds at ambient temperature, it has the potential to alleviate the geometric warping and residual stresses that arise in 3D printed thermoplastic materials due to the strong thermal gradients that result from the heating and cooling associated with deposition [23, 26, 76, 117]. It is important to note that thermosets do experience shrinkage during curing [35] that can lead to warping in geometrically complex parts. However, shrinkage can be limited through the choice of curing agent and filler material, and preliminary experiments on large-scale –

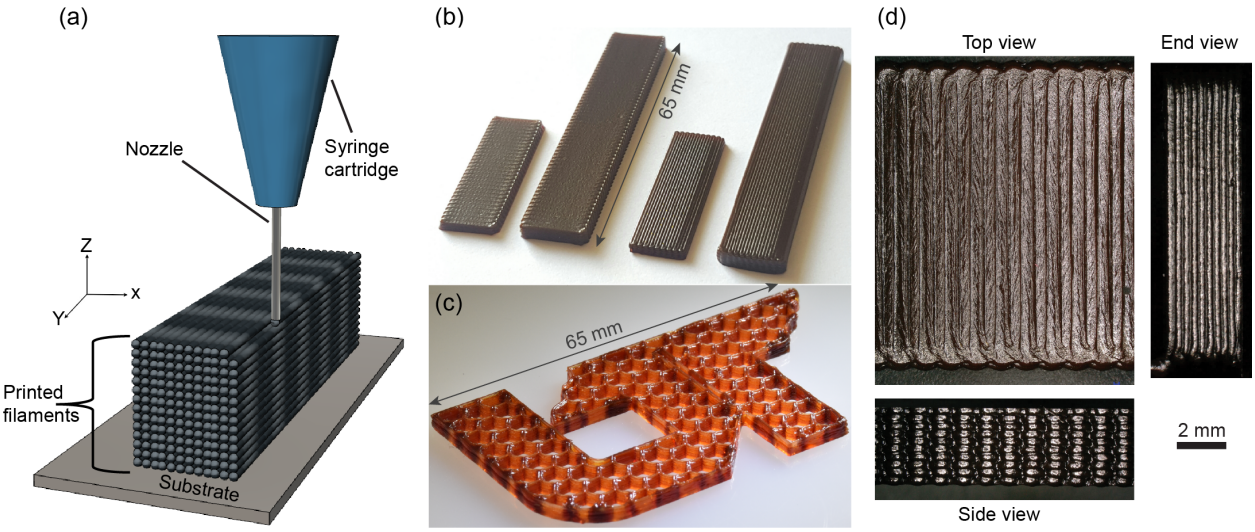

Figure 3.1: (a) Schematic illustration of direct ink writing 3D-printing. (b) 3D-printed epoxy/NC rectangular specimens for both flexural and DMA test characterization, with transverse specimens on the left and longitudinal specimens on the right. (c) 3D-printed University of Tennessee logo with honeycomb infill. (d) Top, side, and end view optical micrographs of a transverse flexure specimen printed using the 12.5 wt.% NC ink formulation.

AM of thermoset polymers show significant promise [96]. Additionally, with thermoset materials printed using DW, curing occurs well after deposition, so that chemical crosslinks form between printed layers, potentially leading to drastic improvements in bond strength between layers compared to printed thermoplastics, which are plagued with low strength in the build direction [3, 31, 67].

Here, we report the effects of alkyl quaternary ammonium-functionalized NC platelets on the rheological, printing, thermal, and mechanical properties of epoxy/NC nanocomposites fabricated via DIW 3D-printing. In our approach, the NC is used as both the viscosifying agent to impart beneficial rheological properties that enable DIW printing, and as mechanical reinforcement in the cured composite. Inks are formulated containing fixed amounts of epoxy resin and NC platelets up to 12.5 wt.%. The rheological properties of each ink formulation are experimentally investigated using parallel plate rheometry, and the thermo-mechanical properties of the printed composites are measured using 3-pt flexural testing, nanoindentation mapping, thermo-gravimetric analysis (TGA), and dynamic mechanical analysis (DMA). The effect of deposition on the orientation of NC platelets and associated anisotropic strength and stiffness is probed by testing specimens parallel (hereafter referred to as longitudinal specimens) and transverse (hereafter referred to as transverse specimens) to the printing direction. Additionally, nanoindentation mapping is employed to probe the local elastic modulus property within a single printed epoxy/NC filament (or road). Cast and printed behavior is compared for one ink formulation, and a control ink formulated using isotropic FS is also investigated for comparison. Good printing behavior is observed in NC inks with shear yield stress values greater than ∼300 Pa, and observed strength values are up to ∼5x higher than those reported in [22] for epoxy/NC DIW inks without fibers, suggesting there is great potential for further development of this material system for additive manufacturing. Finally, print patterns and degree of NC orientation are characterized using polarized optical microscopy (POM) and micro-beam small-angle X-ray scattering (μSAXS). Results establish explicit relationships between visible optical birefringence patterns, local and bulk mechanical properties, and filler orientation within printed composites.

3.3 Experimental

3.3.1 Materials

The epoxy resin used in this study is Epon 826 epoxy resin (Momentive Specialty Chemicals, Inc., Columbus, OH), a Bisphenol A diglycidyl ether (DGEBPA) resin with 178-186 weight per epoxide, and density of 1.162 g/cc. 1-Ethyl-3-methylimidazolium dicyanamide (EMIM DCA) (Basionics VS 03, Sigma-Aldrich, Inc., St. Louis, MO) or dicyandiamide (DICY) powder (Amicure CG-1200G, Evonik Industries AG, Essen, Germany) was used as a latent curing agent for the epoxy resin. Imidazole-based curing agent (VS 03) results in inks with up to one month of shelf stability at room temperature and also imparts a characteristic reddish-brown to black color to the cured composite [53]. Garamite 7305 NC (BYK-Chemie GmbH, Wesel, Germany) with a specific density of 1.5-1.7 g/cc was utilized as the nano-scale filler material. Garamite 7305 is part of BYK's patented Mixed Mineral Thixotrope technology and is comprised of a blend of benzalkonium sepiolite and benzalkonium montmorillonite (https://Specialchem, https://BYK), alkyl quaternary ammonium-modified silicates with fibrous and layered crystal structures, respectively [9, 134, 5, 87]. As described in the following sections, this NC blend readily disperses in epoxy and other polar polymer resins and imparts strong rheology modification at fairly low loading. Additionally, one ink formulation was made using fumed silica (FS) (Cab-o-sil TS-720, Cabot Corporation, Alpharetta, GA) instead of NC as a control ink for comparison. FS is often used as a viscosifyer in epoxy resins, and has been previously demonstrated to yield 3D-printable epoxy inks [14, 91, 73]. FS particles, however, do not possess strong anisotropy, so they would not be expected to adopt any preferred orientation during the printing process. Comparisons between NC- and FS-based inks may thus provide greater insight into the specific effects of the printing process and filler type on the mechanical properties of 3D-printed composites.

3.3.2 Ink formulations

The inks were prepared by mixing the epoxy resin with appropriate amounts of NC (or FS), using a centrifugal planetary SpeedMixer (FlackTek, Inc., Landrum, SC) in 185-mL plastic

containers. Six formulations, plus the control, were prepared using 30 g of Epon 826 resin and 1.5 g of the curing agent (VS 03). The contents were mixed under vacuum at 0.1 atm for 60 seconds at 1700 rpm. Next, the nanofiller was added, followed by 60 seconds of mixing at 1700 rpm and 0.1 atm. After mixing with the nanofiller, the sides of the container were scraped with a spatula and mixed for an additional 60 seconds at 1800 rpm and 0.1 atm to make sure that the NC was completely dispersed and the mixture was bubble free. The compositions of all NC ink formulations are summarized in Table 3.1. The control epoxy/FS ink was formulated with 10 wt% FS. The 10 wt% FS was identified as a suitable amount to modify the viscosity of the epoxy resin and to enable printing of stable mechanical test specimens (see Section A.1 for more details). An additional ink containing 10 wt% NC was formulated with the Amicure curing agent instead of VS 03, and will be refereed to as the NC/Amicure ink.

3.3.3 3D printing

Ink formulations containing 7.5, 10 and 12.5 wt.% NC and 10 wt.% FS were printed using a custom DIW 3D-printing platform comprised of a 3-axis positioning stage (Shopbot Tools, Inc., Durham, NC), solenoid valves, and a voltage controlled air pressure regulator (Omega Engineering, Inc., Norwalk, CT). Inks were manually loaded into 10 cc syringe barrels (Nordson EFD, Westlake, OH) using a spatula. To eliminate bubbles, all loaded syringe barrels were centrifuged at 4500 rpm for 10 minutes using a SorvallTM ST-8 Centrifuge (ThermoFisher Scientific, Waltham, MA). The RPM and duration were chosen empirically to effectively remove bubbles without causing any separation of the NC from the epoxy resin, following [22]. Following the centrifuging process, the loaded syringe was inserted into a pressure adapter (HP3, Nordson EFD, Westlake, OH). A 634-micron-diameter straight metal Luer-lock syringe tip (McMaster-Carr, Elmhurst, IL) was used to print all samples. The layer height and filament-to-filament spacing were specified as 0.6 and 0.85 times the nozzle diameter (380.4 μm). Longitudinal and transverse test specimens were printed using translation speeds of 30 mm/s and 20 mm/s, respectively. The NC/Amicure ink was printed using a tapered metal nozzle tip (S-type, GPD, Grand Junction, CO) with an outlet diameter of 609 μm, and at a print speed of 20 mm/s using 50 psi (344.7 KPa) extrusion pressure –

Table 3.1: Compositions of epoxy/NC formulations

Ink	Resin (g)	VS 03 (g)	NC (g)	NC (wt.%)	NC (calculated vol.%)	Density (g/cc)
1	30	1.5	0.00	0.0	0.0	1.190
2	30	1.5	0.81	2.5	1.871	1.206
3	30	1.5	1.66	5	3.77	1.214
4	30	1.5	2.55	7.5	5.69	1.220
5	30	1.5	3.50	10	7.63	1.230
6	30	1.5	4.50	12.5	9.60	1.250

applied to the ink without a pressure adapter. Ink formulations with 0, 2.5 and 5 wt.% NC were too fluid to 3D print and were instead cast into printed silicone molds of the same dimensions as the printed samples. To provide a comparison between cast and printed specimens of the same formulation, additional specimens were made using the formulation containing 5 wt.% NC by 3D-printing it into a silicone mold. In this manner, any orientation of the NC that results from the printing process should be preserved, and may manifest in the mechanical properties or microstructural observations. All inks were printed or cast onto glass substrates covered with PTFE-coated aluminum foil (Bytac, Saint-Gobain Performance Plastics, Worcester, MA) to prevent a permanent bond to the substrate. All samples were pre-cured at 100 °C for 24 hours, allowed to cool down at room temperature, removed from the substrate, and finally cured at 220 °C for 2 hours on an uncoated glass substrate. The g-code defining the print path for all test samples was generated using custom programs written with Scilab software (Scilab Enterprises, France). Representative 3D-printed DMA and flexure samples are shown in Figure 3.1b. The print path for the UT logo shown in Figure 3.1c was generated from a computer-aided design (CAD) solid model that was converted to an .stl file and sliced for FFF printing using the open source slicing software, Slic3r (http://slic3r.org/). The software-generated tool path was then converted for use on our direct-write printer using a custom conversion program. The density of printed, cured specimens was measured using the Archimedes method.

3.3.4 Ink rheology

Rheological properties of the inks were measured using a Discovery HR-2 Rheometer (TA Instruments, New Castle, DE) with a gap size of 500 μm for all inks. All measurements were preceded by a two minute conditioning step at a constant shear rate of 0.1/s. Oscillatory stress sweeps were performed at controlled oscillatory stresses from (5 to 5000 Pa) and continuous flow sweeps were performed at controlled shear rates from (0.02 to 100 1/s). Tests were conducted at ambient lab temperature (∼21 °C).

3.3.5 Thermal characterization

Thermo-gravimetric analysis (TGA) was carried out on a Q500 by TA instruments. The tests were run to 800 °C at a ramp rate of 10 °C/min under both air and nitrogen atmospheres. Samples were cut from cured printed or cast bars using a low speed sectioning saw (TechCut 4, Allied High Tech Products, Inc., Rancho Dominguez, CA). Dynamic mechanical analysis (DMA) was performed on a Discovery HR-2 Rheometer using three-point bending configuration at a constant oscillation frequency of 1 Hz. DMA test specimens had nominal dimensions of 32 x 12 x 2 mm, and testing was conducted over a temperature range of 25 – 250 °C at a heating rate of 3 °C/min.

3.3.6 Mechanical characterization

Three-point flexural tests were conducted at room temperature on an electromechanical load frame (Model 45, MTS Systems Corporation, Eden Prairie, MN, USA) using a 1 kN or 5 kN load cell (typical loads were 200-300 N and no systematic difference was observed between measurements from the 1 kN and 5 kN load cells). Flexural test samples had target as-printed dimensions of 65 x 12.7 x 3.2 mm, and were tested using a span length of 50 mm and cross-head speed of 1.3 mm/min. Edges and surfaces of the flexural tests samples were ground or machined smooth prior to testing, so that the final as-tested depth of the majority of samples fell between 2.95 mm and 3.15 mm, resulting in a span-to-depth ratio of between 16.95:1 and 15.87:1, which is very close to the 16:1 span-to-depth ratio specified in ASTM D790 [7]. Nanoindentation mapping was performed on a single, cylindrical filament (or road) printed with NC/Amicure ink to spatially map the the elastic modulus property as a function of the radial distance. A commercial nanoindenter (Nanomechanics, iMicro Nanoindenter, Oak Ridge, TN) was used to generate 20 x 20 (sepearted by 5 μm) and 2 x 9 indents (sepearted by 40 μm) with maximum test loads of 10 mN and 50 mN, respectively. The printed single roads used for nanoindentation were mounted in an epoxy resin and then polished using a MetaServ 250 (Buehler, Lake Bluff, IL). Polishing was conducted with silicon carbide (SiC) abrasive papers down to 800 grit size, and then with aluminum oxide powder down to 0.05 μm.

3.3.7 Microscopic characterization

Optical micrographs were recorded using a VHX-5000 digital microscope (Keyence Corporation of America, Itasca, IL). Additionally, polarized optical microscopy (POM) was performed on thin slices of printed specimens using transmitted light to observe birefringence patterns associated with the printing process. Slices were cut using a low speed sectioning saw (TechCut 4, Allied High Tech Products, Inc. Rancho Dominguez, CA). The surfaces of the cut slices were then polished using aluminum-oxide lapping films (Allied High Tech Products, Inc. Rancho Dominguez, CA). The cut slices had comparable thicknesses ($\sim$ 0.5 mm thick) and were inspected with the same light intensity. POM was performed using the same VHX-5000 digital microscope, after equipping it with two polarized filters (i.e. polarizer and analyzer). Scanning electron mciroscopy (SEM) was performed on a Phenom Desktop SEM (Nanoscience Instruments, Inc, Phoenix, AZ) to observe the failure initiation points of fractured flexure specimens. Scanning micro-beam small-angle X-ray scattering (μSAXS) data for an epoxy/NC/Amicure printed slice from [114] was used to compare with POM observations and nanoindentation measurements. Full details of these measurements and analysis are available in Trigg et al. [114].

3.4 Results and Discussion

3.4.1 Ink rheology

Curves of the apparent viscosity as a function of shear rate are plotted in Figure 3.2a for each ink formulation investigated. The neat epoxy resin exhibits nearly rate-independent viscosity at $\sim$10 Pa.s for the range of shear rates probed. The addition of NC drastically increases the apparent viscosity and shear thinning behavior of the epoxy resin. At low shear rates (10^{-2} s^{-1}), the apparent viscosity increases to 3000 Pa.s for 2.5 wt.% NC, and up to 4 x 10^5 Pa.s for 12.5 wt.% NC. At shear rates comparable to those experienced by the material during deposition ($\sim$50 s^{-1}) the apparent viscosity values range from 10 - 100 Pa.s, a much smaller range indicative of the high degree of shear thinning imparted by the NC. The shear thinning behavior of complex fluids can be quantified by fitting the apparent viscosity versus

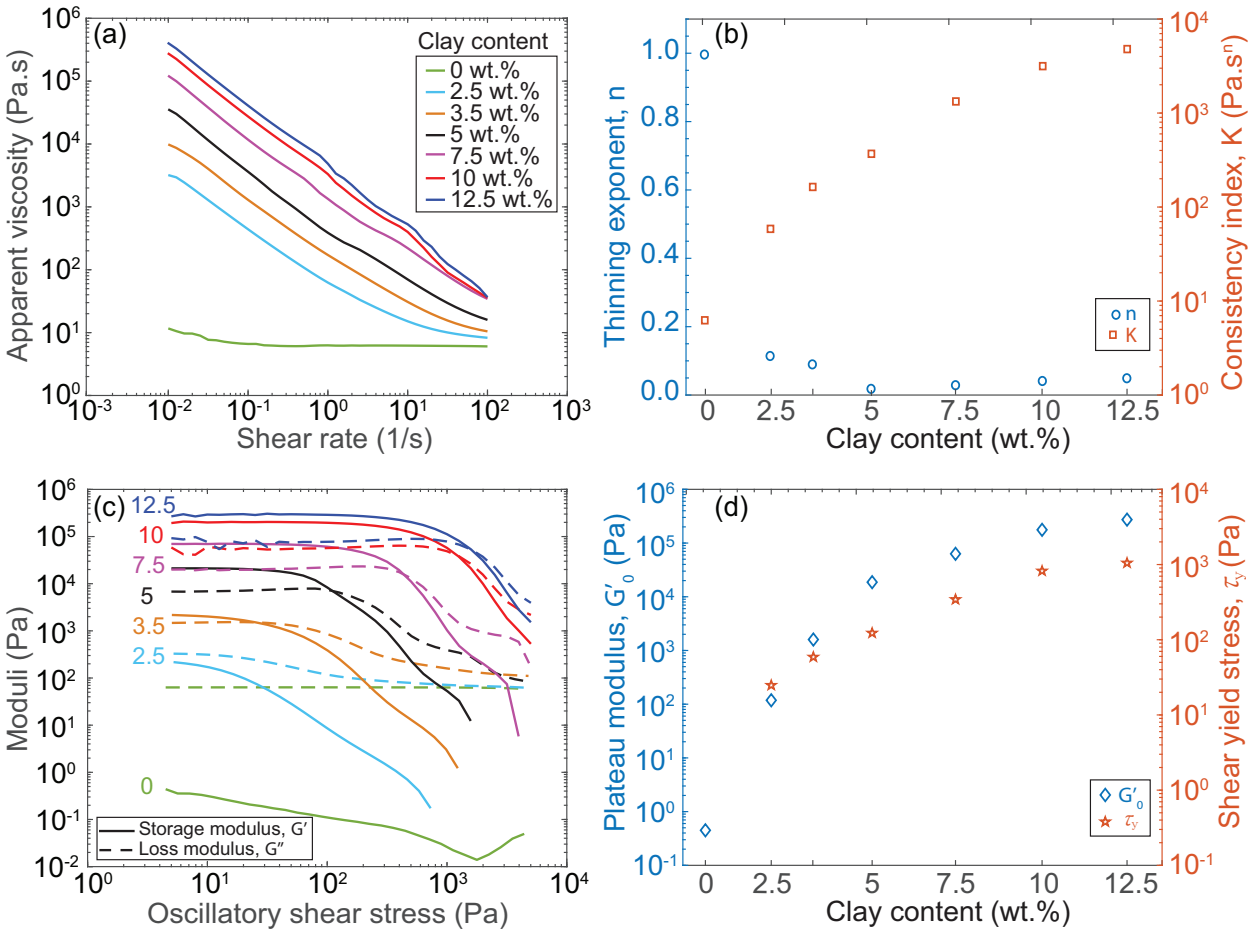

Figure 3.2: Rheological behavior of all epoxy/NC formulations investigated. (a) Log-log plots of apparent viscosity as a function of shear rate. (b) The shear thinning exponent, n, and the consistency index, K, computed by fitting the linear portions of the viscosity curves in (a) with the power-law fluid model described by equation (1). (c) Log-log plots of storage and loss moduli as a function of oscillatory shear stress. (d) The plateau elastic modulus and the shear yield stress values for each formulation, measured from (c).

shear rate curves to a power law of the form:

$$\eta = K\dot{\gamma}^{n-1} \tag{3.1}$$

where K is the consistency index and n is the flow index. The flow index, n, describes the rate dependence of the fluid; for shear thinning fluids, n $<$ 1, while for shear thickening fluids, n $>$ 1, and for Newtonian fluids, n = 1. On a log-log plot of apparent viscosity vs shear rate, as in Figure 3.2a, the slope of the linear portion of the apparent viscosity curve equal to 1-n. Numerical values for n and K were computed from the rheology curves by linear regression over the linear portions of the curves (i.e. between 1 and 100 s^{-1} for the neat resin, and between 0.01 and 1 s^{-1} for all other formulations). The computed n and K values are plotted in Figure 3.2b for all formulations. It can be seen that the consistency index correlates strongly with the amount of NC, while presence of any NC results in a flow index much less than one, without a strong correlation between amount of NC and flow index. All formulations containing greater than 2.5 wt.% NC exhibit flow index values less than 0.1, indicating superior shear thinning behavior. It is worth noting that the precise value of the flow index is very sensitive to the exact range of the apparent viscosity curves used in the linear regression. For consistency, we have used the same range for all curves containing NC, but small adjustments to the range change the computed values of flow index slightly. Dedicated studies will be needed to investigate the relationships between potential variations in the degree of exfoliation of the NC in these systems and subtle changes in the flow and consistency indices. For the purposes of this study, all formulations containing NC exhibit favorable shear thinning.

Plots of the storage (G') and loss moduli (G'') are shown on Figure 3.2c. The neat resin displays a stress-independent loss modulus value of 100 Pa that is approximately three orders of magnitude larger than the storage modulus, indicating that the neat resin behaves predominantly as a viscous fluid. The addition of NC increases both the loss and storage moduli. At higher NC content (>2.5 wt.%) the storage modulus exceeds the loss modulus, and the inks begin to display solid-like behavior at low shear stress. In this case, the storage modulus remains constant over a certain range. This constant value is known as the plateau

elastic modulus, G'_0, and for the formulations characterized, the values range from 1.87 x 10^3 Pa, for the formulation containing 3.5 wt.% NC, up to 2.7 x 10^5 Pa for the formulation containing 12.5 wt.% NC. For those formulations possessing solid-like behavior, as the applied stress increases above a certain value, the storage modulus decreases precipitously to a value below that of the loss modulus, and more liquid-like behavior is obtained. This transition corresponds to the shear yield stress, τ_y, which can be measured from the intersection point of two tangent lines drawn from the stress-independent elastic region of the storage modulus curve and the shear thinning portion of the storage modulus curve [25]. Shear yield stress values increase with increasing NC content from 59 Pa for the 3.5 wt.% formulation to 1.05 x 10^3 Pa for the 12.5 wt.% formulation. The values of plateau elastic moduli and the shearyield stress for each formulation are plotted in Figure 3.2d and all measured rheological parametersare summarized in Table 3.2.

3.4.2 3D printing and sample fabrication

Through a series of printing tests, it was observed that inks containing 5 wt.% NC and less, did not possess sufficiently solid-like behavior to print multiple layers without significant flow and spreading of the lower layers, so flexural specimens were cast, rather than printed. The ink formulations containing greater than 5 wt.% NC were able to be extruded through the deposition nozzle reliably at and above 120 psi (827 kPa), and recovered sufficiently solid-like behavior after deposition to enable flexural test specimens comprising ten layers to be printed with minimal spreading or other geometric distortion. Because of the rheological requirements of 3D printing, the printable formulations were not able to be cast for comparison. Instead, the 5 wt.% NC formulation was printed into silicone molds in the longitudinal and transverse motifs to provide a direct comparison between casting and 3D printing using the same ink.

Optical micrographs of the ends of representative longitudinal flexure specimens are shown in Figure 3.3 along with corresponding cross-sections of the same bars. In each of the views, the axis of the printed filaments is normal to the plane of the image, so that the surfaces shown in Figure 3.3a-c are where the print head makes a U-turn, as shown in Figure 3.1d.For the ink containing 7.5 wt.% NC (Figure 3.3a), the surface of the printed –

Table 3.2: Rheological properties of epoxy/NC formulations

NC (wt.%)	G'_0 (kPa)	τ_y (Pa)	K (Pa.s^n)	n
0.0	–	–	6.24	0.995
2.5	0.1183	24.8	58.6	0.1130
3.5	1.622	58.9	163.6	0.0885
5	18.69	122.9	369	0.00324
7.5	63.0	343	1329	0.0276
10	176.3	822	3160	0.0399
12.5	273	1050	4790	0.0479

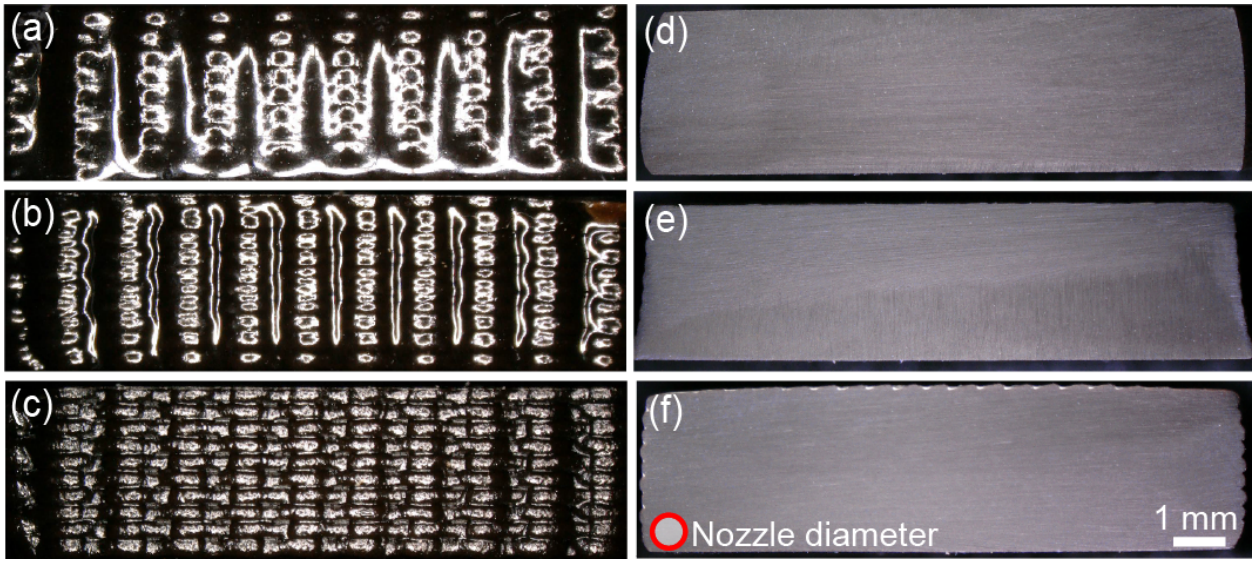

Figure 3.3: Optical micrographs of the as-printed ends of representative longitudinal flexural bars along with corresponding optical micrographs of cross-sections of the same bars. (a) and (d) contain 7.5 wt.% NC, (b) and (e) contain 10 wt.% NC, and (c) and (f) contain 12.5 wt.% NC. These micrographs demonstrate that all formulations can form fully dense components without any voids trapped between filaments.

part is smooth and shiny. The locations of individual printed filaments are still visible as smooth peaks or undulations in the surface, but most of the definition is lost because the filaments have flowed together during deposition. As NC content and shear yield stress increase, the individual filaments in each layer become more defined on the exterior surface of the printed bars. On the specimen printed using the 10 wt.% NC ink (Figure 3.3b), the printed layers have mostly coalesced, but the repeated identical print path for each layer results in columnar features on the surface that indicate the print paths. For the sample printed using the 12.5 wt.% NC formulation (Figure 3.3c), the surface features are sharp, and all layers and filaments are visible. Cross-sections of printed flexural bars (Figure 3.3d-f) show that, despite the stark difference in surface appearance (and rheological properties) between the inks with different NC content, fully dense, pore-free components can be successfully printed with a wide range of ink compositions, provided flow rate, layer height, and print speed are chosen appropriately.

As an example of printing-related voids that can occur if printing parameters are not carefully tuned, fracture surfaces of two specimens printed using the 12.5 wt.% NC formulation are shown in Figure 3.4. The fracture surface shown in Figure 3.4a and c is the result of carefully tuned print parameters for this ink and nozzle combination. No voids are visible, nor is any evidence of the print path. The surface shown in Figure 3.4b and d contains a regular array of round voids with a characteristic spacing equal to the nozzle diameter, very similar to those observed in thermoplastic 3D printing. This sample was printed with a flow rate that was slightly too low for the print speed. Interestingly, some of the voids in Figure 3.4d can be seen to have been filled in with what appears to be neat epoxy resin (indicated with black arrows). It is possible that neat resin may have flowed from the surrounding material as a result of surface tension during the curing process. These observations raise the possibility that thermosets may be able to be designed to be more robust against printing-related voids than thermoplastics. However, it is impossible to make any definitive statements based only on these preliminary observations, and further work would be needed.

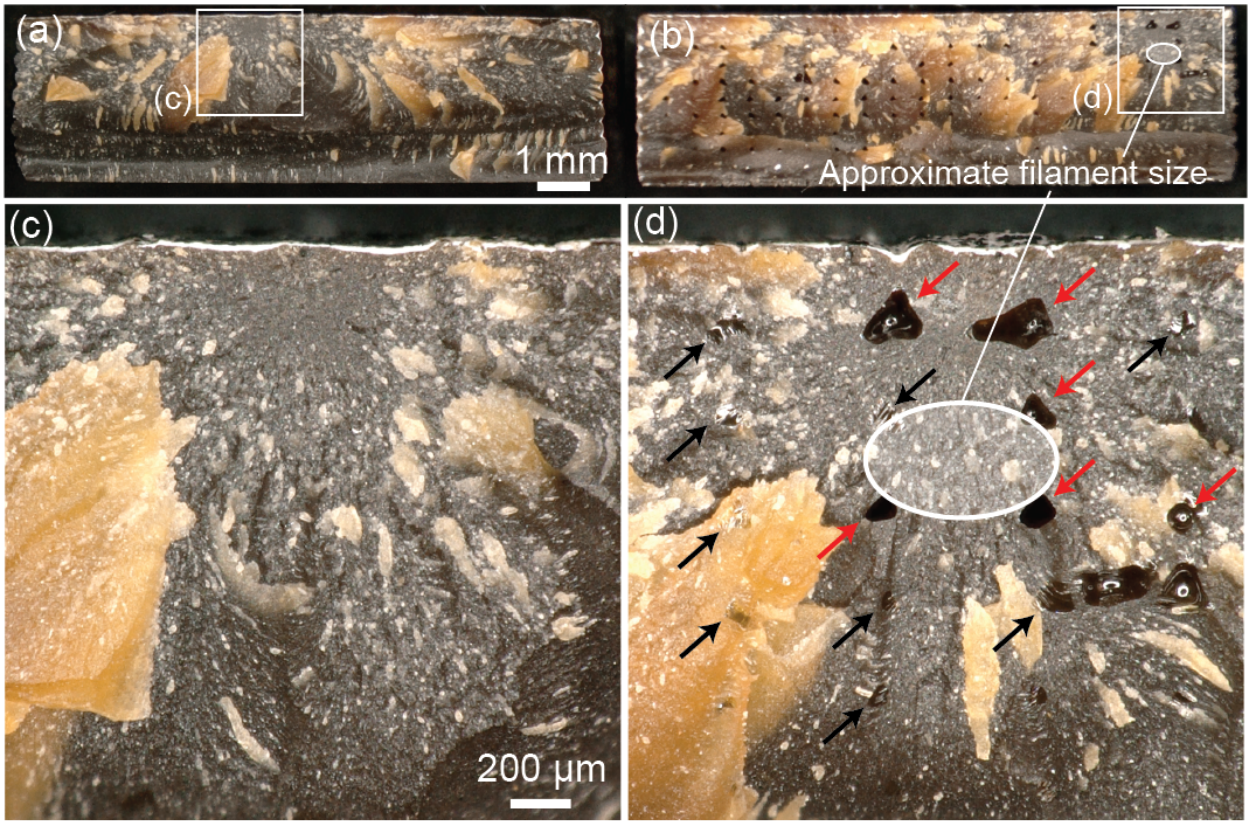

Figure 3.4: Optical micrographs showing printing-related voids in a longitudinal flexure specimen containing 12.5 wt.% NC. (a) Low-mag image of the fracture surface of a pore-free sample. (b) Low-mag image of the fracture surface of a sample containing a regular array of interfilamentary voids resulting from a lower ink flow rate during printing. (c) High-mag micrograph of the pore-free surface shown in (a). (d) High-mag micrograph of the surface containing voids. The approximate filament size is indicated by the white oval. Empty pores are indicated with red arrows, while filled pores are indicated with black arrows.

3.4.3 Mechanical behavior

The elastic modulus, strength, and strain-to-failure for all cast and printed flexural specimens are plotted in Figure 3.5 and summarized in Table 3.3. Flexural modulus values increase monotonically with increasing NC content from 2.9 GPa for the cast neat epoxy up to 4.2 GPa and 3.8 GPa for the longitudinal and transverse samples containing 12.5 wt.% NC, respectively (Figure 3.5a). Flexural strength values (Figure 3.5b) for all samples tested range from 80 MPa to 143 MPa, with a monotonic increase in strength with NC content for the cast and printed specimens.

Among the printed specimens, longitudinal samples exhibited considerably higher strength and stiffness, suggesting that the printing process imposes a preferred orientation on the NC that leads to anisotropic properties in printed parts. Interestingly, the FS ink exhibits substantially less anisotropy in both strength and stiffness than the NC-containing formulations, although a small amount of anisotropy does remain. This suggests that a small portion of the anisotropy observed in the mechanical tests may be attributed to the printing process alone, while the majority appears to depend on the aspect ratio of the filler material. The fact that the printed 5 wt.% formulation exhibited anisotropy and lower strength than the cast 5 wt.% formulation would seem to corroborate this interpretation. Strain-to-failure for all flexural tests ranged from 3 to 5 (Figure 3.5c). Longitudinal specimens failed at higher strains than transverse specimens for all printed specimens, including the FS. This may indicate that strength-limiting flaws are more likely to occur between filaments where they would more strongly affect the strength and strain-to-failure of the transverse specimens.

The nanoindentation mapping results are shown in Figure 3.6. Figure 3.6a shows an optical micrograph of the end view of a printed epoxy/NC/Amicure single-road mounted in epoxy, including the selected regions for nanoindentation testing (marked by black boxes). Figure 3.6b displays a mapping of the elastic modulus property over an area of 100 x 100 μm^2 using an array of 20 x 20 indentations separated by 5 μm. Figure 3.6c displays a mapping of the elastic modulus property over an area of 400 x 40 μm^2 using an array of 2 x 9 indentations separated by 40 μm. In both mappings, higher modulus values (4 - 6.2 GPa) are obtained near the exterior (i.e. outer-most boundary) of the printed road, while the –

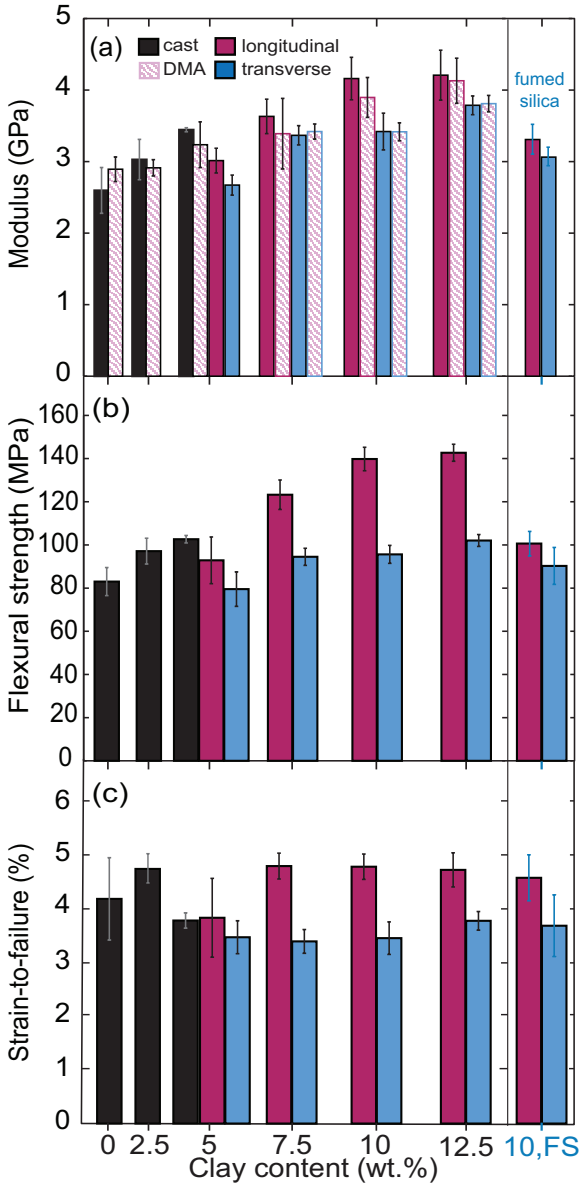

Figure 3.5: Bar plots of the average values of (a) flexural modulus, (b) flexural strength and (c) strain-to-failure for all tested specimens. The room temperature storage modulus values measured by DMA are also shown in (a) for comparison. The flexural properties of the epoxy/FS printed specimens are also shown on the right side of the bar plots, indicated by FS. Error bars indicate the standard deviation in measured values

Table 3.3: Mechanical properties of cast and 3D-printed epoxy nanocomposites

Specimen configuration	NC (wt.%)	Flexural modulus (GPa)	Storage modulus (GPa)	Flexural strength (MPa)	Strain -to-failure (%)	Number of tested specimens
Cast	0	2.60 ± 0.32	2.89 ± 0.17	83.0 ± 6.51	4.17 ± 0.77	5
	2.5	3.03 ± 0.28	2.91 ± 0.11	97.1 ± 5.99	4.73 ± 0.30	3
	5	3.45 ± 0.03	3.24 ± 0.32	102.7 ± 1.74	3.77 ± 0.14	3
Longitudinal	5	3.01 ± 0.17	-	92.9 ± 10.82	3.82 ± 0.73	6
	7.5	3.62 ± 0.24	3.50 ± 0.41	123.3 ± 6.83	4.78 ± 0.25	9
	10	4.16 ± 0.30	3.90 ± 0.28	140.3 ± 5.50	4.77 ± 0.24	10
	10,FS[a]	3.31 ± 0.21	-	100.6 ± 5.69	4.56 ± 0.43	9
	12.5	4.21 ± 0.35	4.13 ± 0.32	142.7 ± 3.95	4.70 ± 0.30	8
Transverse	5	2.67 ± 0.14	-	79.5 ± 8.00	3.46 ± 0.31	6
	7.5	3.37 ± 0.14	3.42 ± 0.11	94.5 ± 3.97	3.38 ± 0.22	10
	10	3.42 ± 0.26	3.42 ± 0.13	95.6 ± 4.17	3.44 ± 0.30	8
	10, FS[a]	3.06 ± 0.13	-	90.3 ± 8.56	3.67 ± 0.57	9
	12.5	3.79 ± 0.13	3.81 ± 0.12	102.1 ± 2.76	3.76 ± 0.17	8

[a]FS

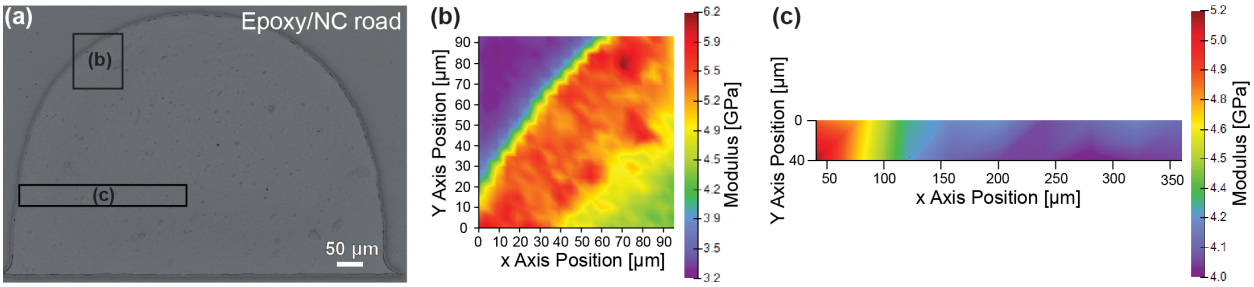

Figure 3.6: (a) Optical image of the end view of a printed epoxy/NC/Amicure single-road. The black boxes denote the regions of interest for nanoindentation testing. (b) Elastic modulus values of 20 x 20 indentations separated by 5 μm. (c) Elastic modulus values of 2 x 9 indentations separated by 40 μm. The single-road was printed at a print speed of 20 mm/s using a nozzle diameter of 609 μm.

interior of the road maintains lower modulus values (4 - 4.2 GPa). These observations indicate that the flow profile in the deposition nozzle induces a spatial orientation on the NC platelets with respect to the radial location, which leads to variations in the elastic modulus property in the printed part.

Representative fracture surfaces of the flexural specimens are shown in Figure 3.7. In all specimens, the mirror, mist, and hackle regions are apparent and indicate that failure initiated near center of the tensile surface (the top edge in the images). The fracture surface of the cast neat epoxy (Figure 3.7a) has a smooth glassy appearance typical of brittle unfilled epoxies, while the presence of NC leads to rougher fracture surfaces (Figure 3.7b-i) with a highernumber of flakes (the light tan regions in the micrographs) that indicate crack bifurcation and higher energy consumption during fracture. The fracture surfaces for the longitudinal and transverse printed specimens (Figure 3.7d-i) can be compared in the center and right columns, respectively. There is no evidence of the original print path, pores between printed filaments, or any delamination between layers, suggesting strong bonding between printed filaments and thorough crosslinking between layers.

Representative high magnification scanning electron micrographs of the failure initiation points are shown in Figure 3.8 for the 10 wt.% NC specimens, as well as the FS specimens. The point of failure initiation is visible in each micrograph as a light gray or white particle. These features do not appear to be pores, but may be dust or agglomerates of NC or FS. Interestingly, the features in the transverse specimens (Figure 3.8b and d) are considerable larger than those in the longitudinal specimens (Figure 3.8a and c). This may be a contributing factor to the decreased strength associated with the transverse specimens.

3.4.4 Thermal behavior

Thermograms and primary derivative plots are shown in Figure 3.9 for all formulations investigated, and data points for the initial degradation temperature (defined as the temperature at 5% mass loss, following Gu et al. [50]), the temperature at maximum degradation rate, and the char yield at 800 °C are summarized in Table 3.4 and Table 3.5 for air and nitrogen atmospheres, respectively. The presence of NC mildly accelerates the onset of thermal degradation and slightly reduces the temperature at which the maximum

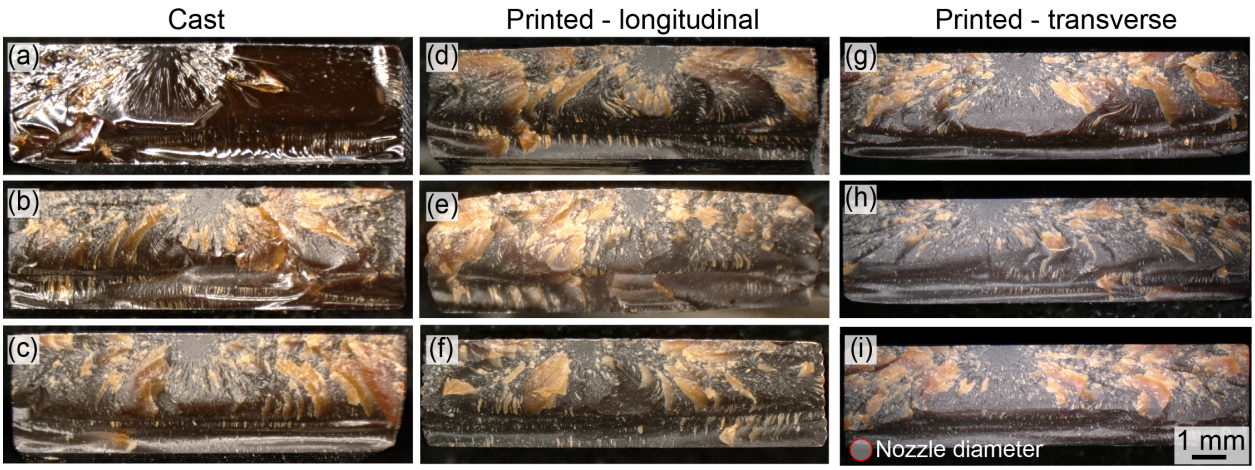

Figure 3.7: Optical micrographs of representative fracture surfaces of cast and printed flexure specimens containing (a) 0 wt.%, (b) 2.5 wt.%, (c) 5 wt.%, (d) and (g) 7.5wt.%, (e) and (h) 10 wt.%, and (f) and (i) 12.5 wt.% NC. No inter-filamentary voids are observed, indicating complete coalescence of printed filaments.

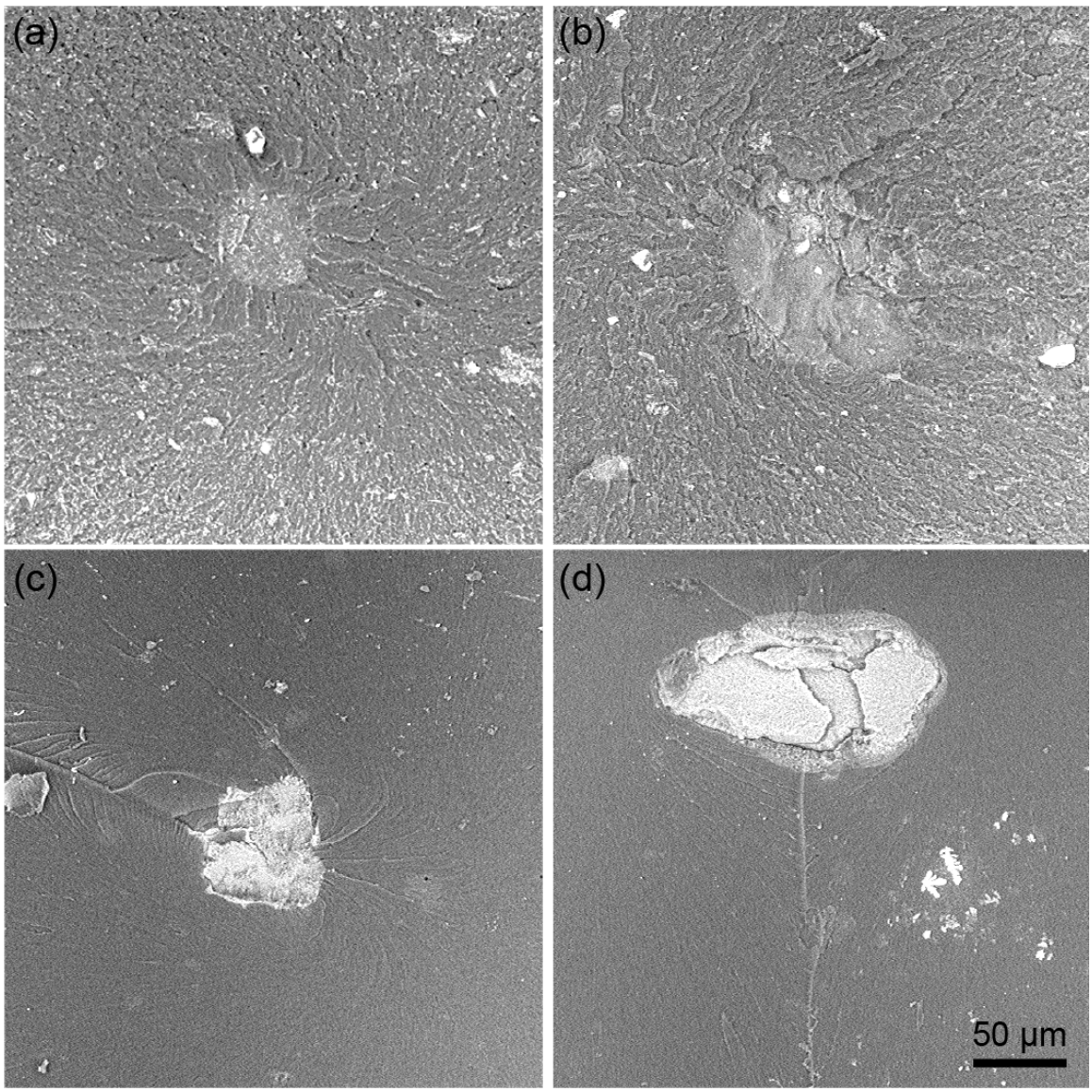

Figure 3.8: Scanning electron micrographs showing features of the point of failure initiation on the fracture surfaces of (a) a longitudinal specimen containing 10 wt.% NC, (b) a transverse specimen containing 10 wt.% NC, (c) a longitudinal specimen containing 10 wt.% FS, and (d) a transverse specimen containing 10 wt.% FS.

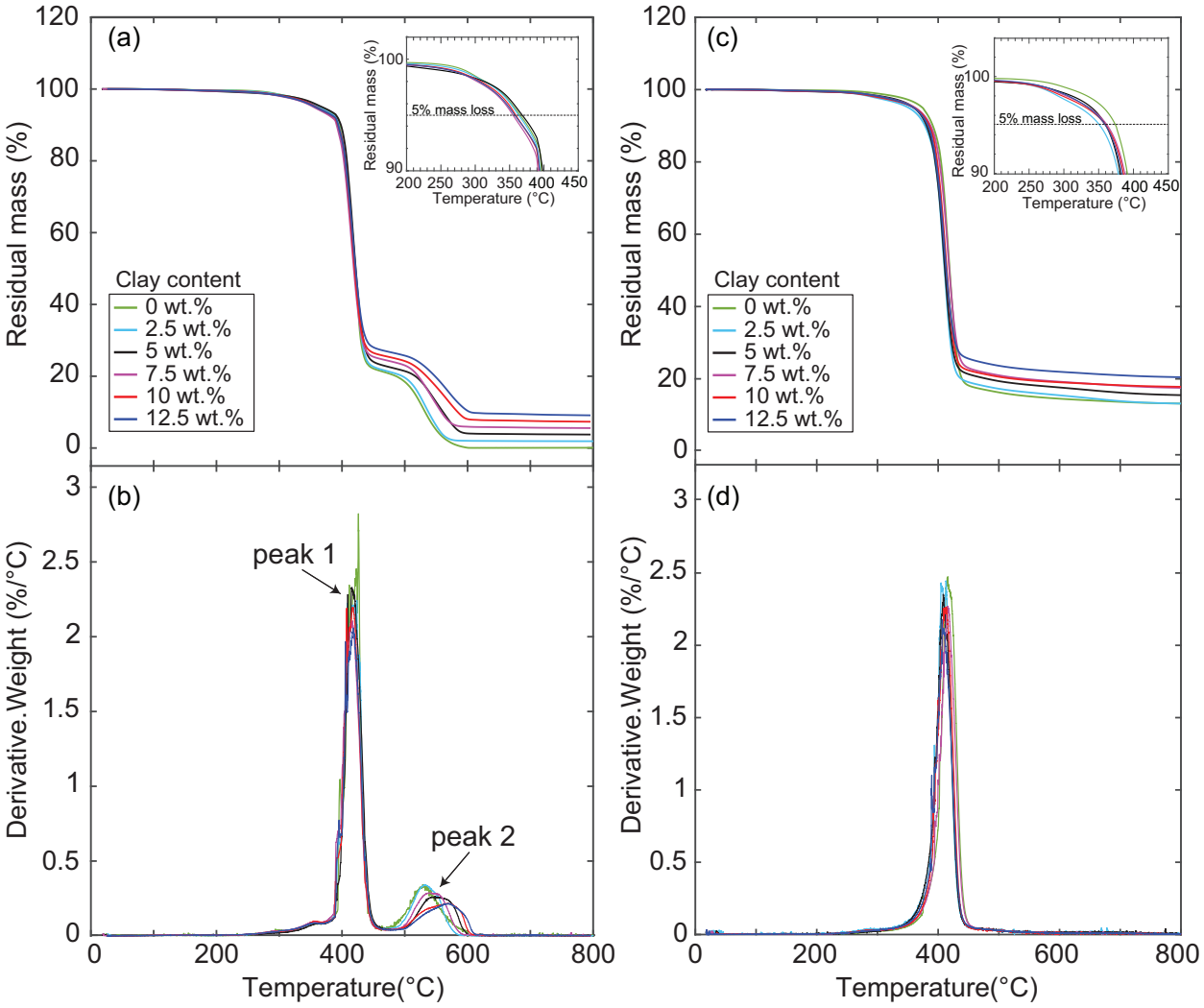

Figure 3.9: Thermograms and primary derivative plots for the epoxy/NC formulations in (a) and (b) air, and (c) and (d) nitrogen atmospheres.

Table 3.4: Thermogravimetric data for epoxy/NC composites in air atmospheres

NC (wt.%)	5 % mass loss (°C)	Peak loss rate (°C)		Char yield @ 800 °C (%)
		Peak 1	Peak 2	
0	365.1	426.2	528.7	0.074
2.5	362.8	419.1	534.6	1.90
5	368.1	415.8	547.9	3.76
7.5	354.8	416.6	539.3	5.55
10	358.8	417.8	569.6	7.33
12.5	357.5	417.9	568.8	9.11

Table 3.5: Thermogravimetric data for epoxy/NC composites in nitrogen atmospheres

NC (wt.%)	5 % mass loss (°C)	Peak loss rate (°C)	Char yield @ 800 °C (%)
0	374.2	416.0	13.2
2.5	351.1	412.9	13.2
5	360.1	408.8	15.5
7.5	362.0	415.8	17.5
10	359.9	413.1	17.8
12.5	359.4	406.8	20.5

degradation rate is reached in both nitrogen and air atmospheres. However, beyond the presence or absence of NC, the NC content does not strongly correlate with either measurement. The initial degradation temperature and the temperature at maximum degradation rate are not substantially different in nitrogen or air atmospheres, although the progression of thermal degradation clearly is. In air, mass loss slows substantially between 450 °C and 500 °C and accelerates again between 500 °C and 600 °C (Figure 3.9a and b), while in nitrogen, degradation occurs in one step with a significantly higher char yield at 800 °C for all formulations (Figure 3.9c and d).

The two-step degradation process in air is attributed to the competing formation and oxidation of intermediate carbonaceous products [134, 50, 99, 15], although Gu et al. point out that the exact mechanisms of this process are not fully understood [50]. The temperature at which the second peak mass loss rate occurs in air (Figure 3.9a) increases with NC content, from 529 °C for neat epoxy, up to 569 °C for the formulation containing 12.5 wt.% NC. These results are in good agreement with those reported by Camino et al. for similar epoxy/NC systems using an anhydride curing agent [15]. This shift in the second peak mass loss temperature with NC content is attributed to the excellent oxygen barrier properties of NCs, which slows the rate of oxidation of the char material [50, 15].

Storage modulus and loss tangent curves measured by DMA in 3-pt flexure for each of the formulations investigated are plotted in Figure 3.10, and the glass transition temperatures, T_g, measured using the peak of the loss tangent curve, are plotted in Figure 3.11. Storage modulus values at room temperature for each formulation are also plotted in Figure 3.5a with the modulus values measured during the quasistatic flexure testing. Elastic modulus measurements are broadly consistent between the two test methods. Peak loss tangent values range from 0.25 to 0.35 and T_g values range from 149 °C for the neat epoxy to 161 °C for the 7.5 wt.% NC formulation. For printed samples, the T_g measured for transverse samples is 2-5 °C lower than that for the longitudinal samples, indicating a potential effect of the printing process on the arrangement and orientation of the NC platelets.

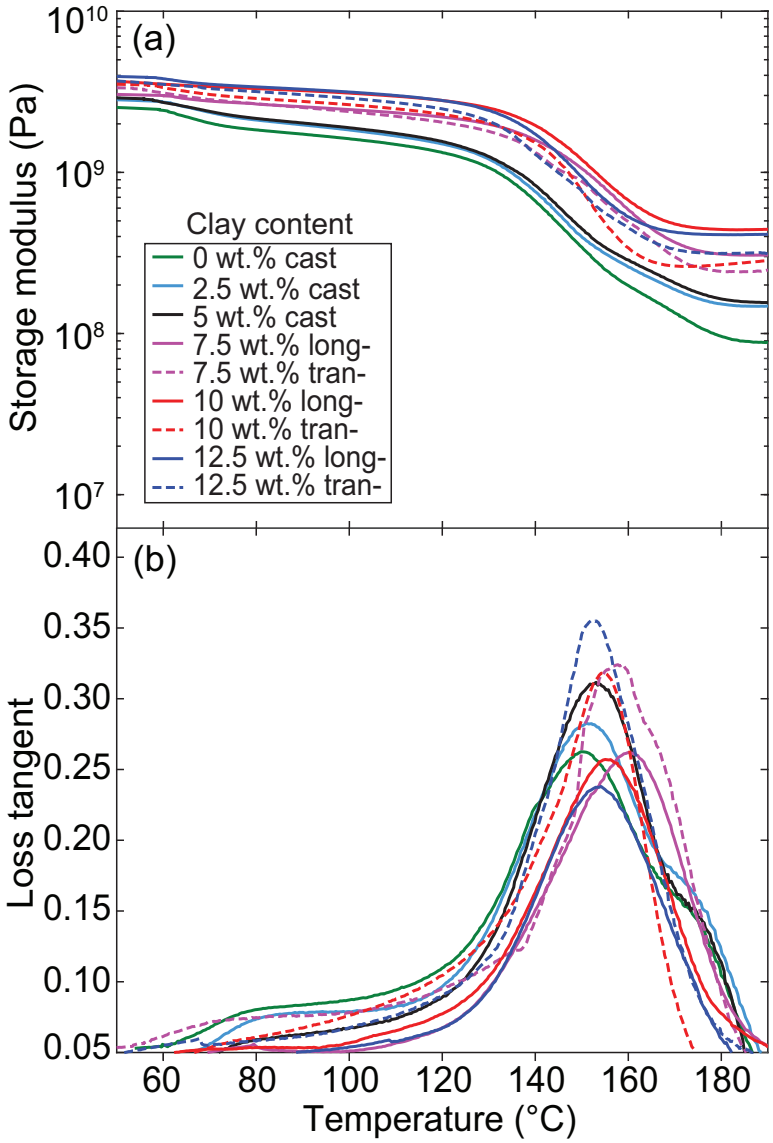

Figure 3.10: 3-pt. flexure DMA measurements. (a) Representative storage moduli as a function of temperature for all epoxy/NC formulations. (b) The corresponding loss tangent curves.

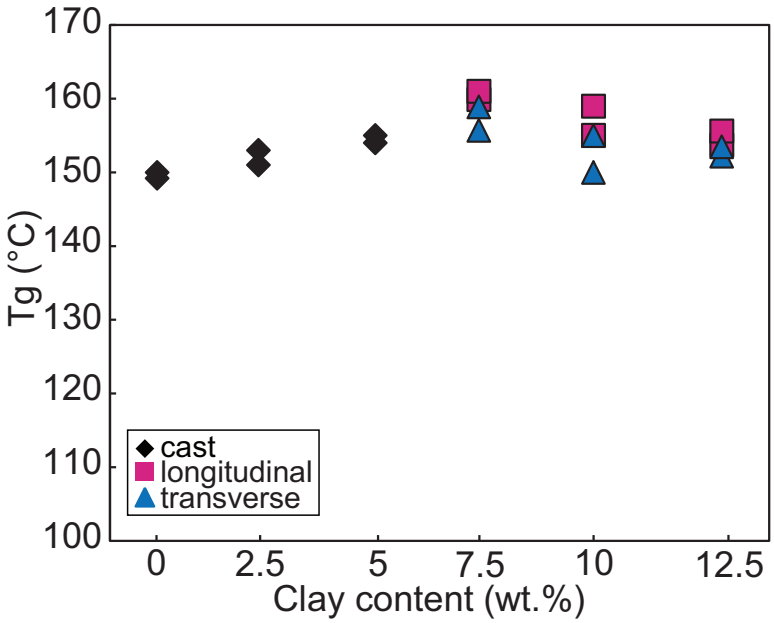

Figure 3.11: Glass transition temperatures, T_g, measured from the peak of the loss tangent curves.

3.4.5 Anisotropy due to printing

Although the NC particles that are employed here to impart both desirable rheological properties for printing and mechanical reinforcement after curing are significantly smaller than the deposition nozzle, much greater anisotropy in stiffness and strength in printed composites was observed when utilizing these high-aspect-ratio filler materials compared to FS, which has a more isotropic morphology. These observations indicate that the shear flow within the deposition nozzle may impose orientation on the NC platelets that leads to mechanical properties that differ parallel to the printed filament axis and transverse to it. Indeed, anisotropic mechanical properties associated with orientation of NC platelets resulting from shear flow has been observed in previous studies [42]. However, the fracture surfaces of printed longitudinal and transverse flexural specimens are not significantly different from those of the cast specimens, and no evidence of the original print path can be seen on the fracture surfaces or inferred from the mode of fracture.

In order to investigate the possible architecture imposed on the NC platelets by the printing process, thin slices of material were cut from all cast and all longitudinal printed flexure specimens, including the control samples utilizing FS. These slices were observed using transmitted light microscopy, with and without crossed polarizers. Micrographs of the thin sections are shown in Figure 3.12. In simple transmitted light mode (left-hand column), the interior of all samples appear nearly uniform with a darker perimeter that may be due to oxidation during curing, and a darker central region that may be due to elevated temperature resulting from the exothermic crosslinking reaction. The printed samples (Figure 3.12d-h) have characteristic surface pattern from the printing process, but otherwise there are few features to distinguish printed from cast samples. In cross-polarized light mode (right-hand column), however, the effects of NC and the printing process are stark. The crossed polarizers completely extinguish all light passing through the neat cast sample (Figure 3.12a), except for small regions at the corners of the sample where some residual stresses may be present, indicating an absence of birefringence throughout the bulk of the sample. The cast samples containing 2.5 wt.% and 5 wt.% NC (Figure 3.12b and c) exhibit a small amount of birefringence in a nebulous pattern throughout the cross-section, and the amount of birefrin-

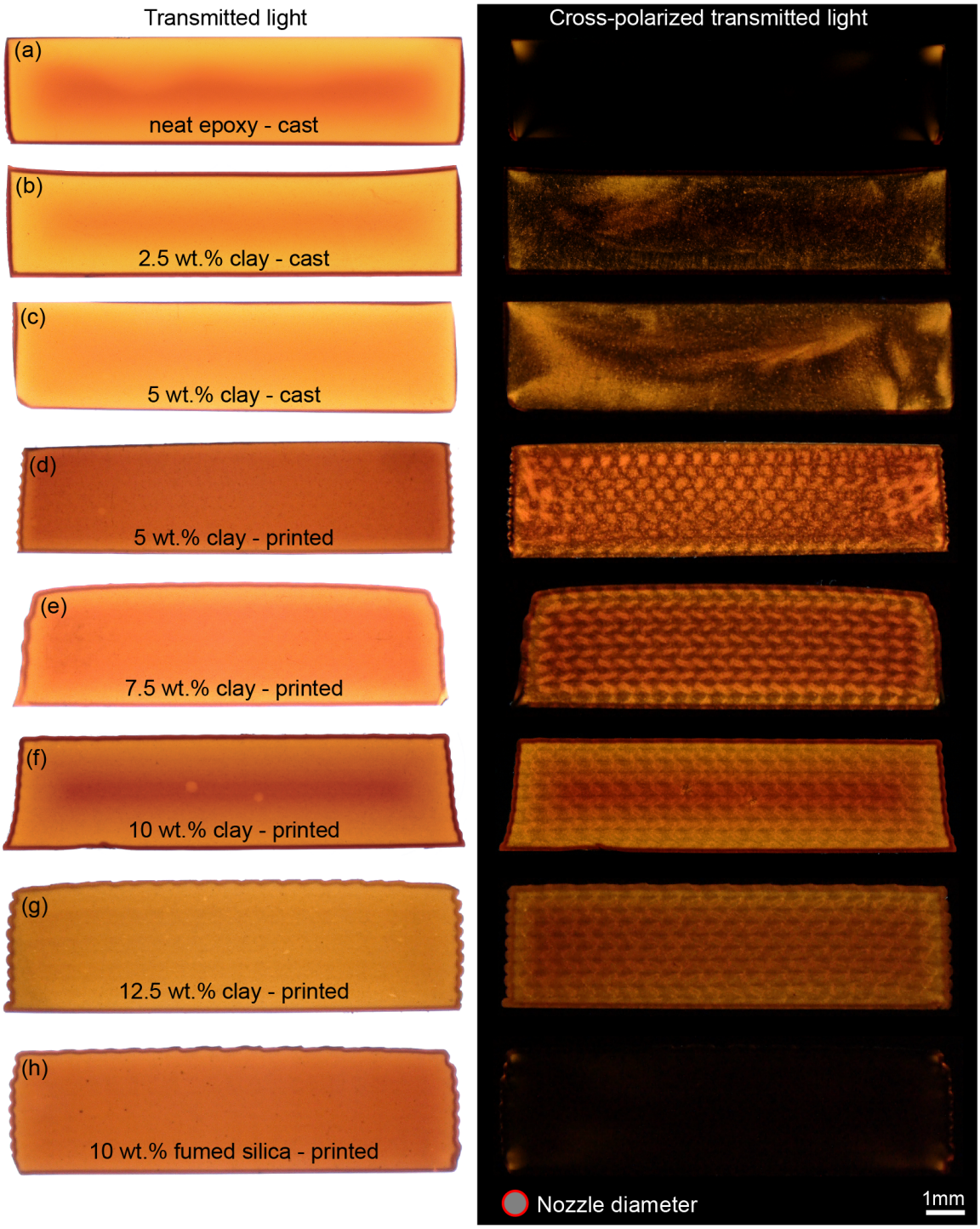

Figure 3.12: Optical transmitted light micrographs for polished thin slices (< 1 mm thick) cut from cast and printed specimens. (a) 0 wt.% cast, (b) 2.5 wt.% cast, (c) 5 wt.% cast, (d) 5 wt.% printed, (e) 7.5 wt.% printed, (f) 10 wt.% printed, (g) 12.5 wt.% printed epoxy/NC, and (h) 10 wt.% FS, printed. The left-hand column shows normal transmitted light, while the right-hand column shows the same samples observed using crossed polarizers. The patterned birefringence observed in (d)-(g) is indicative of preferred orientation in the NC as a result of the printing process.

-gence increases with NC content, suggesting that it is the presence of the NC that is causing birefringence. In contrast to the cast samples, the entire cross-sections of the printed NC samples (Figure 3.12d-g) are visible in cross-polarized light, indicating strong birefringence and orientation of the NC. In fact, a periodic array of higher and lower transmittance is apparent over the entire cross-section, and the size of the repeat units corresponds closely to the size of the nozzle used to print the sample. Images of the cast and printed 5 wt.% NC formulation (Figure 3.12c and d) allow direct comparison between the casting and printing process and highlight the effects of the high shear flow and discrete deposition process associated with DIW 3D printing. Interestingly, the printed FS sample exhibits minimal birefringence (Figure 3.12h), comparable to the unfilled cast epoxy. These observations provide clear evidence that the printing process imposes order on the NC in the nanocomposite feedstock, rather than the resin itself.

To further investigate the resulting birefringence patterns in the NC printed system, POM micrographs for composites printed with NC/Amicure are presented in Figure 3.13. It can be observed that the powdered Amicure curing agent imparts a brighter characteristic color to the printed, cured NC composites compared to the reddish-brown color imparted by the VS 03 curing agent shown in Figure 3.12, making it easier to observe spatial variations in the resulting birefringence patterns. In Figure 3.13a, a POM micrograph of a single-road printed with a tapered nozzle diameter of 609 μm is shown. It is observed that the single-road exhibits spatial variations in birefringence patterned in a core-shell color scheme. The shell region is shown to exhibit a uniform, bright color, while the core region exhibits a darker color. The color variations – due to variations in light scattering by the NC platelets in the slice – suggest that the NC platelets have adopted preferred orientation with respect to the radial location within the deposition nozzle.

Figure 3.13b presents POM micrograpes of a thin slice containing NC/Amicure cut form a longitudinal printed rectangular specimen. Similar to the slices in Figure 3.12, this slice present adjacent roads (or filaments) overlapped by a certain percentage to form a monolithic sample. Because of road overlapping, an interfacial boundary and deformed region between the roads exist. Therefore, printed roads will no longer maintain their cylindrical shape (Figure 3.13a) within the printed composite. When the slice is aligned parallel to the —

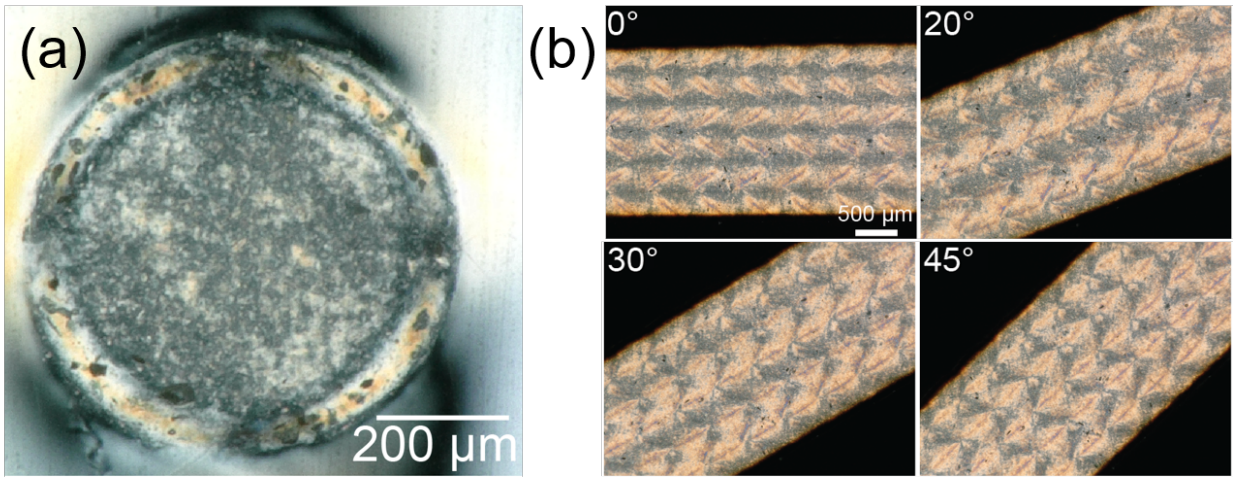

Figure 3.13: Optical microscopy images in cross-polarized light mode (transmission) of thin slices printed with NC/Amicure: (a) a slice of a single-road cut from a printed log-pile structure encased in an epoxy resin, and (b) a slice of multiple overlapped roads cut from a printed flexural bar as in Figure 4.6. The optical micrographs in (b) are taken at 0°, 20°, 30°, 45° orientation angles relative to the orientation direction of the polarizer. All specimens were printed with a nozzle diameter of 609 μm at a print speed of 20 mm/s

polarized filter (0°), visible diagonal features can be observed and they are expected to be both the left and right boundaries of each individual deformed road within the printed sample. It can also be seen that the tilt direction of the diagonal features alternate from one layer to another in a zigzagging pattern. This can be mainly attributed to the print sequence, as well as to the location of the deformed region between the overlapped roads. In this sample, roads were printed sequentially from left to right in the bottom layer, and from right to left in the second layer, and so on. By tilting the sample in cross-polarized light mode, we allow particular structural directions within the composite to be parallel to the orientation direction of the polarizer. Thus, as the printed slice is tilted from 0° to 45° (Figure 3.13b), horizontal features within the slice become brighter and visible. These features seem to indicate the top and bottom boundaries of the individual deformed roads in the sample.

Considering the lateral overlapping distance between roads (15% x D), as well as layer height (40% x D), each deformed road is expected to have a surface area smaller than π x D, where D is the nozzle diameter used for printing (609 μm). Assuming a rectangular surface area after road overlapping, each road will roughly have an area of $\sim$ 0.2 mm^2 (0.85 x 0.609 x 0.6 x 0.609). In Figure 3.13b, the diagonal and horizontal visible features have approximate characteristic dimensions of $\sim$ 410 μm and $\sim$ 475 μm, respectively. This gives an average area of 0.195 mm^2, which corresponds very closely to the measured road area programmed into the g-code used for printing the specimen.

3.4.6 NC arrangements

The nanoindentation maps in Figure 3.6 and the core-shell birefringence pattern observed in Figure 3.13a appear to be in good agreement. The resulting behavior in these maps suggest that the NC arrangements are highly influenced by the local shear stresses in the deposition nozzle. The shear rates developed during extrusion are highly non-uniform and vary significantly as a function of the radial distance within the deposition nozzle. To help understand the resulting behaviour, COMSOL analysis was carried out to simulate the flow profiles in a tapered deposition nozzle (see Figures A.3 and A.4). Distributions of the velocity magnitude and shear rates at the outlet of the deposition nozzle are shown in Figure A.4,

along with corresponding 2D plots of the velocity and shear rate as a function of the radial distance in the deposition nozzle. The velocity profile shows a flatted velocity distribution (i.e. plug-like) in the middle and a small plateau region (i.e. shear-thinning zone) near the walls of the deposition nozzle. The corresponding shear rate profile shows a maximum shear rate near the walls and zero shear rate at the center of the nozzle where the plug flow area exists. In the small shearing zone, high-aspect-ratio filler materials are expected to be highly aligned along the flow direction, while the alignment in the plug region would be more or less statistical (i.e. more random orientation).

Based on these analysis, spatial variation of NC orientation is expected across the diameter of the printed road. Therefore, the visible bright shell area of the core-shell birefringence pattern (Figure 3.13a) suggests highly ordered NC platelets near the outer boundary of the road where shear rates experienced by the flowing ink are the highest. By contrast, the darker core region indicates a more random NC orientation within the interior region of the road where the plug-flow region exists. Furthermore, this local variation in NC orientation appears to have a remarkable effect on the local mechanical properties within the printed road as quantified by the nanoindentation measurements (Figure 3.6).

To provide additional insight into the birefringence patterns associated with the printing process, in a recent study [114], we performed high-energy scanning microbeam small-angle X-ray scattering (μSAXS) with a 5 μm spatial resolution on the same NC/Amicure printed slice shown in Figure 3.13b. μSAXS was proven powerful in spatially mapping the extent of NC orientation within printed composites [114]. Figure 3.14a shows a 2D μSAXS mapping of a rectangular scanned area, showing the extent of NC orientation (i.e. Herman's orientation factor, f) in the printed slice. It is clearly shown that the μSAXS mapping allows direct visualization of the boundaries, as well as the resulting architecture of the alternating deformed roads within the printed slice (Figure 3.14a). The extent of NC orientation is shown to be higher at the road boundaries and near zero towards the middles of the road. This shows a satisfactory agreement with the COMSOL analysis (Figure A.4), nanoindentation maps (Figure 3.6), and POM observations (Figure 3.13). However, there are two important factors for the resulting orientation at the road boundaries: (1) the highest shear rates near

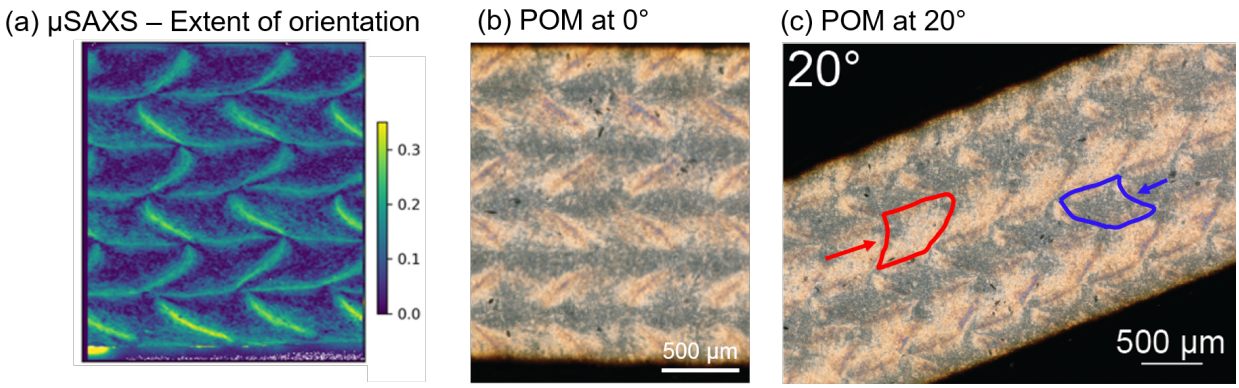

Figure 3.14: Side-by-side comparison between (a) μSAXS mapping and (b - c) POM micrographs of a 3D printed NC/Amicure slice. The μSAXS image shows the extent of orientation imposed on the NC platelets by the printing process. The μSAXS data is reproduced from [114]. The arrows in (c) indicate the print sequence and the deformed region of printed roads. Samples were printed at 20 mm/s with a nozzle diameter of 609 μm.

the walls of the nozzle during extrusion and (2) the road-to-road shearing upon deposition onto the substrate.

Figure 3.14b shows a corresponding POM micrograph of the same slice used for μSAXS mapping. It can be observed that the diagonal features in POM directly correspond to the boundaries of the roads in the μSAXS map where NC orientation is the highest. This side-by-side comparison also confirms that the horizontal features observed in POM upon rotation of the sample in the microscope (Figure 3.14c) directly correspond to the top and bottom boundaries of the deformed roads upon deposition. Additionally, from the μSAXS map (Figure 3.14a), it can be seen that the print direction (or print sequence) has a quantifiable effect on the extent of NC orientation. For instance, the road boundaries in the bottom layer in Figure 3.14a are observed to exhibit a higher degree of orientation value (up to $f = 0.35$, yellow scale), whereas the road boundaries in the subsequent layer (i.e. the second layer from the bottom) exhibit a lower degree of orientation of $f = \sim 0.2$ (greenish scale). This difference in orientation can be qualitatively observed in the POM micrograph in Figure 3.14c. At 20° of rotation, the POM micrograph displays variations in light transmittance between the alternating layers (Figure 3.14c). The layers with lower transmittance (i.e. dark color) can be seen to correspond to the roads with higher extent of orientation, while the layers with higher transmittance (i.e. bright color) correspond to the roads with lower extent of orientation (Figure 3.14c). These findings prove that POM technique, which is widely accessible, is vital to mapping the road boundaries in 3D printed birefringent specimens and providing qualitative information about the spatial variation of microstructure in 3D printed composites.

3.5 Summary and Conclusions

In this work, we have investigated the effects of a NC blend on the rheology of an epoxy resin as it pertains to formulating printable nanocomposite feedstocks for DIW 3D printing. We have also characterized relationships between NC content and the printing behavior, and between NC content and the thermo-mechanical properties of printed nanocomposites using 3-pt flexural testing, DMA, TGA, and POM. Furthermore, we have probed the local

elastic modulus property within a printed single-road via nanoindentation mapping. We have also established relationships between optical birefringence patterns, local/bulk mechanical properties, and filler arrangements within a printed component.

The strength of these 3D-printed epoxy nanocomposites ranged from 80 to 143 MPa, substantially higher than that of any previously reported values for 3D-printed thermoset nanocomposites. We anticipate higher strength values when fibers are incorporated into the matrix formulations presented here. Although anisotropy in strength and stiffness was observed in the printed nanocomposites, the layer-to-layer bonding in these materials is excellent due to the cross-linking process that occurs after the component has been printed. The thermal properties in these materials appear to be unaffected by the printing process, so that a wide range of thermal properties should be achievable by utilizing other curing agents that impart different thermal properties.

POM has proven invaluable in providing straightforward visual characterization of the structure that the printing process imposes on nanocomposite feedstock materials containing high-aspect ratio particles (e.g. NC platelets). Furthermore, this work has shown that POM is useful in providing information about road structure, mapping the road boundaries, as well as providing qualitative information about the spatial microstructural heterogeneity in 3D printed, birefringent polymer composites. As confirmed by μSAXS mapping, the POM birefringence patterns associated with the printing process strongly correlate with the spatial variation in NC arrangements within a printed component. The overall NC arrangements in printed composites are influenced by the shear alignment within the nozzle during extrusion, and road-to-road shear upon deposition onto the substrate. Furthermore, the nanoindentation results appear to provide strong correlation between the visible POM birefringence patterns and local mechanical properties.

In summary, this work has shown that epoxy nanocomposites are promising feedstock materials for direct ink writing AM, and has highlighted the need for future studies investigating the effects of fiber reinforcement in new high-strength matrices, the possibility of novel nozzle designs to influence and control material directionality, and the effects of carbon-based fillers on the structural and functional properties of printed composites. This work has also highlighted the potential use of POM in future studies investigating the effects

of the degree of road overlapping and nozzle geometry on visible birefringence patterns and filler arrangements in 3D printed composites.

3.6 Acknowledgements

This work has been generously supported by the University of Tennessee, the UT Science Alliance through the Joint Directed Research and Development Program (JDRD), and Honeywell Federal Manufacturing & Technology through contract N000230945, administered by Dr. Jamie Messman. The authors would like to thank Dr. Hilmar Koerner, Dr. Arthur R. Woll, Dr. Edward B. Trigg, and Dr. Louisa M. Smieska for the μSAXS data and analysis. The authors would also like to thank Mr. Liam Page for assistance preparing flexure test specimens and Dr. Elizabeth Barker for assistance with rheology measurements. JWK would also like to acknowledge generous support from the UT Chancellor's Fellowship.

Chapter 4

Effects of filler morphology, nozzle size and print speed on mechanical anisotropy in 3D-printed epoxy composites

A version of this chapter was originally published by Hmeidat et al.: **Hmeidat, N. S.**, Pack, R. C., Talley, S. J., Moore, R. B., and Compton, B. G. (2020). Mechanical anisotropy in polymer composites produced by material extrusion additive manufacturing. *Additive Manufacturing*, 34:101385. https://doi.org/10.1016/j.addma.2020.101385 [60].

4.1 Abstract

Extrusion-based additive manufacturing technologies, such as direct ink writing of filled polymer resins, have shown a great potential for the development of printed components with superior structural and functional properties. However, the associated extrusion process induces preferred orientation on high-aspect-ratio filler materials as they extrude through the deposition nozzle, causing strong mechanical anisotropy in printed components. Printing-induced anisotropy is a critical issue that complicates the straightforward design of additively manufactured components. The goal of this work is to gain a better understanding of the anisotropy in printed polymer composites by investigating the effects of filler morphology and print parameters on the mechanical properties of printed composites. Inks are formulated using fumed silica particles or nanoclay platelets as the primary viscosifying agent, and silicon carbide (SiC) whiskers as the primary mechanical reinforcement. Mechanical anisotropy is characterized via 3pt-flexural tests for epoxy ink formulations utilizing fumed silica or nanoclay, with or without SiC whiskers, and printed at three different print speeds, using three different nozzle sizes. Print patterns, microstructure, and filler alignment are studied using polarized optical microscopy (POM), small- and wide-angle x-ray scattering, and scanning electron microscopy (SEM). Results show that smaller nozzle diameters and higher deposition rates lead to greater anisotropy when nanoclay or SiC fillers are utilized, while the use of fumed silica alone results in mechanical behavior that is independent of print parameters and print path. Superior flexure strength values up to 215 MPa are obtained with SiC whisker-reinforced composites when tested parallel to the print direction.

4.2 Introduction

Additive manufacturing (AM) of polymer composites is a rapidly growing area, as researchers seek to improve strength, stiffness, and functionality of printed components over existing AM technologies that predominantly utilize unfilled polymers. Material extrusion AM, in particular, has been a major focus in AM of polymer composites, in part because the extrusion process is amenable to deposition of highly filled, high viscosity resins [108, 118, 102, 22, 59, 95]. In addition, extrusion processes are effective at aligning and orienting high-aspect-ratio filler materials in the direction of extrusion [10, 34, 8, 48, 82, 93, 124]. This feature enables more effective reinforcement from the filler materials [22, 31, 110, 92, 72, 14, 91, 64], and, coupled with the ability to select different print paths for each layer in a component, provides unique opportunities to design composite layups into the printed part [2]. In general, this deposition-related alignment of filler materials manifests as anisotropy in strength and stiffness relative to the print direction [22, 59, 83]. However, anisotropy in transport [72, 20, 80] and thermal [106] properties have also been reported.

To manipulate filler orientation and enable greater control over anisotropy in printed materials, new deposition techniques have been developed. For example, Raney and Compton, et al. demonstrated a rotating print head that imparts a helical fiber arrangement with spatial control over the helical angle through modulation of rotation rate [94]. Kokkinis et al. demonstrated spatial control over filler orientation in printed composites by utilizing an external magnetic field and magnetized platelet fillers [69]. Collino et al. utilized acoustic focusing within a deposition channel to concentrate, align, and arrange a wide range of fillers within printed filaments [19, 18]. Gladman et al. utilized carefully designed print paths in conjunction with a material that undergoes anisotropic swelling (as a result of filler alignment) to print actuating structures with elegantly programmed deformation modes [46]. Despite these exciting demonstrations of controlling filler orientation to achieve prescribed mechanical or functional anisotropy, there have been few basic experimental studies investigating the fundamental relationships between print parameters, filler morphology, and anisotropy in 3D-printed composite materials.

Orientation of non-spherical particles in a flowing fluid has been studied for nearly a century. For example, in Jeffrey's analysis of dilute ellipsoidal particles immersed in a viscous fluid [62], he calculated how oblate (plate-like) and prolate (rod-like) spheroids will reorient in both simple shear and extensional flows. In the limit of an infinitely thin disc or an infinitely slender rod, particles are predicted to adopt a stable orientation with their long dimension aligned in the direction of flow for either type of flow. However, particles with finite thickness are predicted to continue to rotate in simple shear flows, in what are now called Jeffrey orbitals. Conversely, for purely extensional flows even finite-sized particles are predicted to adopt stable orientation along the direction of extension [36]. The periodic motion of particles in flowing fluid has been observed experimentally in dilute and concentrated suspensions [36, 113], and very recently in numerical simulations of highly confined flows of concentrated fibers in non-Newtonian fluids wherein each particle is explicitly resolved [64]. Many authors have extended Jeffrey's analysis and applied it to the rheology of short fiber suspensions and to predict the fiber orientation in short fiber composites made via extrusion and injection molding, among others. Notably, Folgar and Tucker developed a modified model that included a fiber-fiber interaction term to enable prediction of the orientation distribution function for short fibers in concentrated suspensions [36], and Advani and Tucker introduced the use of orientation tensors to approximate the fiber orientation distribution function and enable efficient numerical calculation of the evolution of fiber orientation through various flow scenarios [1].

A significant result of these types of analyses is that fiber orientation for extrusion processes is expected to be predominantly dictated by the total amount of extensional strain that is applied to the extrudate, which is set by the draw ratio or area reduction ratio [48], the ratio of the diameter of the fluid reservoir to that of the extrusion die. Experimental studies, however, are somewhat less conclusive. For example, while Goettler identified a strong correlation between measured fiber orientation and the area reduction ratio in glass fiber-reinforced epoxy resins, he also noted a slight dependence on rate of elongational strain, which he attributed to porosity in the mixture [48, 47]. Farkash and Brandon [8] studied orientation of SiC whiskers in a ceramic slurry subject to extrusion and identified a strong correlation between fiber orientation and the length of the extrusion die (with

the diameter held constant), and they too noted a mild dependence of fiber orientation on extrusion rate [34]. Peng et al., in one of the first demonstrations of material extrusion AM of epoxy composites, observed a significant increase in the alignment of glass fibers along the print direction with an increase in draw ratio [91], which they achieved by increasing the translation speed of the print head while keeping the flow rate of the material constant. Interestingly, they did not note any difference in fiber orientation between a 1.6-mm-diameter deposition nozzle and a 0.6-mm-diameter nozzle, when flow rate and translation speed were held constant, but they did note an increase in orientation with increase in flow rate while keeping constant the translate speed of the print head. They attributed this observation to "plowing of the material surface" by the nozzle [91], reminiscent of using a doctor blade to cast a tape of material.

Observations of particle orientation as a result of tape casting processes have also led to mixed conclusions. For example, Watanabe et al. [120] studied tape casting of bismuth titanate platelets and found no correlation between platelet orientation and shear rate, but did observe an increase in platelet orientation with platelet concentration in the suspension [120]. On the other hand, Wu and Messing [125] observed strong correlation between shear rate in a tape casting process and the orientation of SiC whiskers in an acrylate-based suspension of mullite particles and SiC whiskers. Finally, Galgali et al. [42] investigated the effect of shear rate on orientation of nanoclay particles in polypropylene subject to a tape casting process and found no correlation between shear rate and particle orientation when the nanoclay had not been compatibilized with the polypropylene, but they observed greater orientation of particles with increasing shear rate for clay that had been compatibilized to the polymer matrix. Because the material extrusion AM process utilizes highly concentrated suspensions with particles that may or may not be functionalized to interact with the carrier fluid, and because the printing process includes aspects of both traditional extrusion and tape casting (Figure 4.1b), it would appear worthwhile to study particle orientation effects in AM processes in greater depth.

To that end, the overarching goal of the present work is to a gain a deeper understanding of the phenomena that govern anisotropy in polymer composites printed via material extrusion AM. To do so, we utilize filler materials with different morphologies to develop –

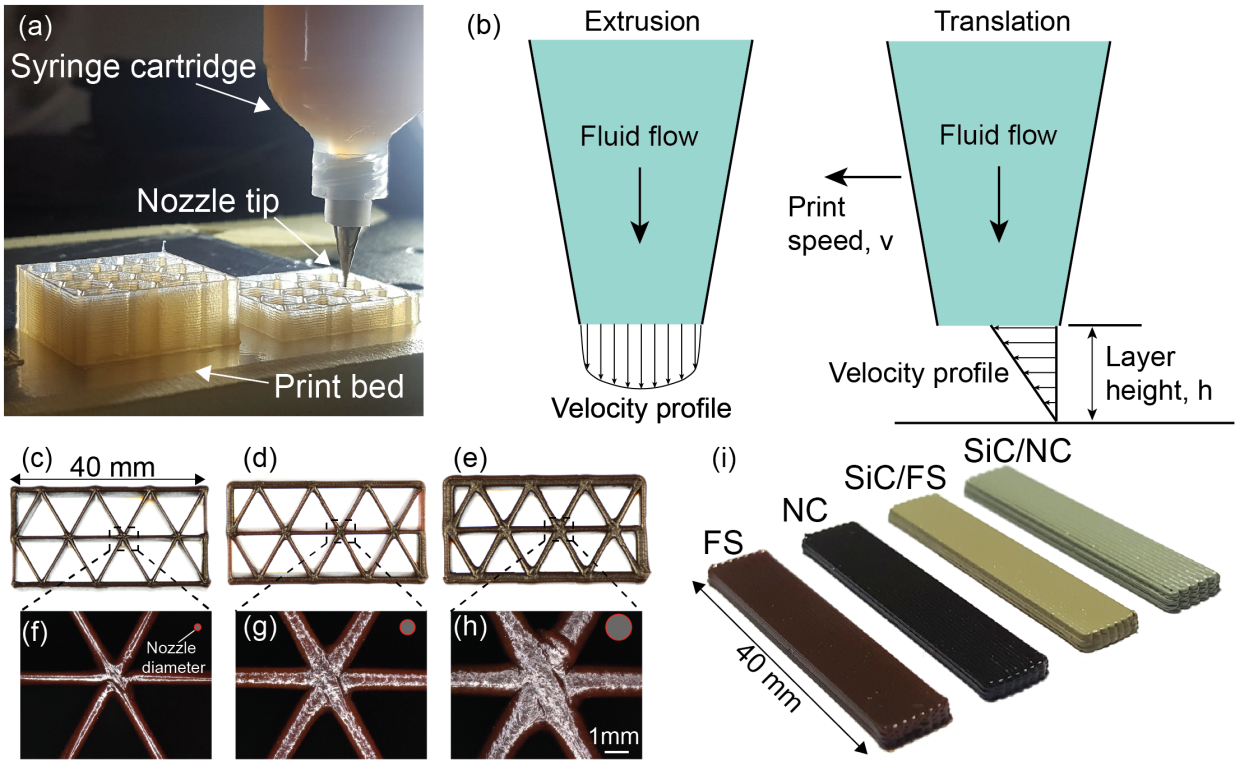

Figure 4.1: (a) Direct ink writing (DIW) process using a 410-μm-diameter nozzle (b) Cartoon depicting the approximate velocity profiles that result from extrusion and translation during printing. (c – e) Photographs of triangular honeycombs printed with nozzle sizes of (c) 233 μm, (d) 609 μm and (e) 1041 μm. (f – h) Optical micrographs showing print features as a function of nozzle diameter. (i) Rectangular mechanical test specimens composed of fumed silica (FS), nanoclay (NC), SiC/FS and SiC/NC, printed with a 609-μm-diameter nozzle. Only longitudinal specimens are shown.

viscoelastic epoxy-based inks for direct ink writing (DIW) (Figure 4.1a). Filler materials include fumed silica (FS) particles, nanoclay (NC) platelets, and silicon carbide (SiC) whiskers, and were chosen because they are frequently used to reinforce polymer resins, impart favorable printing behavior to epoxy resins, and because they span the range of morphology from oblate (NC) to spherical (FS) to prolate (SiC) (Figure 4.2). Furthermore, because mechanical anisotropy is frequently observed in material extrusion AM of unfilled polymers [3, 11], use of the FS is expected to provide a baseline measure of anisotropy that is not expected to be related to particle orientation. Using inks containing these fillers, rectangular mechanical test specimens are printed using different nozzle sizes and print speeds, and mechanical properties are measured in 3pt-flexural tests, with test specimens printed using print paths oriented along the length of the beam (longitudinal specimens) and transverse to the length of the beam (transverse specimens) (Figure A.5). Print patterns, microstructure, and filler alignment are studied using cross polarized light microscopy, small- and wide-angle x-ray scattering, and scanning electron microscopy (SEM). Through this work, we aim to elucidate the effects that nozzle size and print speed have on the strength and stiffness of printed polymer composites comprised of isotropic and anisotropic filler materials. Insights gained from this work will enable more robust design of 3D-printed composite parts.

4.3 Experimental Details

4.3.1 Materials

Epon 826 epoxy resin (Momentive Specialty Chemicals, Inc., Columbus, OH) was utilized as the DIW ink base. Basionics VS 03, 1-Ethyl-3-methylimidazolium dicyanamide (EMIM DCA) ionic liquid (Sigma-Aldrich, Inc., St. Louis, MO) was employed as a latent curing agent for the epoxy resin. Three different filler materials were utilized to impart mechanical reinforcement and favorable rheology for 3D printing: (*i*) Cab-o-sil TS-720 fumed-silica (FS) (Cabot Corporation, Alpharetta, GA), (*ii*) Garamite 7305 nanoclay (NC) platelets (BYK-Chemie GmbH, Wesel, Germany), and (*iii*) SF-1E epoxy-functionalized silicon carbide (SiC)

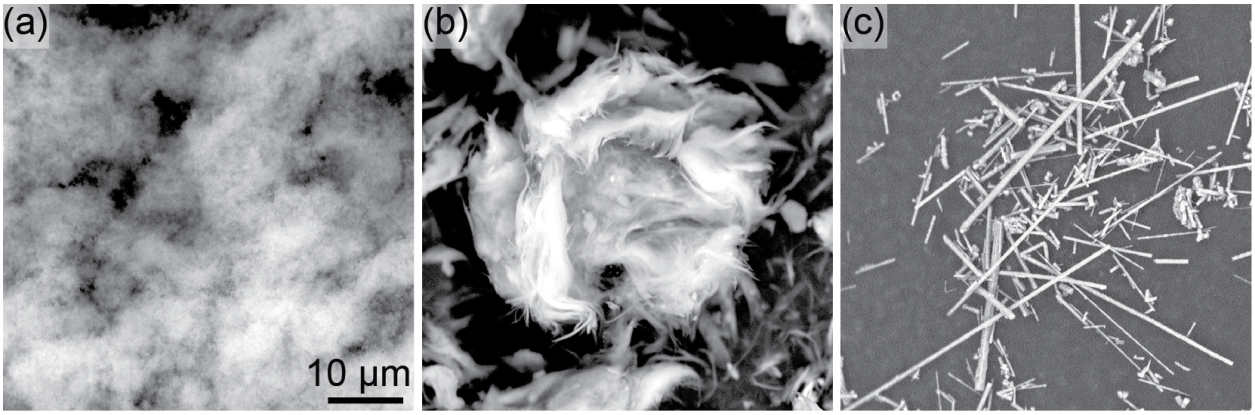

Figure 4.2: Scanning electron micrographs showing different morphologies of the as-received filler materials incorporated in this work. (a) fumed silica (FS) particles, (b) nanoclay (NC) platelets and (c) rod-like SiC-whiskers.

whiskers (Haydale Technologies Inc, Greer, SC) (Figure 4.2). The properties of ink constituents are listed in Table 4.1.

4.3.2 Formulation

All inks were mixed using a centrifugal planetary mixer (FlackTek, Inc., Landrum, SC). Ink batches were prepared using 20 g of epoxy resin and 1 g of the VS03 curing agent, mixed together at 1700 rpm for 60 seconds. Filler materials were then added in specific increments and mixed under vacuum at 0.1 atm. All ink compositions are summarized in Table 4.2. For the FS ink, the total amount of FS was added in two increments, each followed by mixing for 60 s at 1700 rpm. Finally, the sides of the mixing container were scraped using a spatula and the final mixture was mixed for another 60 s at 1800 rpm. The NC ink was prepared following the same steps as in [59]. The SiC-based inks were prepared as follows: SiC-whiskers were added and mixed at 1800 rpm for 180 s, then 1.7 g (5.07 wt.%) of NC (or FS) was added to serve as a rheology modifier, followed by mixing for 120 s at 2000 rpm. Finally, the sides of the container were scraped, and the mixture was mixed for an additional 120 s at 2000 rpm. All mixing steps were carried out under vacuum at 0.1 atm. Mixtures with single-filler material were also formulated to investigate the effects of individual filler morphology on the rheological properties of an epoxy resin (Figure A.6). It was not possible to formulate a printable ink using SiC whiskers alone.

4.3.3 Ink rheology

Rheological properties of the ink were measured using a Discovery HR-2 Rheometer (TA Instruments, New Castle, DE) with 25 mm parallel platens for all ink formulations and 40 mm parallel platens for the unfilled epoxy resin. The apparent viscosity was measured using continuous flow sweeps at controlled shear rates from 0.01 to 30 s^{-1}. The storage (G') and loss (G'') moduli were measured using an oscillatory stress sweep in stress control mode at a frequency of 1 Hz. All measurements were preceded by a conditioning step comprised of continuous shear at 0.01 s^{-1} applied for 120 seconds, followed by a rest period for 120 seconds. Measurements were conducted at ambient temperature ($\sim$21 °C). A gap of 500 μm

Table 4.1: Properties and morphology of individual ink constituents

Material	Density (g/cc	Approximate dimensions, thickness x length (μm)	Aspect ratio	Morphology
Epoxy resin	1.16	-	-	liquid
Fumed silica (FS)	2.2	0.014 x 0.014	$\sim$1	Agglomerates of spheroidal nanoparticles
Nanoclay (NC)	1.6	0.001 x 0.1	100	platelets
SiC whiskers	3.21	0.65 x 11	17	rods

Table 4.2: Composition of inks formulated for direct ink writing

Filler	Resin (g)	VS 03 (g)	Filler (wt.%)	Filler (g)	Filler (vol.%)	Density (g/cc)
FS	20	1	10	2.33	5.54	1.232
NC	20	1	10	2.33	7.46	1.237
SiC/FS	20	1	SiC (32.4), FS (5.07)	SiC (10.8), FS (1.7)	SiC (15), FS (3.48)	1.512
SiC/NC	20	1	SiC (32.4), NC (5.07)	SiC (10.8), NC (1.7)	SiC (15), NC (4.72)	1.521

was used for all formulations except SiC/NC, which used a gap of 1000 μm.

4.3.4 3D-printing and curing schedule

Test samples were printed using a 3-axis gantry (Shopbot Tools, Inc. Durham, NC) equipped with solenoid valves and air pressure regulator for extrusion. Ink formulations were loaded into 30 cc or 10 cc syringe barrels (Nordson EFD, Westlake, OH) and centrifuged at 3900 rpm for 8 minutes using a SorvallTM ST-8 Centrifuge (ThermoFisher Scientific, Waltham, MA) to get rid of any bubbles that may have been introduced during loading, following [22, 59]. Tapered metal syringe tips (S-type, GPD, Grand Junction, CO) with different inner diameters (233, 609, 864 and 1041 μm), and with the same length were used throughout the study. Tapered nozzles were used because they result in significantly higher flow-rate for a given applied pressure, compared to straight, cylindrical nozzle tips. The layer height and spacing between filaments were specified as 0.6 and 0.85 times the inner diameter of the nozzle, respectively. Rectangular specimens were printed using two different print paths: (1) the longitudinal print path, in which the printed filaments (or roads) were oriented parallel to the length of the specimen (Figure 4.1i), and (2) the transverse print path, in which printed filaments were oriented orthogonal to the length of the specimen. Schematic illustrations of the employed print paths are shown in Figure A.5. The desired print paths were defined in G-code using scripts written with Scilab software (Scilab Enterprises, Institut National de Recherche en Informatique et en Automatique, France). All specimens were printed on glass substrates covered with polytetrafluoroethylene (PTFE) coated aluminum foil (Bytac, Saint-Gobain Performance Plastics, Worcester, MA) to avoid permanent adhesion. Samples were printed at print speeds of 10, 20 and 40 mm/s and the extrusion pressure was adjusted to provide a flow-rate to match the print speed in a one to one manner. The extrusion pressure values used for each material system with different nozzle sizes and print speeds are summarized in Table A.2. Following printing, samples were pre-cured at 100 °C for 24 hours, removed from the substrate, and cured at 220 °C for 2 hours on an uncoated glass substrate. Density of printed, cured materials were measured using the Archimedes method.

4.3.5 Mechanical testing

Printed specimens with nominal dimensions of 40 x 8 x 2 mm were tested in three-point flexure configuration. Top and side surfaces of the transverse specimens were ground flat prior to testing. Tests were carried out at ambient temperature (∼21 °C) on an electromechanical load frame (Model 45, MTS Systems Corporation, Eden Prairie, MN, USA) using a 10 kN load cell with a cross-head speed of 0.8 mm/min. All printed specimens were mounted identically in the 3pt-flexural configuration, so that the principle stress direction was parallel to the print direction for the longitudinal specimens, and transverse to the print direction for the transverse specimens. A span length of 32 mm was used for all specimens. For specimens with strain-to-failure values of $\leq 5\%$, the flexural strength was calculated according to ASTM D790 [6]. For specimens with strain-to-failure values greater than 5%, the modified stress equation suggested in [44, 87] was used to calculate the flexural strength.

4.3.6 Microscopy

SEM was used to observe select fracture surfaces of tested flexure specimens and to observe the morphology of the individual filler materials prior to ink formulation. Additionally, cross-polarized light microscopy was performed on thin slices of printed specimens using transmitted light to observe birefringence patterns associated with discrete print paths, following [59]. Slices were cut using a low speed sectioning saw (TechCut 4, Allied High Tech Products, Inc. Rancho Dominguez, CA). The surfaces of the cut slices were then polished using aluminum-oxide lapping films (Allied High Tech Products, Inc. Rancho Dominguez, CA). The cut slices had comparable thicknesses (∼ 0.5 mm thick) and were inspected with the same light intensity. SEM was performed on a Phenom Desktop SEM (Nanoscience Instruments, Inc, Phoenix, AZ), and cross-polarized light microscopy was performed on a VHX-5000 digital microscope (Keyence Corporation of America, Itasca, IL), equipped with two polarized filters (i.e. polarizer and analyzer). Image analysis was performed using the open source software ImageJ, version 1.52a (http://imagej.nih.gov/ij).

4.3.7 X-ray scattering

Thin printed samples were characterized using 2D small-angle x-ray scattering (2D-SAXS) and 2D wide-angle X-ray scattering (2D-WAXS) to quantify microstructural ordering of the filler materials as a result of the printing process. SAXS was performed using a Rigaku S-Max 3000 three-pinhole SAXS system, equipped with a rotating anode emitting X-rays with a wavelength of 0.154 nm (Cu Kα). Scattering from a silver behenate standard was used to calibrate a sample-to-detector distance of 1.5 m. Two-dimensional data were collected using a fully integrated 2D multiwire area detector with 2 h exposure time. WAXS was performed using the same equipment with a sample-to-detector distance of 110.0 mm. WAXS two-dimensional diffraction patterns were obtained using an image plate, with an exposure time of 1 h. WAXS data were collected at three different locations on each specimen to obtain an average value of Herman's orientation parameter (f_x). All WAXS data were analyzed using the SAXSGUI software package to obtain WAXS intensity versus azimuthal angle profiles. For both SAXS and WAXS measurements, the X-ray beam was focused by the three-pinhole system to a size of 0.4 mm in diameter. Samples printed at 20 mm/s were used for all x-ray measurements.

4.4 Results

4.4.1 Rheological behavior and printing

Pure epoxy resin acts as a Newtonian fluid, with a nearly shear rate-independent viscosity of 10 Pa.s over the shear rate range probed (Figure 4.3a). When filler materials are added, the viscosity increases significantly and pronounced shear thinning behavior is observed. At low shear rates ($\sim 10^{-2}\ s^{-1}$), the viscosity increases in all formulations by four to five orders of magnitude. Both the FS and NC inks display similar apparent viscosities and shear thinning behavior at shear rates greater than $0.2\ s^{-1}$. The shear thinning exponent for these inks, based on a standard power law flow model, ranges from n = 0.03 to 0.25, over the range from 0.01 to 1 s^{-1}. This range indicates good shear thinning behavior and falls within the range of several other reported successful DIW inks [22, 59, 79, 38].

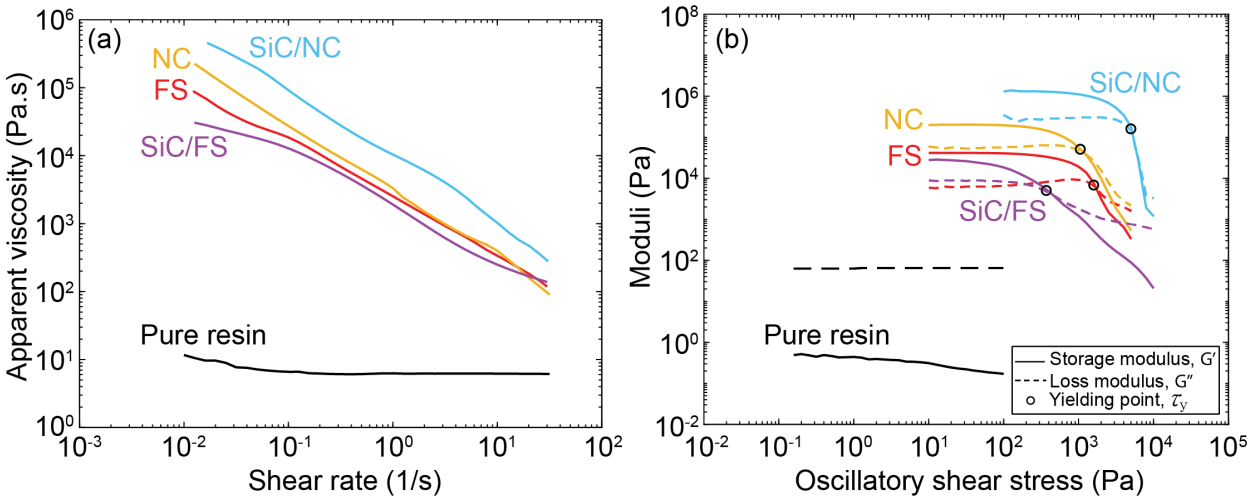

Figure 4.3: Rheological behavior of different epoxy-filled systems as it pertains to formulating printable inks for direct ink writing (DIW) process. (a) log-log plots of apparent viscosity as a function of shear rate and (b) the corresponding storage and loss moduli (i.e. viscoelastic properties) versus oscillatory shear stress for the inks shown in (a). The shear yield stress values are measured from the crossover point between the two moduli shown in (b).

Measurements of storage (G') and loss (G'') moduli are plotted in Figure 4.3b. For the pure resin, the shear loss modulus is stress-independent (∼100 Pa) and is about two orders of magnitude higher than its storage modulus, characteristic of a viscous fluid. As fillers are added to the epoxy resin, both the loss and storage moduli increase, and at low applied stress all inks display solid-like behavior, where the storage modulus is higher than the loss modulus. At higher stresses, the inks yield and flow, indicated by a steep drop in storage modulus. The yield stress approximately corresponds to the crossover point where the storage modulus drops below the loss modulus, indicating a transition from solid-like to liquid-like behavior. The SiC/NC ink exhibits the highest shear yield stress (τ_y = 5012 Pa) and the SiC/FS ink exhibits the lowest shear yield stress (τ_y = 400 Pa), while the NC and FS inks are more similar in behavior with τ_y = 1590 Pa and 1000 Pa, respectively. Although the range of storage modulus and yield stress values is fairly large, all fall within the range reported for other successful DIW inks [22, 59, 105, 121]. All of the inks were able to be printed out of three distinct nozzle sizes and at three distinct print speeds. Examples of printed specimens are shown in Figure 4.1c-i. Moreover, all of the inks were able to successfully produce pore-free, fully dense printed components with the print parameters and pressures chosen. As an example, representative optical micrographs of fracture surfaces are shown in Figure A.7 for longitudinal and transverse flexural specimens printed with the NC ink at varying nozzle sizes and print speeds. In these micrographs, there is no evidence of the original print path, indicating complete coalescence and strong adhesion between adjacent filaments and layers, as reported in [59].

4.4.2 Mechanical behavior

The flexural modulus and flexural strength of printed composites as a function of nozzle size are shown in Figure 4.4. The FS composites have a flexural modulus of 3.1 GPa and flexural strength of 109 MPa, independent of the nozzle size and print direction (Figure 4.4a, b). Printed composites containing anisotropic fillers display an inverse relationship between their flexural strength and stiffness and the nozzle size, when tested along the print direction, while a direct correlation is apparent when tested transverse to the print direction. For example, at the smallest nozzle size, the flexural strength of the NC specimens is 173 -

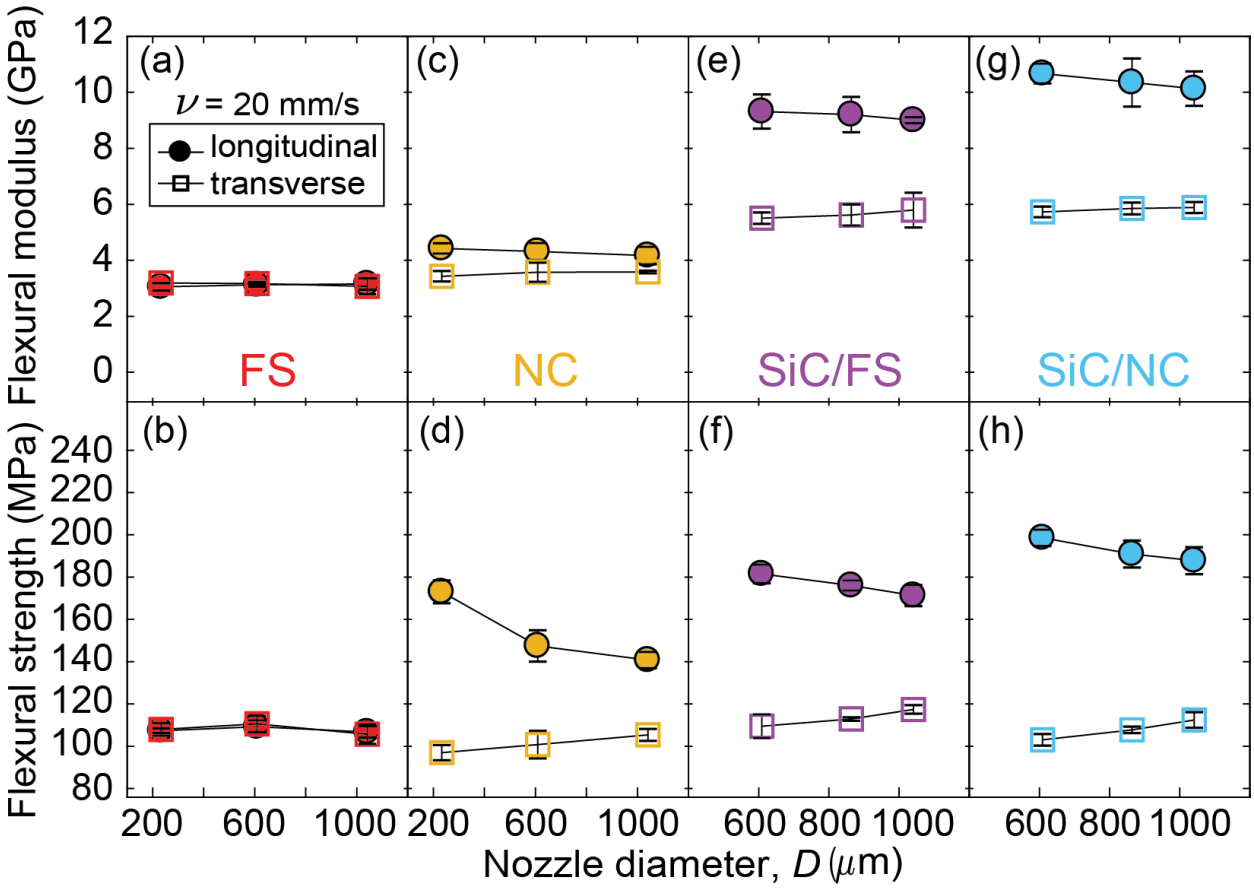

Figure 4.4: Flexural properties of longitudinal and transverse specimens as a function of nozzle diameter for epoxy-based composites containing different filler materials. Flexural modulus (top) and flexural strength (bottom) are shown, respectively, for: (a and b) FS, (c and d) NC, (e and f) SiC/FS, and (g and h) SiC/NC composites. All composites were printed at a constant print speed of 20 mm/s.

MPa along the print directions and 97 MPa transverse to it, while for the largest nozzle size, the flexural strength reduces to 141 MPa along the print directions and increases to 105 MPa transverse to it (Figure 4.4d). The same trend is observed in SiC whisker-containing inks, albeit with a greater difference in properties observed along and transverse to the print direction. At the smallest nozzle size, the SiC/NC ink displays a flexural strength of 199 MPa along the print direction and 103 MPa transverse to it. For the largest nozzle size, these values change to 188 MPa along the print direction and 112 MPa transverse to it. Trends are identical for the SiC/FS ink with strength values being slightly lower along the print direction and slightly higher transverse to it (Figure 4.4f). The trends observed for strength are also observed for flexural modulus for each material, with SiC whisker-containing inks displaying the greatest sensitivity to print direction and nozzle size (Figure 4.4c,e,g).

The flexural modulus and flexural strength of printed composites as a function of print speed are shown in Figure 4.5. Again, the FS material exhibits flexural strength and stiffness that is independent of print speed and direction (Figure 4.5a, b), whereas specimens with anisotropic filler materials display a pronounced dependence on print speed. Here, the trends are reversed from those observed for nozzle size. For example, the flexural strength of the NC material along the print direction increases with print speed from 132 MPa when printed at 10 mm/s to 159 MPa when printed at 40 mm/s. At the same time, the flexural strength transverse to the print direction decreases from 104 MPa to 96 MPa over the same print speeds (Figure 4.5d). As was observed for nozzle size effects, the presence of SiC whiskers increases anisotropy and sensitivity to print speed. At the highest print speed, the SiC/NC composite attains a strength of 216 MPa along the print direction and 93 MPa transverse to it. At the lowest print speed, the strength along the print direction reduces to 180 MPa and the transverse strength increases to 112 MPa. Again, trends are identical for the SiC/FS ink with strength values being slightly lower along the print direction and slightly higher transverse to it (Figure 4.5f). The trends observed for strength are also observed for flexural modulus for each material, with SiC whisker-containing inks displaying the greatest sensitivity to print direction and print speed (Figure 4.5c,e,g). All flexural properties are summarized in Table 4.3 and Table 4.4.

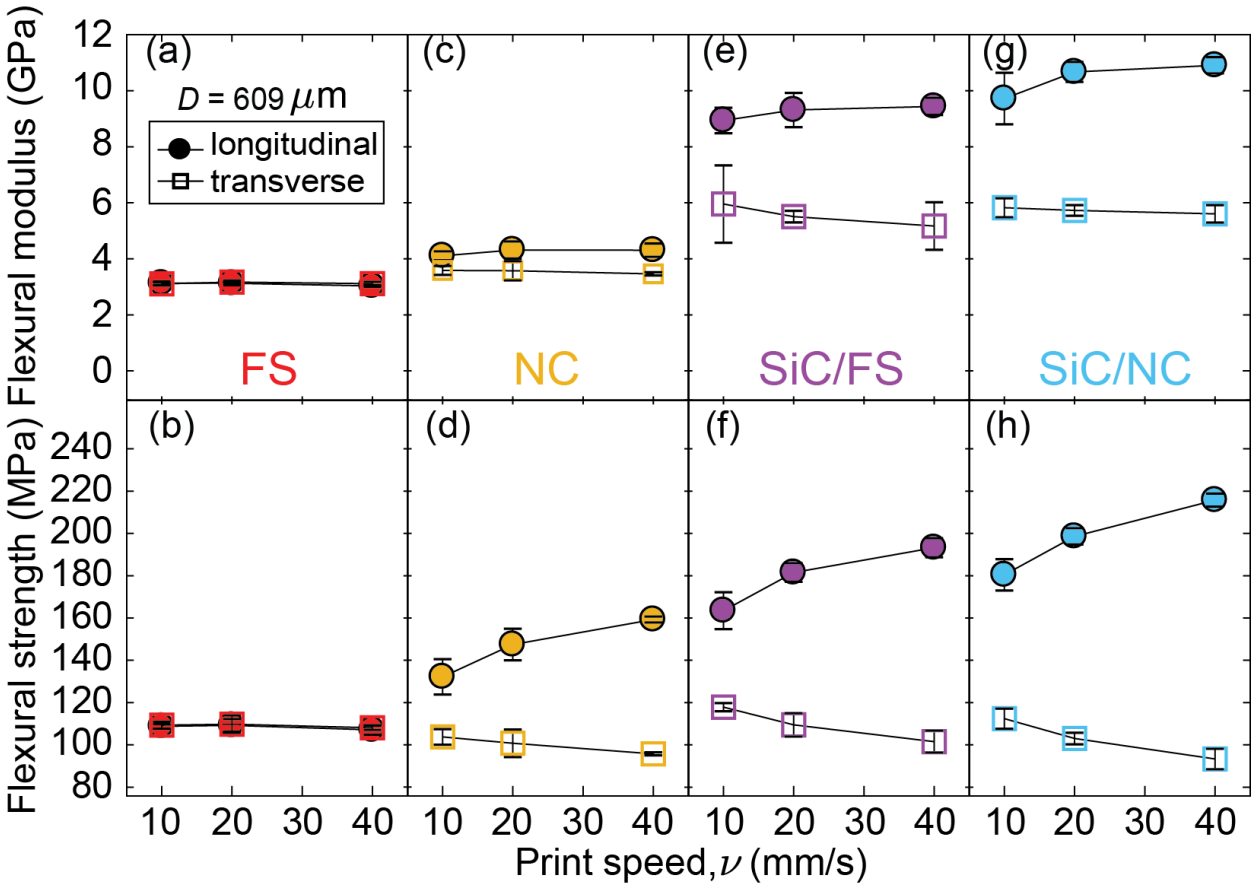

Figure 4.5: Flexural properties of longitudinal and transverse specimens as a function of print speed for epoxy-based composites containing different filler materials. Flexural modulus (top) and flexural strength (bottom) are shown, respectively, for: (a and b) FS, (c and d) NC, (e and f) SiC/FS, and (g and h) SiC/NC composites. All samples were printed at a constant deposition nozzle diameter of 609 μm.

Table 4.3: Flexural properties of FS– and NC–based 3D-printed specimens

Filler material	Nozzle size (μm)	Print speed (mm/s)	Print path*	Flexural modulus (GPa)	Flexural strength (MPa)	Strain-to-failure (%)	Number of specimens
FS	233	20	L	3.05 ± 0.13	107.3 ± 1.09	4.99 ± 0.00	4
	233	20	T	3.19 ± 0.01	107.9 ± 2.95	4.66 ± 0.30	4
	233	20	L	3.13 ± 0.07	109.2 ± 2.98	4.99 ± 0.01	6
	609	20	T	3.17 ± 0.06	110.6 ± 3.76	4.65 ± 0.29	4
	1041	20	L	3.16 ± 0.21	106.7 ± 2.68	4.98 ± 0.03	4
	1041	20	T	3.07 ± 0.28	105.6 ± 4.54	4.61 ± 0.05	4
	609	10	L	3.13 ± 0.07	108.8 ± 1.12	5.00 ± 0.00	4
	609	10	T	3.10 ± 0.06	109.3 ± 1.64	4.60 ± 0.09	4
	609	40	L	3.03 ± 0.03	107.1 ± 2.23	4.97 ± 0.12	4
	609	40	T	3.11 ± 0.07	108.1 ± 1.01	4.47 ± 0.10	4
NC	233	20	L	4.42 ± 0.18	173.0 ± 5.38	5.26 ± 0.11	4
	233	20	T	3.43 ± 0.19	97.0 ± 3.59	3.32 ± 0.26	5
	233	20	L	4.32 ± 0.30	147.4 ± 7.45	4.64 ± 0.19	5
	233	20	T	3.57 ± 0.34	100.8 ± 6.5	3.27 ± 0.14	6
	1041	20	L	4.17 ± 0.31	140.7 ± 3.85	4.45 ± 0.26	5
	1041	20	T	3.58 ± 0.05	105.4 ± 2.81	3.69 ± 0.19	4
	609	10	L	4.11 ± 0.16	132.2 ± 8.39	4.41 ± 0.52	5
	609	10	T	3.59 ± 0.16	103.8 ± 3.72	3.54 ± 0.19	4
	609	40	L	4.31 ± 0.24	159.3 ± 1.43	5.06 ± 0.08	4
	609	40	T	3.46 ± 0.06	95.7 ± 0.73	3.15 ± 0.06	4

*L: Longitudinal; *T: Transverse

Table 4.4: Flexural properties of SiC–based 3D-printed specimens

Filler material	Nozzle size (μm)	Print speed (mm/s)	Print path*	Flexural modulus (GPa)	Flexural strength (MPa)	Strain-to-failure (%)	Number of specimens
SiC/FS	609	20	L	9.31 ± 0.61	181.5 ± 4.40	3.39 ± 0.11	6
	609	20	T	5.51 ± 0.21	109.5 ± 5.55	3.03 ± 0.20	4
	864	20	L	9.20 ± 0.63	176.0 ± 2.39	3.35 ± 0.05	4
	864	20	T	5.62 ± 0.38	112.9 ± 0.80	3.17 ± 0.13	4
	1041	20	L	9.00 ± 0.11	171.3 ± 4.99	3.26 ± 0.19	5
	1041	20	T	5.79 ± 0.62	117.4 ± 1.99	3.20 ± 0.15	4
	609	10	L	8.94 ± 0.46	163.5 ± 8.71	3.33 ± 0.40	6
	609	10	T	5.96 ± 1.38	117.8 ± 1.90	3.20 ± 0.12	4
	609	40	L	9.44 ± 0.30	193.3 ± 4.51	3.42 ± 0.25	4
	609	40	T	5.17 ± 0.85	101.5 ± 5.18	2.96 ± 0.10	4
SiC/NC	609	20	L	10.67 ± 0.36	198.6 ± 3.87	2.51 ± 0.05	4
	609	20	T	5.73 ± 0.19	103.0 ± 2.75	2.15 ± 0.12	6
	864	20	L	10.35 ± 0.86	190.9 ± 6.40	2.51 ± 0.29	4
	864	20	T	5.85 ± 0.21	107.7 ± 1.54	2.17 ± 0.05	4
	1041	20	L	10.13 ± 0.61	187.8 ± 6.40	2.48 ± 0.13	5
	1041	20	T	5.89 ± 0.20	112.4 ± 3.71	2.40 ± 0.19	4
	609	10	L	9.72 ± 0.92	180.4 ± 7.40	2.40 ± 0.39	4
	609	10	T	5.82 ± 0.34	112.4 ± 4.74	2.37 ± 0.22	5
	609	40	L	10.91 ± 0.29	215.7 ± 3.13	2.84 ± 0.20	4
	609	40	T	5.61 ± 0.31	93.3 ± 4.84	2.02 ± 0.17	4

*L: Longitudinal; *T: Transverse

4.4.3 Microscopic characterization

Figure 4.6 shows representative optical micrographs for printed composites containing NC in transmitted, cross-polarized light mode. The bottom edges printed slices are aligned parallel to the orientation of the polarizer (at 0° orientation angle). It can be observed that the NC causes distinct birefringence patterns (Figure 4.6), with a clear correlation between the nozzle size and the characteristic size of the birefringence pattern. The size of the repeat patterns directly corresponds to the size of the nozzle used to print the samples, as indicated on the images by white ovals. In contrast, no birefringence or pattern was observed throughout the bulk of the printed specimens containing FS as previously reported [59], regardless of nozzle diameter (see Figure A.8).

The SiC-based specimens were not transparent enough to be inspected with cross-polarized light microscopy. However, representative SEM micrographs of fracture surfaces for flexure specimens printed with SiC/FS at varying print speeds are shown in Figure 4.7. In these micrographs the epoxy matrix is a dull gray while the SiC whiskers are bright white. The longitudinal print path was used for these specimens, so the print direction is normal to the plane of the image. At a print speed of 10 mm/s, the whiskers appear to be more randomly oriented, as a large number of whiskers can be seen lying predominantly in the plane of the image (Figure 4.7a). As print speed increases to 20 mm/s and 40 mm/s, fewer in-plane whiskers are visible, and more whiskers appear as single bright dots, corresponding to an end-on view (Figure 4.7b,c). To quantify these qualitative observations, the micrographs were converted to black and white, with white pixels indicating SiC whiskers and black pixels indicating epoxy matrix (Figure 4.7d-f). The ratio of white to black pixels provides a measure of the relative area that each phase occupies in the micrograph. For any given whisker, the apparent area is smallest when it is aligned normal to the plane of the image. Therefore, because the volume fraction of whiskers is identical in each of the samples, comparison of the ratios of white-to-black pixels provides an indication of the relative alignment of the whiskers between samples, with a lower ratio indicating greater alignment. The white-to-black ratio varies from 0.15 to 0.11 to 0.07 for print speeds of 10, 20, and 40 mm/s, respectively. We note that this approach does not result in a direct measure of whisker orientation.

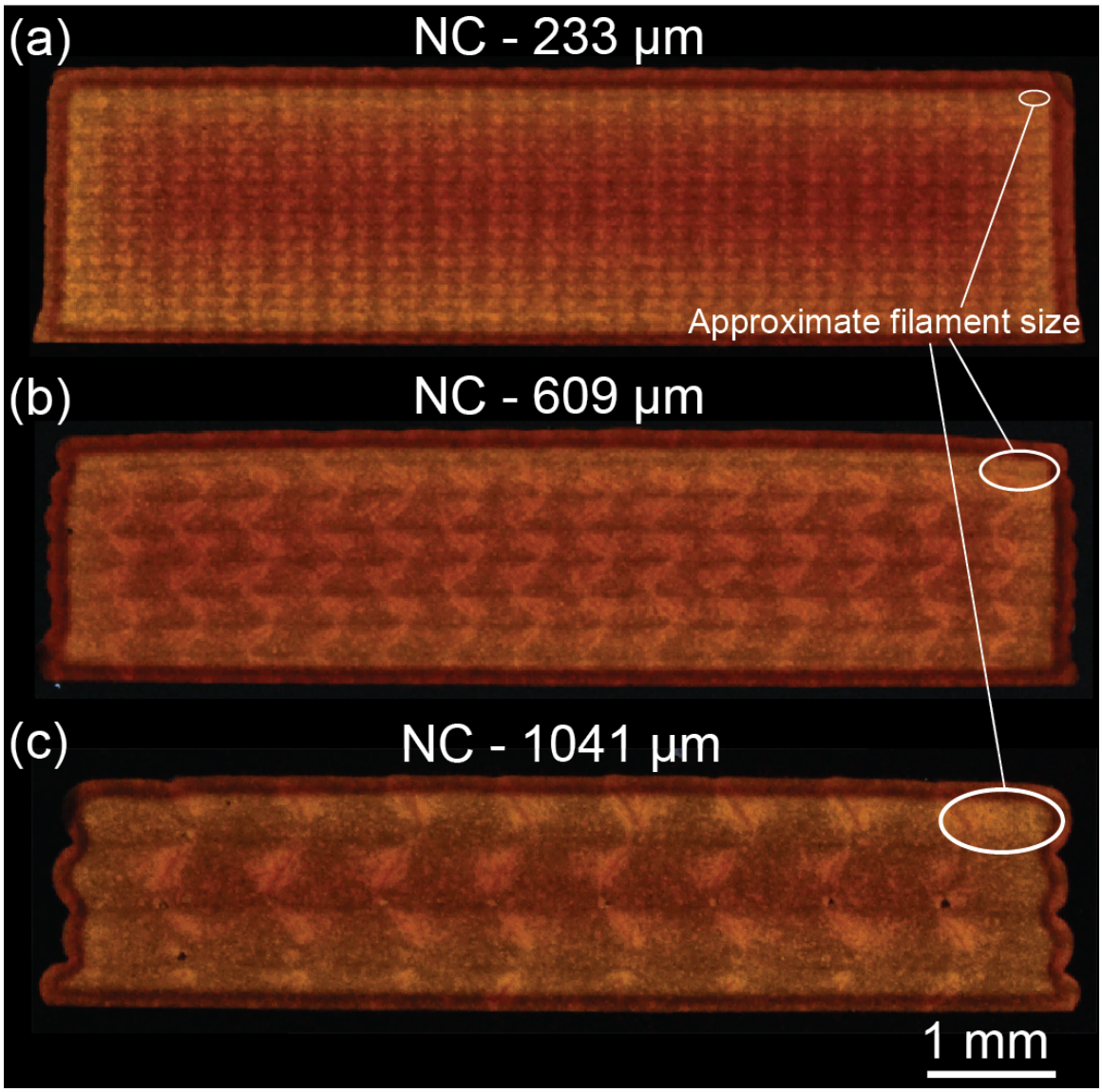

Figure 4.6: Representative optical transmitted light micrographs of polished thin slices (< 1 mm thick) cut from printed specimens containing NC filler, observed using crossed polarizers. Specimens printed with nozzle diameters of (a) 233 μm, (b) 609 μm and (c) 1041 μm. These samples show strong periodic variations in birefringence that have length scales comparable to the diameter of the nozzle used for printing. The axis of the printed filaments is normal to the plane of the image.

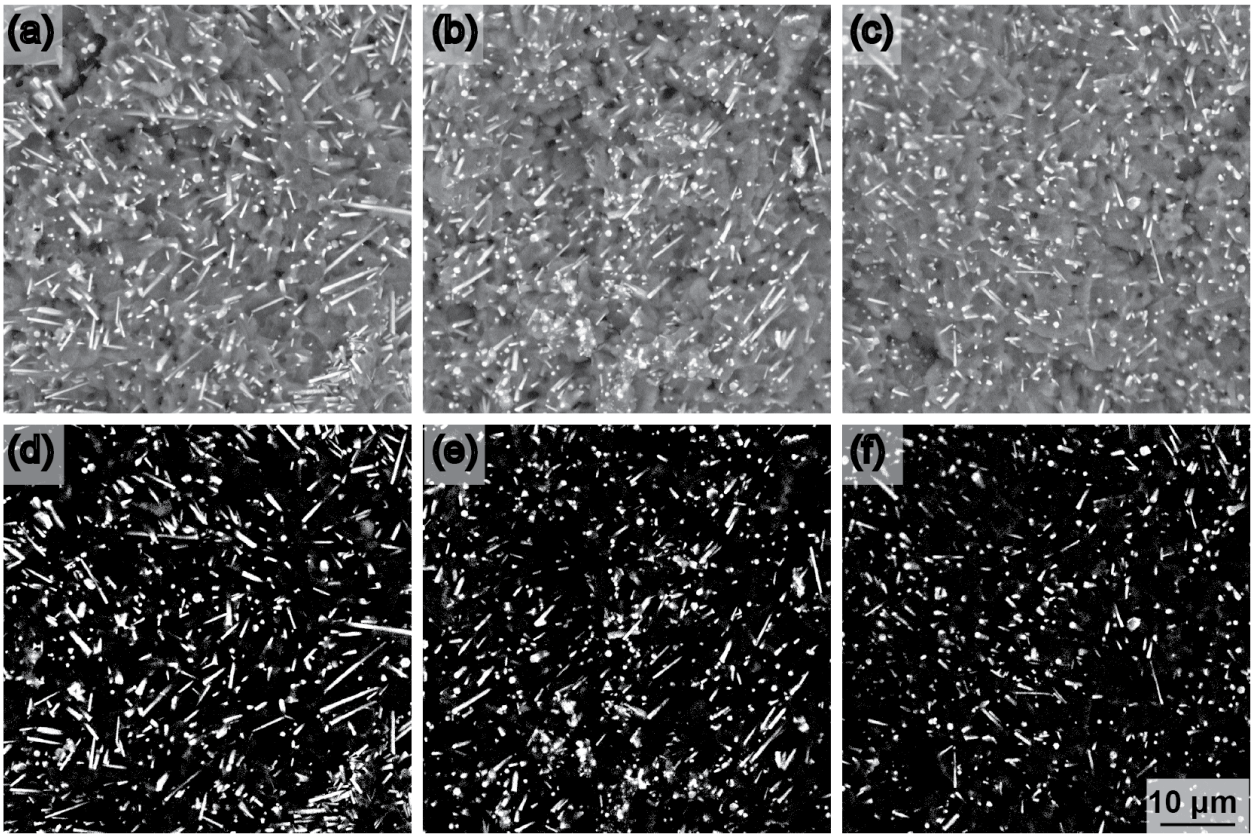

Figure 4.7: Representative SEM micrographs of selected fracture surfaces for longitudinal flexural specimens with SiC/FS ink at varying print speeds: (a) 10, (b) 20 and (c) 40 mm/s. (d – f) Binary images of corresponding SEM micrographs analyzed with ImageJ to enable quantitative correlation between print speed and whisker alignment. White pixels indicate SiC-whiskers and black pixels indicate epoxy matrix. The print direction is normal to the plane of the image, thus SiC whiskers are observed to become more oriented (indicated by fewer in-plane whiskers) in the print direction as print speed increases (from left-to-right).

4.4.4 X-ray scattering

SAXS 2D patterns of the FS material system for the three deposition nozzle diameters show symmetric, isotropic scattering (Figure 4.8a-c). In contrast, 2D scattering patterns from the NC material (Figure 4.8d-f) show anisotropic scattering along the vertical axis, indicating orientation along the horizontal axis (corresponding to the print direction) from all nozzle diameters. 2D WAXS scattering patterns were also collected for the same samples (Figure 4.9). No orientation is observed in the 2D WAXS patterns from the FS printed specimens (Figure 4.9a-c), regardless of nozzle size, whereas high intensity scattering along the vertical axis at a scattering angle of 0.51 $\mathring{A}^{-1}$ is visible in the scattering patterns from the NC specimens all nozzle diameters (Figure 4.9d-f). The sharp, anisotropic scattering observed in the scattering patterns of the NC samples occurs at a scattering angle of 0.51 $\mathring{A}^{-1}$ (7° 2θ), which is consistent with a d-spacing of 1.2 nm between the silicate platelets in the tactoids of Garamite nanoclay [51].

The degree of NC orientation was quantified using Herman's orientation factor. The two intensity maxima of background-corrected tactoid scattering intensity (0.50 $\mathring{A}^{-1}$ < q < 0.55 $\mathring{A}^{-1}$) as a function of azimuthal angle were fit using Gaussian functions. Individual Gaussian fits were then shifted horizontally along the azimuthal angle until centered about 0° (Figure A.9) and then used to determine Herman's orientation factor, f_x, using Eqs. 4.1 and 4.2:

$$f_x = 1 - 3\overline{sin^2\delta} \tag{4.1}$$

$$\overline{sin^2\delta} = \frac{\int_0^{\pi/2} I(\delta) sin^2\delta cos\delta d\delta}{\int_0^{\pi/2} I(\delta) cos\delta d\delta} \tag{4.2}$$

where δ is the azimuthal angle in radians [119]. As shown in Table 4.5, NC platelets become more oriented as nozzle size decreases. This quantitative analysis corroborates the mechanical and cross-polarized light observations for both FS and NC material systems.

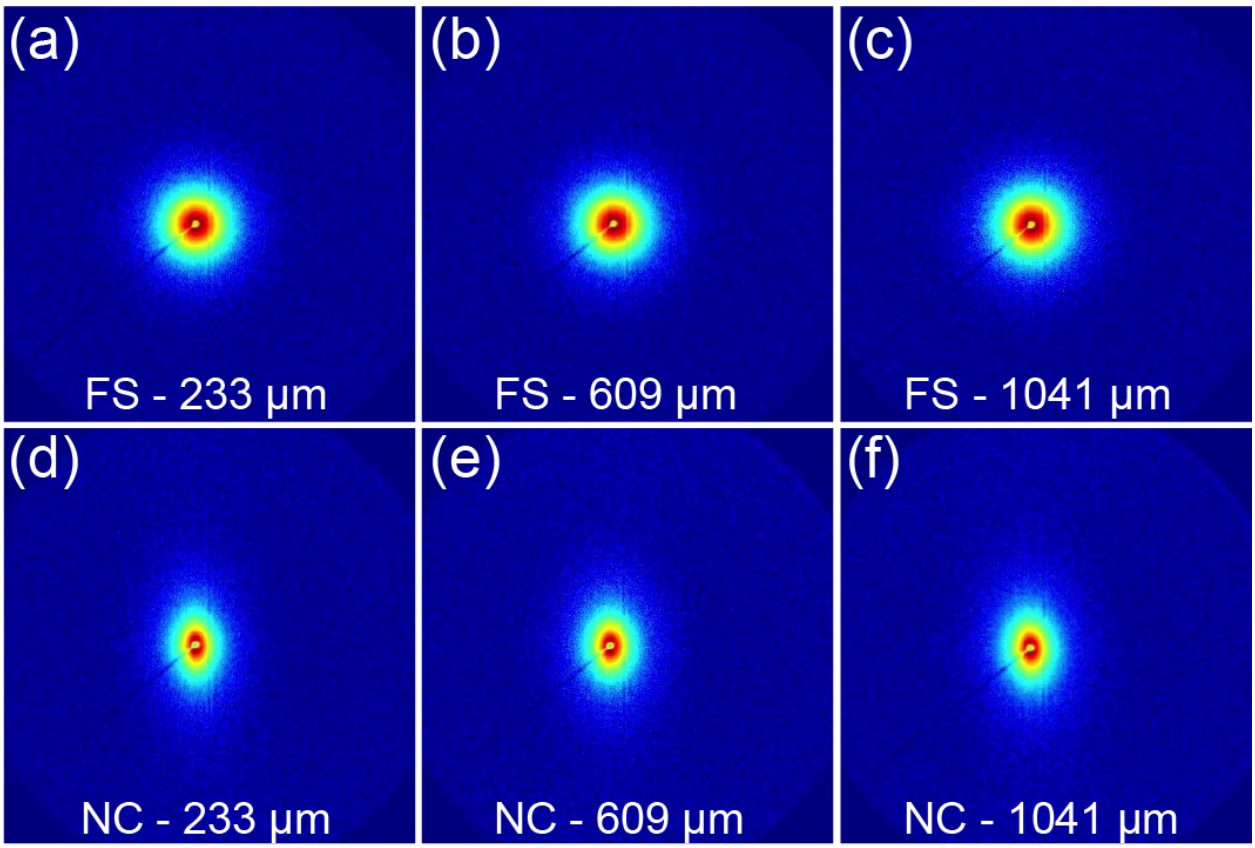

Figure 4.8: (a-c) SAXS 2D patterns for printed FS composites and (d-f) NC composites with nozzle diameters of 233 μm, 609 μm, and 1041 μm, in which the print direction is oriented along the horizontal axis.

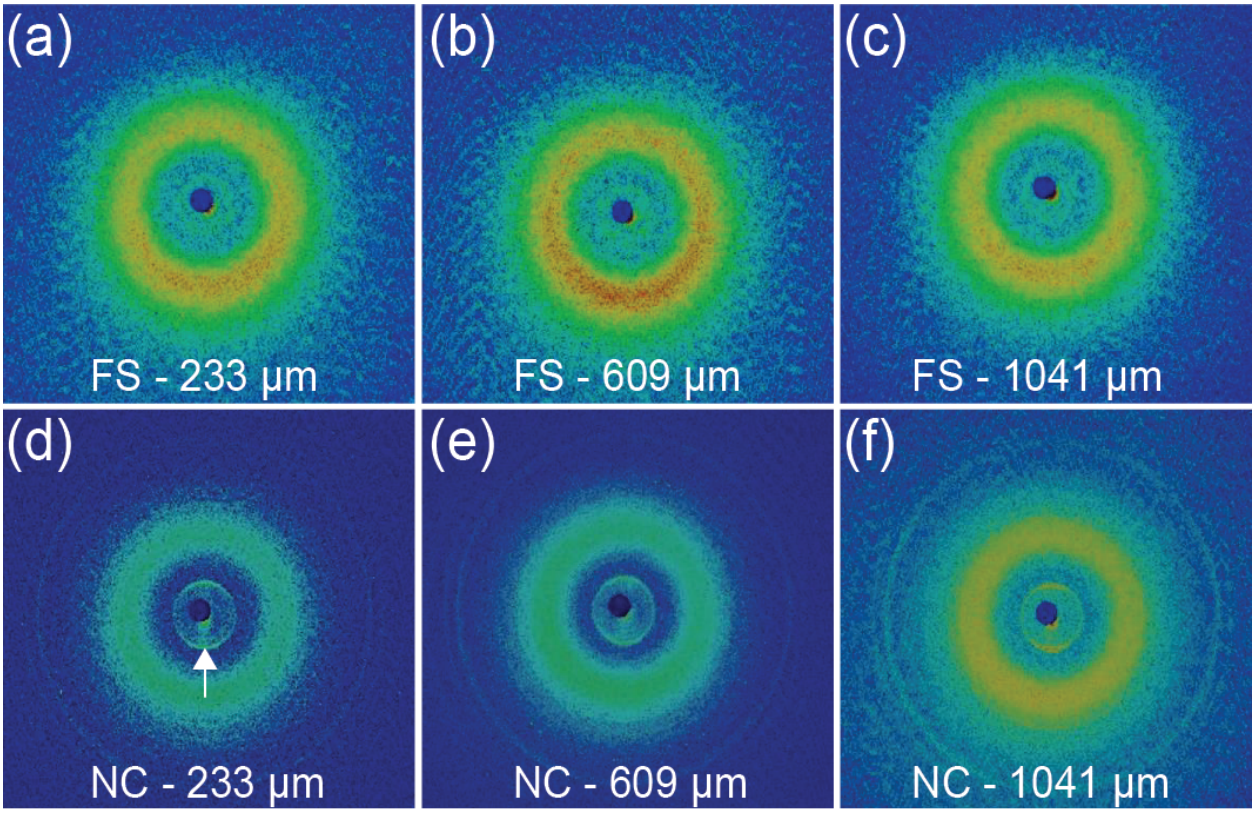

Figure 4.9: (a-c) WAXS 2D patterns for printed FS composites and (d-f) NC composites with nozzle diameters of 233 μm, 609 μm, and 1041 μm, in which the print direction is oriented along the horizontal axis. Scattering at 0.51 $\mathring{A}^{-1}$ is denoted by an arrow in (d).

Table 4.5: Herman's orientation factor, f_x, in NC-containing composites

Nozzle size (μm)	233	609	1041
f_x	0.65 $\pm$ 0.03	0.56 $\pm$ 0.04	0.51 $\pm$ 0.03

4.5 Analysis and Discussion

4.5.1 Rheology of composite inks

Although both fumed silica and nanoclay are strong rheology modifiers in the epoxy resin, and shear thinning behavior at 5 wt.% and 10 wt.% loading is similar for each material (Figure A.6 and Figure 4.3), FS and NC impart notably different storage modulus and yield stress to the epoxy resin, particularly in the presence of an additional filler material, such as SiC whiskers. For example, the FS ink possesses a higher yield stress than the NC ink, which suggests that that fumed silica may be a better viscosifier to use when formulating a composite ink. However, when combined with SiC whiskers to make the SiC/NC and SiC/FS inks, the FS results in a significantly lower yield stress and storage modulus compared to the ink that utilizes NC with SiC whiskers. This may be related to potential interactions between the FS and SiC, different length scales of the networks that FS and NC form relative to the size of SiC whiskers, or how each of the filler materials forms a network within the resin. These observations are the subject of ongoing study.

4.5.2 Anisotropy master curves

In the course of this study, we have varied nozzle size and print speed to investigate how such parameters influence anisotropy in printed composites. The results clearly indicate that particle alignment and mechanical anisotropy are influenced by both of these parameters. However, because the flow rate of the ink was matched to the translation speed of the print head, and the layer height was fixed at 60% of the nozzle diameter, changes to nozzle size were accompanied by changes to the shear rate in the fluid between the nozzle and the substrate and these tests were unable to unambiguously probe the effects of draw ratio in isolation. The presence of this shear field between the translating nozzle and the stationary substrate is a necessary feature of material extrusion AM, which would appear to preclude clean studies of draw ratio in AM processes without changing the diameter of the reservoir. With this in mind, the two data sets generated in this study can be compared by defining

a normalized translation rate that is proportional to the shear rate between the nozzle and substrate:

$$v^* \equiv \frac{v}{D} \propto \frac{v}{h} \tag{4.3}$$

where ν is the print speed and D is the diameter of the deposition nozzle, and h is the layer height. The physical interpretation of this quantity is unambiguous, regardless of the properties of the fluid or the specific geometry of the nozzle and it enables direct comparisons between different combinations of nozzle size and translation rate.

In addition, we define an anisotropy factor as the ratio of the longitudinal to transverse property of printed composites:

$$\psi \equiv \frac{M_L}{M_T} \tag{4.4}$$

where ψ is the anisotropy factor, M is either the strength or modulus, and the subscripts L and T indicate the longitudinal and transverse properties, respectively. Using these definitions, all of the mechanical test data for a given material system collapse onto one curve that indicates a single functional relationship between normalized translation rate and mechanical anisotropy (Figure 4.10). Plotted in this manner, we see that the anisotropy factor approaches a value of unity as the normalized translation rate approaches zero, indicating that the printed composites approach isotropic behavior as the print speed approaches zero or as the nozzle size approaches $+\infty$.

Based on this observation, a two-parameter power-law model is proposed to fit the data:

$$\psi = 1 + A(\nu^*)^b \tag{4.5}$$

where A and b are the fitting parameters. Table 4.6 lists the values of A and b computed for each material system, for both modulus and strength data, computed using non-linear regression. Model predictions are also plotted with the data points in Figure 4.10.

These master curves and power law model allow one to make direct comparisons of a wide range of printing tests to provide insight into the phenomena that govern anisotropy in printed composite materials. We anticipate that every combination of filler material and

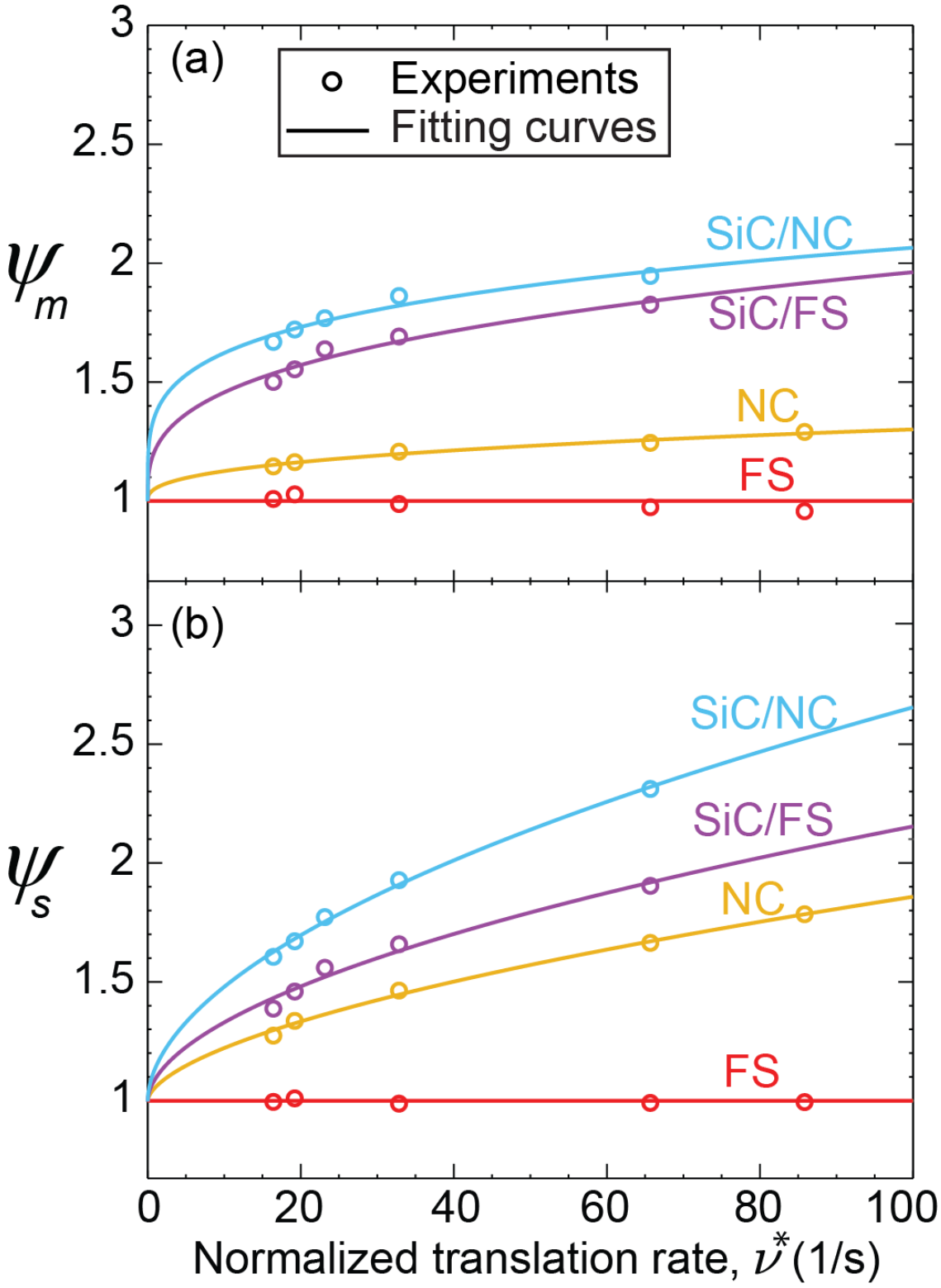

Figure 4.10: Plots of mechanical anisotropy versus normalized translation rat in (a) modulus and (b) strength for all the samples tested. Solid lines are the fit of the power-law model given in Eq. 4.5.

Table 4.6: Fitting parameters for power law anisotropy model

	Fitting parameters			
	Modulus		Strength	
Filler material	A	b	A	b
FS	0	1	0	1
NC	0.05	0.38	0.06	0.60
SiC/FS	0.22	0.32	0.10	0.54
SiC/NC	0.36	0.23	0.14	0.54

resin will have a characteristic master anisotropy curve that depends on the viscosity of the resin, the size and morphology of the filler material, and the geometry of the deposition nozzle. Thus, for a given printing system and material, a select few mechanical tests can enable predictions of mechanical properties and anisotropy over a broad range of printing parameters. This can be very important for enabling more rigorous engineering design of 3D-printed composite materials and may even provide a pathway to spatially program mechanical properties using only print parameters. It is important to note that the upper limit of the anisotropy factor is dictated by the properties that would result from perfectly aligned fillers, above which the anisotropy factor would adopt a constant value. This limiting behavior is not captured in the model at present.

4.5.3 Interaction between fillers

Experimental observations showed that the FS-based composite exhibits mechanical behavior that is independent of both print direction and normalized translation rate. Therefore, the increase in mechanical properties that is observed in the SiC/FS ink with increasing normalized translation rate is assumed to result entirely from the reinforcing effect of the SiC whiskers as they become more oriented along the print direction. However, when considering the SiC/NC system, both the SiC whiskers and the NC are expected to contribute to the dependence of the mechanical properties on the normalized translation rate. Indeed, each filler material individually displays strong sensitivity to deposition rate. If both species of filler behave independently in the epoxy matrix, then a synergistic effect may be expected. That is, if the epoxy and clay are thought of together as the matrix, and the SiC whiskers as the reinforcing species, then an increase in normalized translation rate would result in strengthening of the matrix alone – from increased alignment of the clay particles, leading to higher composite strength – and strengthening of the composite through increased alignment of the SiC whiskers. If that description is accurate, then one would expect to see significantly different behavior between the SiC/FS and SiC/NC inks.

Interestingly, while the SiC/NC composite is stiffer and stronger along the print direction than the SiC/FS composite, the difference is small compared to the difference in strength between the NC- and FS-only composites at comparable print parameters. To highlight this

observation, we have plotted the difference in strength between the NC and FS composites, and between the SiC/NC and SiC/FS composites as a function of normalized translation rate in Figure 4.11. Along the print direction, the NC composite is 20-30 MPa stronger than the FS composite at low normalized translation rate, and 60-70 MPa stronger at high normalized translation rate. Conversely, the SiC/NC composite is only 10-20 MPa stronger than the SiC/FS composite across the entire range of normalized translation rates investigated. One possible explanation for this observation is that the presence of SiC whiskers frustrates the orientation of the clay platelets during the deposition process by altering the local shear rate and stress state in the vicinity of the whiskers, thereby diminishing the propensity of the smaller clay platelets to align along the print direction. This phenomenon could have important implications for the design of optimal composite feedstocks for material extrusion AM, and further study is warranted.

4.6 Summary and Conclusions

In this work we have investigated the effects of filler morphology, nozzle size, and print speed on the mechanical anisotropy in 3D printed epoxy composites fabricated via DIW. We have also characterized the effects of different filler materials on the rheology of an epoxy resin to formulate printable composite inks for DIW. The key results of this work can be summarized as follows:

- Printed epoxy/FS composites were shown to exhibit mechanical behavior that is independent of nozzle size, print speed, and print path, with flexural strength and modulus of 107 MPa and 3.1 GPa, respectively.
- SiC whisker-reinforced printed composites display flexural strength values up to 215 MPa along the print direction. To the authors' knowledge, this is currently the highest reported flexural strength for a 3D-printed whisker-reinforced polymer composite.
- X-ray scattering measurements confirmed the alignment and dependence on print parameters of nanoclay platelets in printed composites.

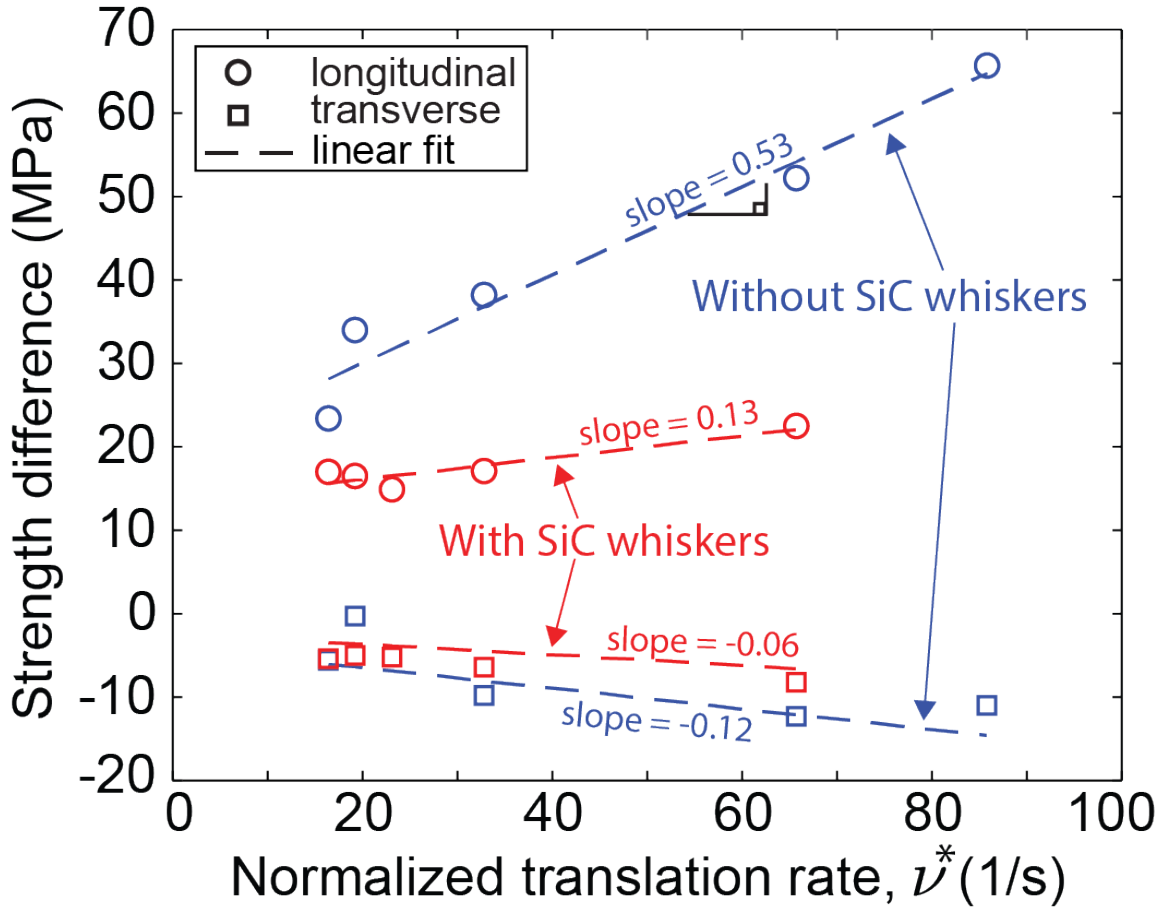

Figure 4.11: The difference in strength between the NC and FS composites (blue), and between the SiC/NC and SiC/FS (red) composites as a function of normalized translation rate. Dashed lines represent the linear regression of each data set. Plotted in this manner, the data suggest that NC is less influenced by normalized translation rate in the presence of SiC whiskers.

- The mechanical properties of printed composites containing high-aspect-ratio fillers display pronounced dependence on both nozzle size and print speed. For the resin and filler combinations utilized in this study, we have found that a power law describes the relationship between mechanical anisotropy and normalized translation rate.

- Both nanoclay and fumed silica are highly effective at imparting shear thinning and yield stress behavior to epoxy resin, but nanoclay appears to be more effective for formulating inks with multiple filler materials. However, in the printed composites, the presence of larger filler materials may disrupt the alignment of clay platelets during the deposition process.

Anisotropy in printed components is a critical issue that complicates the straightforward design of AM components. We believe this study represents an important step towards enabling the application of rigorous engineering design principles to AM component design. In addition, the study highlights the possibility of additively manufacturing complex components with programmed anisotropy simply through the systematic variation of print parameters and ink constituents.

4.7 Acknowledgments

This research was supported through funding from NSF under grant no. CMMI-1825815, and Honeywell Federal Manufacturing and Technologies through Contract DE-NA0002839, administrated by Dr. Jamie Messman, Mr. Steven Patterson, and Dr. Eric Eastwood. The authors would also like to thank Prof. Michael Kilbey for helpful discussion and Mr. James W. Kemp for assistance with SEM imaging. BGC and RCP would like to acknowledge partial support from the Tennessee Higher Education Commission Center for Materials Processing. SJT acknowledges financial support from Doctoral Scholars program of the Virginia Tech Institute for Critical Technology and Applied Science (ICTAS). SiC whiskers were generously provided by Mr. Kevin Fox at Haydale Technologies, Inc.

Chapter 5

Processing and mechanical characterization of carbon fiber – reinforced epoxy composites for material extrusion additive manufacturing

An original version of this chapter has been submitted by Hmeidat et al. for publication in *Composites Part B: Engineering*: **Hmeidat, N. S.**, Elkins, S. D., Peter, H, Kumar, V., and Compton, B. G. (2021). Processing and mechanical characterization of carbon fiber-reinforced epoxy composites for material extrusion additive manufacturing (Submitted).

5.1 Abstract

Fiber-reinforced polymer composites have been extensively utilized in recent years as feedstock materials for extrusion-based additive manufacturing (AM) processes to improve strength, stiffness, and functionality of printed parts over unfilled printed polymers. However, the widespread adoption of AM of fiber-reinforced polymer composites requires a deeper understanding of the process-structure-property relationships in printed components, and such relationships are not well understood yet. This work uses short carbon fiber-reinforced epoxy composites as ink feedstocks for the direct ink writing (DIW) AM technology and seeks to better understand the evolution of fiber length distribution (FLD) during ink processing. FLD is measured for a wide range of ink compositions and shear mixing times, and the distributions are fit with a Weibull-type distribution function. The effects of FLD on the tradeoff between ink processability, ink rheology, printing behavior and mechanical properties are also investigated. Furthermore, the effects of printing parameters (nozzle size and print speed) on mechanical anisotropy and fiber orientation distribution (FOD) in printed composites are explored. Mechanical properties of printed composites are characterized via 3pt-flexural testing, and microstructure is investigated using optical and scanning electron microscopy (SEM), and x-ray computed tomography. Finally, the fitted Weibull parameters are fed into a composite model that incorporates FLD and FOD, and model predictions are found to be in excellent agreement with experimental observations.

5.2 Introduction

Material extrusion additive manufacturing (AM) of polymer composites has been the focus of research interest in recent years for its unprecedented ability to create new structural

components and multi-material architectures [69, 38, 18, 80, 97, 75]. Extrusion-based AM methods consist of building components in a layer-by-layer format by selectively depositing material through a deposition nozzle [107]. Building components in this manner allows direct manufacture of complex structures that may not be feasible via traditional manufacturing approaches. Despite this unique flexibility, key challenges remain that hamper the widespread adoption of AM to produce robust, end-use structural components. Key challenges include: (*i*) the lack of feedstock materials with high specific properties and functionality that can compete with current engineering materials, (*ii*) the associated printing-induced anisotropy and trapped porosity in printed parts, and (*iii*) the lack of deep understanding of the process-structure-property relationships in additively manufactured parts.

A wide variety of polymer feedstock composites have been developed for material extrusion AM technologies – including fused filament fabrication (FFF) and direct ink writing (DIW) – utilizing different filler reinforcements into both thermoplastic and thermoset resins. For example, polymer feedstocks reinforced with carbon fibers (CFs) [31, 76, 110, 116, 22, 83, 94, 92, 88], glass fibers [133], silicon carbide microfibers [18, 22, 60, 49], nanoclay [60, 122, 59, 63, 114], graphene [20, 54] and carbon and boron nitride nanotubes [104, 24] have been investigated to improve strength and stiffness in printed materials. Short fiber-reinforced polymer composites are of particular interest due to their combination of mechanical properties, low density, increased thermal stability, high processibility and low production cost [39, 41]. Love et al. showed that the incorporation of CFs (up to 13 vol%) into a thermoplastic ABS resin could drastically diminish warping in printed parts by reducing the coefficient of thermal expansion (CTE) of the neat ABS resin by 88.72% along the deposition direction [76]. The work also showed that printed ABS/CF composites exhibited higher tensile strength (∼194% increase), stiffness (∼335% increase), and thermal conductivity (∼124.3% increase) than neat ABS when tested parallel to the deposition direction. Zhong et al. incorporated glass fibers (up to 18 wt%) into an ABS resin, leading to an increase of 140% in the tensile strength along the print direction; however, the presence of glass fibers was found to reduce the flexibility and robustness of the ABS filaments during handling [133]. Tekinalp et al. showed that short CFs align in the print direction during

printing ABS/CF composites (up to 40 wt% CF), improving the strength by ∼115% and the stiffness by ∼700% along the print direction over neat ABS [110]. Although highly oriented CFs were achieved in printed ABS/CF composites, increased porosity caused lower tensile properties than those of their compression-molded counterparts [110]. It was also found that the average fiber length in printed ABS/CF composites decreased with increasing CF content, as a result of fiber breakage during compounding the CF and ABS resin under high-shear mixing [110]. Ning et al. investigated the effect of fiber length on the mechanical properties of ABS/CF composites printed via FFF at a CF loading of 5 wt% [86]. Their results showed that printed composites with fiber lengths of 150 μm achieved higher tensile strength and modulus than printed composites with fiber lengths of 100 μm [86].

Several fiber-reinforced thermoset inks have been developed for DIW. For example, Calvert et al. were the first to use DIW for printing CF-reinforced epoxy composites in 1997 [14]. In that study, varying fractions of chopped CF with varying fiber lengths were utilized in epoxy resins in the presence of fumed silica (FS) to induce thixotropy. The modulus and strength of printed composites showed dependence on both fiber length and CF content, and fiber orientation was shown to follow the direction of printing [14]. In a subsequent study by Peng et al., flexural bars of epoxy/FS/glass-fibers were printed with varying print-head speeds and print paths (i.e. orientation angles) relative to the length of the bar [91]. Their results showed that the degree of fiber orientation increases with increasing print-head speed while keeping the flow rate constant. As a result of increased fiber alignment, the flexural modulus improved by 50% as the print-head speed increased by a factor of 2.5 [91]. More recently, Compton and Lewis showed that highly loaded epoxy/nanoclay/SiC/CF inks can reach Young's modulus values up to 24.5 GPa in the print direction [22], while Malek et al. achieved an elastic modulus up to 57 GPa in the print direction using pitch-based CFs in epoxy/nanoclay inks [77]. Nawafleh and Celik employed a vibration-assisted printhead to enable printing epoxy/NC/CF inks with a high CF content (up to 46 vol%), achieving flexural strength values up to 400 MPa and stiffness up to 53 GPa in the print direction [83]. Hmeidat et al. incorporated 15 vol% of SiC microfibers into an epoxy resin filled with either nanoclay (NC) or FS, achieving flexure strength values up to 215 MPa along the print direction [60]. In that study, the team also demonstrated that SiC microfibers become more

highly aligned along the print direction when smaller deposition nozzles and higher print speeds are employed.

Although most of the prior studies have shown significant advances in printed fiber-reinforced polymer composites with high mechanical properties, less attention has been given to the effect of formulation and processing parameters on the fiber length evolution in printed composites. The mechanical performance of short fiber composites is highly dependent on fiber content, fiber length distribution (FLD), fiber orientation distribution (FOD), and fiber-matrix interfacial adhesion [110, 39, 41]. Material extrusion AM is beneficial in this regard as it induces orientation of fibers as they are extruded through the deposition nozzle [110, 22, 92, 60, 14, 91, 64, 72] (Figure 5.1a). However, during formulating and printing of fiber feedstocks, fiber attrition can occur, affecting the rheological properties of the ink and the mechanical properties of printed composites [22, 39, 41]. To enable a better understanding of the mechanical behavior of printed short fiber composites, the linkage between fiber content, formulation processes, printing parameters, the resulting FLD and FOD, and mechanical properties of printed composites need to be established. Pierson et al. have investigated the effect of mixing time and fiber content (up to 5.5 vol%) on the FLD in epoxy/NC/CF inks for DIW [92]. Their results suggest that mean fiber length approaches a steady-state value above a certain mixing time for composite inks containing greater than 2.3 vol% carbon fibers. However, the team did not directly investigate how the mixing time and FLD affect rheological and mechanical properties.

This work seeks to better understand of the evolution of fiber length during material processing, including how the FLD affects the tradeoff between processability (rheology and printing behavior, print quality), and mechanical properties (Figure 5.1b). FLD are measured for a wide range of ink compositions and mixing times, and the distributions are fit with a Weibull-type distribution function. The fitted Weibull parameters are fed into a composite model developed by Fu and Lauke [39] that incorporates FLD and FOD, and model predictions are found to be in excellent agreement with experimental observations. In addition, the effect of nozzle size and print speed on mechanical anisotropy and fiber orientation in printed composites is investigated. Mechanical properties of printed composites are investigated via 3pt-flexural testing, and microstructure is investigated using

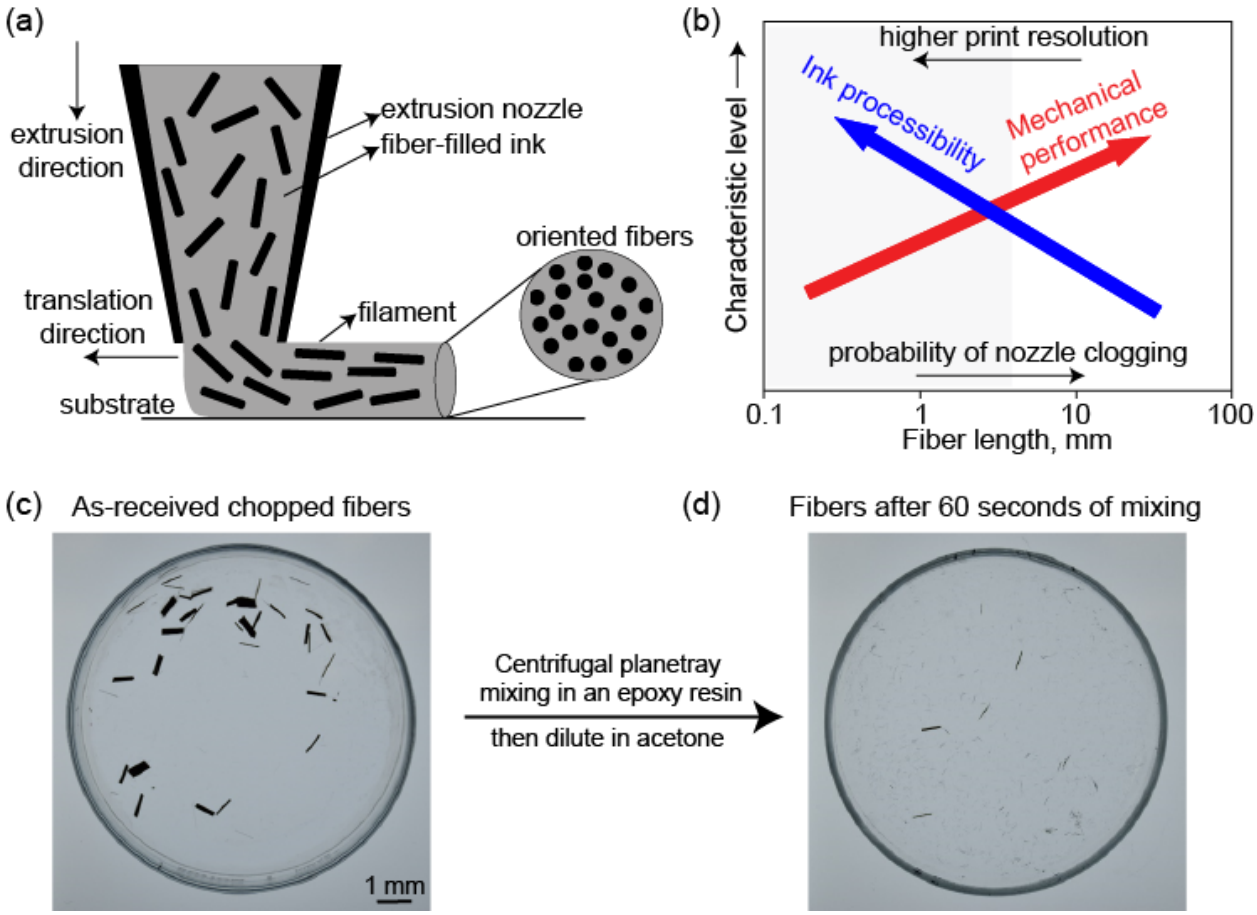

Figure 5.1: Schematic illustrations of (a) direct ink writing (DIW) process, and (b) effect of fiber length on ink processability and mechanical performance in fiber-reinforced composites. The shaded area demonstrates a typical range of fiber lengths in short carbon-fiber composites, which exhibits an excellent combination of material processability and mechanical behavior. (c) and (d) show carbon fibers before and after mixing.

optical and scanning electron microscopy (SEM), and x-ray computed tomography (xCT). Results and insights gained from this work will enable the design of better composite feedstocks for material extrusion AM and more rigorous engineering design of printed composite components.

5.3 Experimental

5.3.1 Materials

EPON 826 (Momentive Specialty Chemicals, Inc., Columbus, OH) epoxy resin with a density of 1.162 g/cm^3, was utilized as the composite ink base. Dicyanex 1400B (Evonik Industries AG, Essen, Germany), a dicyandiamide (DICY) powder, was employed as the latent curing agent for the epoxy resin. Kaltex K20-HTU chopped carbon fibers (CFs) from the Oak Ridge National Laboratory (ORNL) Carbon Fiber Technology Facility (CFTF) were used for this study [32]. These fibers are low-cost, PAN-derived fibers, sized for epoxy resin and chopped to 6 mm length with a density of 1.773 g/cm^3 (Figure 5.1c and Figure A.10). Garamite-7305 nanoclay (NC) (BYK-Chemie GmbH, Wesel, Germany), with a density of 1.6 g/cm^3, was used to modify the viscosity of the resin and enhance the printing behavior. More information about the NC filler material can be found in [59].

5.3.2 Ink formulation

Inks were formulated using a centrifugal planetary mixer (FlackTeck, Inc., Landrun, SC) in 90-ml. plastic containers (FlackTeck, Inc., Landrun, SC). All batches were prepared using 20 g of epoxy resin. The fibers were added to the epoxy resin in different amounts, 3.1, 6.2, 9.15 and 12.2 vol%. After the addition of fibers, the inks were mixed for four different durations, 180, 360, 540, and 720 seconds, to observe the effects that the mixing process and fiber content have on the fiber length distribution. This resulted in a total of 16 different mixtures. Mixing was conducted under vacuum at 0.1 atm at a constant speed of 1800 rpm for all inks. Because high shear mixing can generate heat, the mixing time was divided into 180 s intervals to allow the mixer and ink to cool down. The cool-down period was ∼10

minutes per interval. These ink formulations do not contain NC and will be referred to as the CF inks (Table 5.1).

To identify any effects that the presence of the NC viscosity modifier has on fiber length evolution, an additional ink containing 9.15 vol% CF and 5 wt% (1.3 g) NC was formulated and mixed at the same aforementioned mixing times. The mixing was done in two steps to enable better dispersion of the fibers in the presence of NC. First, the CF was added and mixed for half of the targeted mixing period at 1800 rpm. Then, the NC was added and mixed at 1800 rpm. These formulations will be referred to as the CF/NC inks. After several trials, 5 wt% NC was identified as a suitable amount to modify ink viscosity and enable printing of self-supporting parts following [60]. Inks utilized for fiber length measurements did not contain any curing agent, but 1g of DICY (corresponding to 5 parts per hundred by weight resin) was added into inks utilized for printing. In these inks, DICY was added to the epoxy resin before the fillers and was mixed under 0.1 atm for 60 s at a speed of 1500 rpm.

5.3.3 Fiber length measurements

Fiber length measurements were taken for both CF and CF/NC inks. To reliably measure the variations in fiber lengths, the fibers must be separated from the epoxy matrix without altering length. Further, the fibers must all be aligned in a single plane. To do this, a stainless steel spatula was used to pull a small sample of material from the inks after each mixing cycle. The material was then placed in a bath of acetone to dissolve the epoxy. Then the specimen was immediately poured into a glass petri dish so the acetone could evaporate. This process resulted in fibers that were oriented in single plane (Figure 5.1d and Figure A.11). After the evaporation of acetone, the distributed fibers were imaged using a VHX-5000 digital microscope (KEYENCE Corporation, Itasca, IL), and the fiber lengths were measured manually. To develop greater confidence in the measurements, multiple images were stitched together to enable a larger number of full-length fibers to be measured. For the CF/NC inks, the acetone bath alone was insufficient to effectively separate the fibers from the epoxy/NC matrix. With the addition of NC, the fibers tend to form clumps of material, making it challenging to measure fiber lengths in the microscope.

Table 5.1: Compositions of epoxy/CF ink formulations

Resin (g)	CF (g)	CF (wt%)	CF (vol%)
20	1.00	4.76	3.10
20	2.00	9.13	6.20
20	3.10	13.3	9.15*
20	4.24	17.5	12.1

*an additional ink was formulated at this CF loading in the presence of 5 wt% NC filler.

To solve this issue, the acetone bath was placed in a beaker inside an ultrasonic bath (Fisher Scientific, Waltham, MA) and sonicated for 3 minutes to force clumps of fibers to separate. Subsequently, the acetone bath was poured again into a petri dish, and then immediately placed on a CIMAREC stirring hot plate (ThermoFisher Scientific, Waltham, MA) in a fume hood to expedite evaporation of the acetone. Then fiber length measurements were taken as described previously for the CF inks. The sample size of length measurements for each ink formulation is summarized in Table 5.2. It should be noted that all fiber length measurements were taken immediately after ink mixing; therefore, any potential fiber breakage due to loading the ink into the printer cartridge or during extrusion are not accounted for in the reported FLDs.

5.3.4 Ink rheology

Rheological properties were measured for the pure epoxy resin, epoxy/NC matrix and CF/NC inks, using a Discovery HR-2 Rheometer (TA Instruments, New Castle, DE) with 40 mm parallel platens for the pure resin and 25 mm parallel platens for all inks. To probe the effect of mixing time on ink rheology, inks with different mixing times were investigated. A gap size of 0.5 mm was used for both the pure epoxy resin and epoxy/NC inks, and a gap of 1.5 mm for the CF/NC inks. The apparent viscosity profiles were measured using continuous flow sweeps at controlled shear rates. The viscoelastic properties were measured using an oscillatory stress sweep at controlled oscillatory stresses with a frequency of 1 Hz. All measurements were preceded by a 120 s conditioning step at a constant shear rate of 0.01/s, followed by an equilibration period for 120 s. All tests were conducted at the ambient temperature of the lab ($\sim$ 21 °C).

5.3.5 3D printing

Inks were loaded into 10 cm^3 syringe barrels (Nordson EFD, Westlake, OH) using a spatula. Loaded syringes were then centrifuged at 3900 rpm for 10 minutes using a SorvallTM ST-8 Centrifuge (ThermoFisher Scientific, Waltham, MA), to get rid of any air bubbles that may have been introduced during ink loading, following [22, 59, 60]. The loaded syringe was then

Table 5.2: Volume averaged fiber length and Weibull distribution parameters for all inks formulated

CF content (vol%)	Mixing time (seconds)	Sample size	Shape parameter, k	Scale parameter, λ (x10^{-6})	Volume averaged fiber length (mm)
3.10	180	419	1.852	664	0.587
	360	558	1.891	599	0.529
	540	240	1.901	576	0.526
	720	277	1.916	436	0.414
6.20	180	737	2.24	532	0.499
	360	808	2.18	441	0.389
	540	539	2.20	403	0.364
	720	362	2.30	316	0.287
9.15	180	1079	2.27	439	0.408
	360	709	2.27	361	0.317
	540	427	2.23	333	0.297
	720	288	2.30	296	0.268
12.1	180	973	2.25	466	0.455
	360	845	2.31	334	0.296
	540	183	2.10	279	0.248
	720	499	2.37	262	0.242
9.15 + 5 wt% NC	180	521	2.128	477	0.637
	360	520	2.564	374	0.344
	540	511	2.587	335	0.317
	720	511	2.583	302	0.280

mounted on a custom 3-axis positioning stage (Shopbot Tools, Inc., Durham, NC) equipped with a pneumatic extrusion system for printing. The inks were printed onto substrates covered with polytetrafluoroethylene (PTFE)-coated aluminum foil (Bytac, Saint-Gobain Performance Plastics, Worcester, MA), to prevent permanent adhesion. Rectangular specimens were printed using tapered metal luer-lock nozzle tips (S-type, GPD, Grand Junction, CO) with three different inner diameters of 609, 864 and 1041 μm, and three translation print speeds of 10, 20 and 40 mm/s. The layer height and spacing between filaments were set as 0.6 and 0.8 times the inner diameter of the nozzle used, respectively. The extrusion pressure was adjusted manually to produce a flow-rate matched to the translation print speed (Table A.3).

Two print paths were employed to print mechanical test specimens, in which printed filaments (or roads) are either oriented parallel (hereafter referred to as longitudinal specimens) or orthogonal (hereafter referred to transverse specimens) to the length of the specimen (see Figure A.5). The g-codes were generated using custom programs written with Scilab software (Scilab Enterprises, Institut National de Recherche en Informatique et en Automatique, France). Following the printing process, all specimens were cured at 120 °C for at 24 hours, followed by 2 hours at 220 °C. The density of the printed, cured specimens was measured using a Mettler Toledo Xs64 balance (Mettler-Toledo, LLC, Columbus, OH) equipped with an Archimedes density kit in distilled water.

5.3.6 Mechanical characterization

Flexural tests were performed at room temperature on an electromechanical load frame (Model 45, MTS Systems Corporation, Eden Prairie, MN, USA), using a load cell with a capacity of 1 kN. Flexural test specimens with nominal dimensions of 40 mm x 8 mm x 2 mm were tested in three-point flexure, using a span length of 32 mm and a crosshead speed of 0.8 mm/min. Edges and surfaces of the printed specimens were ground smooth prior to testing. Mechanical testing was performed according to ASTM D790 [7].

5.3.7 Microscopy

Optical micrographs were recorded using a VHX-5000 digital microscope (Keyence Corporation of America, Itasca, IL), to observe features of as-printed specimens, fiber lengths and fracture surfaces. Additionally, scanning electron microscopy (SEM) was carried out on a Phenom Desktop microscope (Nanoscience Instruments, Inc, Phoenix, AZ), to observe the morphology of the as-received carbon fibers, as well as select fracture surfaces of tested CF/NC flexural specimens. All observed specimens were sputter-coated with gold prior to SEM imaging.

5.3.8 X-ray computed tomography

xCT scans were conducted on 3D printed CF/NC composites using a ZEISS Xradia Versa 520 xCT equipment. Two specimens were measured, one using the highest print speed and one using the lowest print speed, and were taken from flexural test specimens. The xCT data were collected at 3 W power and 40 kV accelerating voltage. Tomographs of the middle section of the tested composites (a cylinder with 2 mm diameter and 2 mm height) were recorded. For each tomogram, 1 μm resolution was maintained to capture the individual CFs. A 4x scintillator objective attached with a Charged Coupled Device (CCD) camera was used to record the scans. The recorded scans were visualized using the image processing software Avizo (version 9.3.0, XFiber module, ThermoFisher Scientific), and the Xfiber extension was used to quantify the FODs. The Xfiber extension provides tools to trace the centerlines of cylindrical features.

A detailed workflow of the analysis is given in [128]. Using an assumed minimum fiber length and fiber radius, the analysis enables the construction of a fiber orientation tensor representing the local distribution of the fibers. A spherical coordinate system was used to describe the fiber orientation, with theta (θ) representing the offset angle between the fiber axis and the Z-axis (which is the printing direction in the present work). θ varies in the range of 0° - 90°, and fibers are considered aligned to the print direction when θ approaches 0°.

5.4 Results and Discussion

5.4.1 Fiber length evolution in CF inks

The effects of CF content and mixing time on the fiber length distribution (FLD) during ink processing are illustrated in Figure 5.2. Figure 5.2a shows normalized FLDs for inks with different CF contents mixed for one mixing time (540s), while Figure 5.2b shows normalized FLDs for inks with constant CF content (9.15 vol%) mixed for different times. In both cases, the mixing process results in asymmetrical FLDs. The length of the fibers ranges up to 2 mm. The most probable fiber length decreases with increasing CF content and with increasing mixing time, as indicated by a peak shift and narrower distributions with increasing mixing time or fiber content. Fiber breakage may occur as a result of the interactions between fibers during the high-shear mixing process, interactions between fibers and the resin, and interaction between the fibers and surfaces of the mixing container. Increasing fiber content and mixing time increases the number of fiber interactions, leading to increased fiber breakage and shorter fibers in the resulting ink formulation.

A two-parameter Weibull distribution function can be employed to model the evolution of fiber length during mixing [39, 17, 109, 115]. The cumulative distribution function (CDF) can be given as [39]:

$$CDF \;=\; 1 \;-\; exp\left[-\left(\frac{L}{\lambda}\right)^{k}\right] \tag{5.1}$$

where L is the fiber length, λ and k are the scale and shape parameters of the Weibull distribution, respectively.

Figure 5.3a and b show the experimental CDFs (dotted lines) of the corresponding FLDs in Figure 5.2a and b, respectively, along with the Weibull fitted CDF curves (solid lines). The CDF curves shift upward and to the left (i.e. towards shorter fiber lengths) with increasing fiber content and increasing mixing time, without considerably changing the nature of the curves. The Weibull parameters are computed from the experimental CDF curves by linear regression on a double log-log plot, as illustrated in Figure 5.3c for the ink containing 9.15 vol% CF.

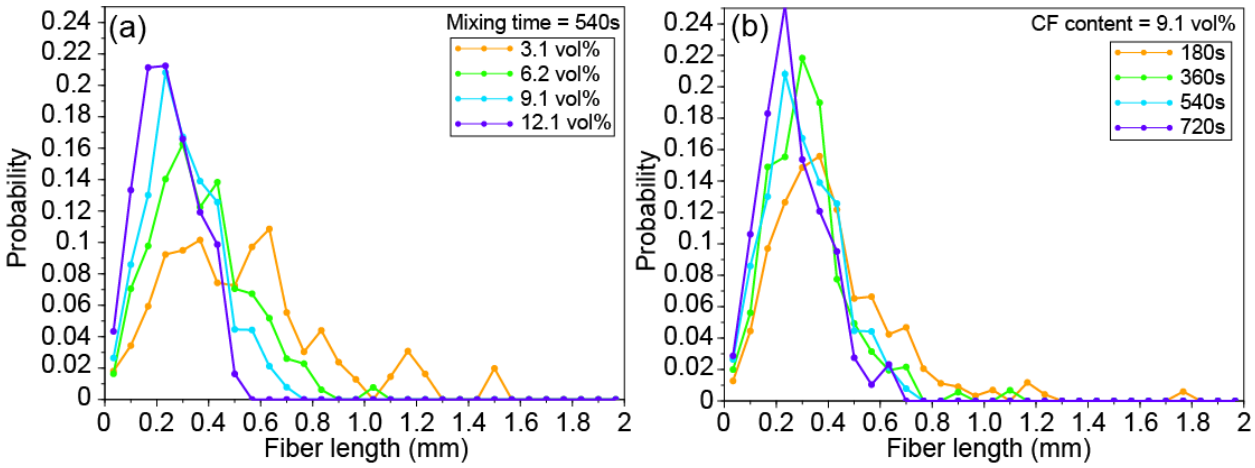

Figure 5.2: Fiber length evolution during processing of CF inks: (a) FLDs for inks with different CF contents mixed for one mixing time (540s) and (b) FLDs for inks with constant CF content (9.15 vol%) mixed for different times

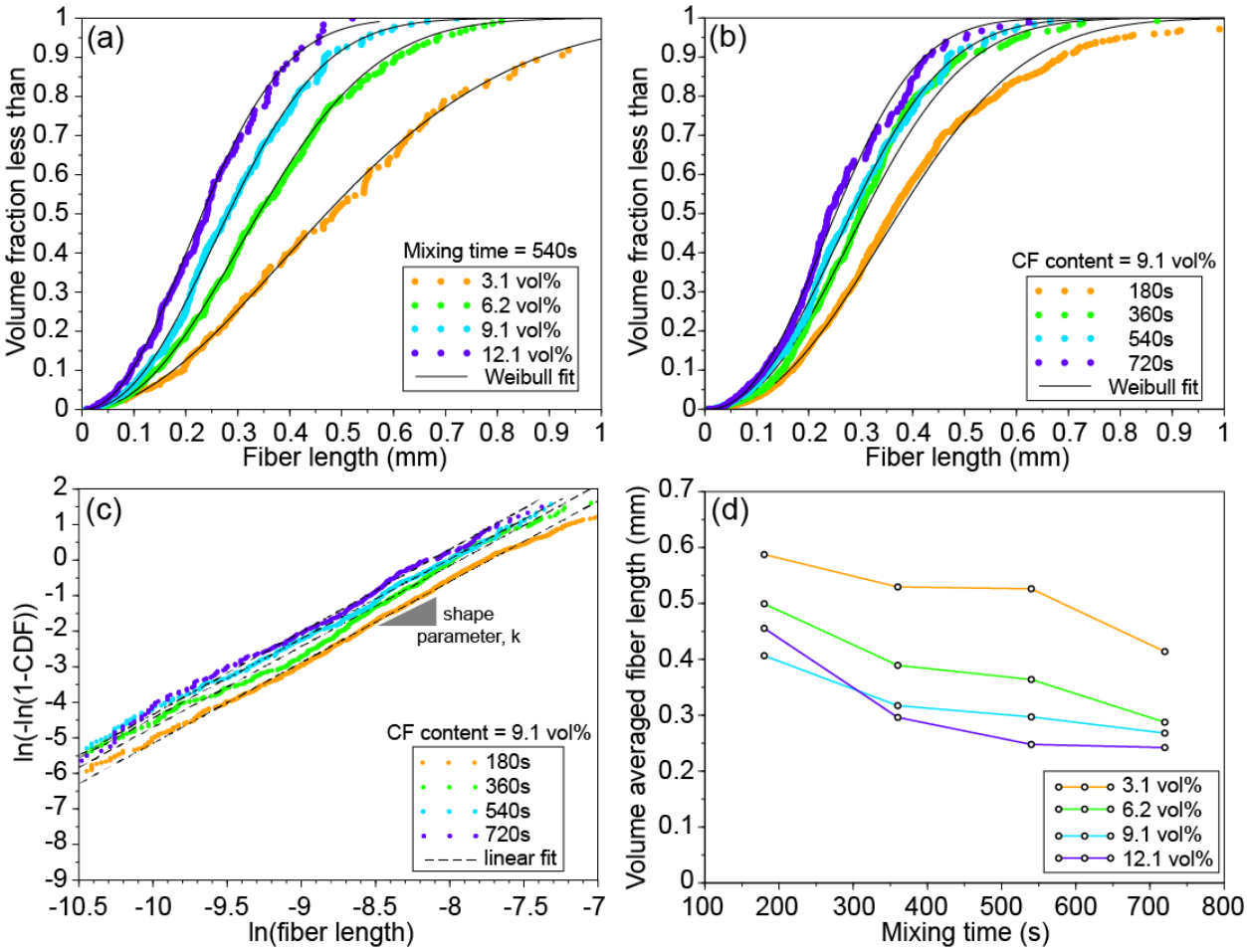

Figure 5.3: (a - b) CDFs of the corresponding FLDs shown in Fig. 1a and b, respectively, along with fitted Weibull distributions (solid lines). (c) Weibull fit parameters computation (Eq. 5.1) for inks with constant CF content of 9.15 vol% mixed for different times, along with dashed lines representing the linear regression of each dataset. (d) A summary of volume average fiber length values in all CF inks for different mixing times and CF contents.

Comparing the Weibull-fitted CDF curves with the experimental CDF data reveals a reasonably good fit across all parameter sets. Interestingly, all length data sets have a similar shape parameter, k, which ranges from ∼2 to ∼2.3, while the scale parameter, λ, decreases systematically with increasing CF content and mixing time. The computed Weibull parameters for all inks tested are summarized in Table 5.2.

The measured volume average fiber lengths for all sample sets are plotted in Figure 5.3d. The initial fiber length (6 mm) was reduced to an average fiber length value below 0.6 mm across all CF contents and mixing times probed. This behavior indicates that high-aspect-ratio carbon fibers fracture easily during the shear mixing process, even at low CF contents and low mixing times. The volume average fiber length appears to reach a steady state value of ∼0.27 mm for high fiber content and long mixing time, in broad agreement with the mean fiber lengths reported by Pierson et al. [92]. All volume average fiber length values for all CF inks tested are summarized in Table 5.2.

5.4.2 Fiber length evolution in CF/NC inks

The incorporation of NC results in higher viscosity of the carrier resin, which is expected to influence the FLD. Figure 5.4a presents the FLD of the CF/NC ink containing 9.15 vol% CF at different mixing times. Changing the rheology of the carrier resin by adding NC leads to noticeable differences in FLD compared with the CF inks, particularly at low mixing times. At a mixing time of 180 s, a poor Weibull fit is obtained (Figure 5.4b) as compared to the same mixing time without NC (Figure 5.3b). However, as mixing time increases with NC, the FLD adopts a more Weibull-like distribution.

FLDs in the presence of NC are plotted in Figure 5.4c on double log-log axes to enable fitting of Weibull parameters to the data. Poor fit in the lower region of the plot indicates that the presence of NC reduces the number of very short fibers, whereas the poor fit in the upper region indicates a higher number of long fibers. A comparison of the average fiber lengths as a function of mixing time for the 9.15 vol% CF inks with and without NC is shown in Figure 5.4d. The results show that, after a sufficient mixing time, the effect of NC diminishes, and average fiber lengths converge. The computed Weibull parameters, as well as the average fiber length values for all the CF/NC inks are summarized in Table 5.2.

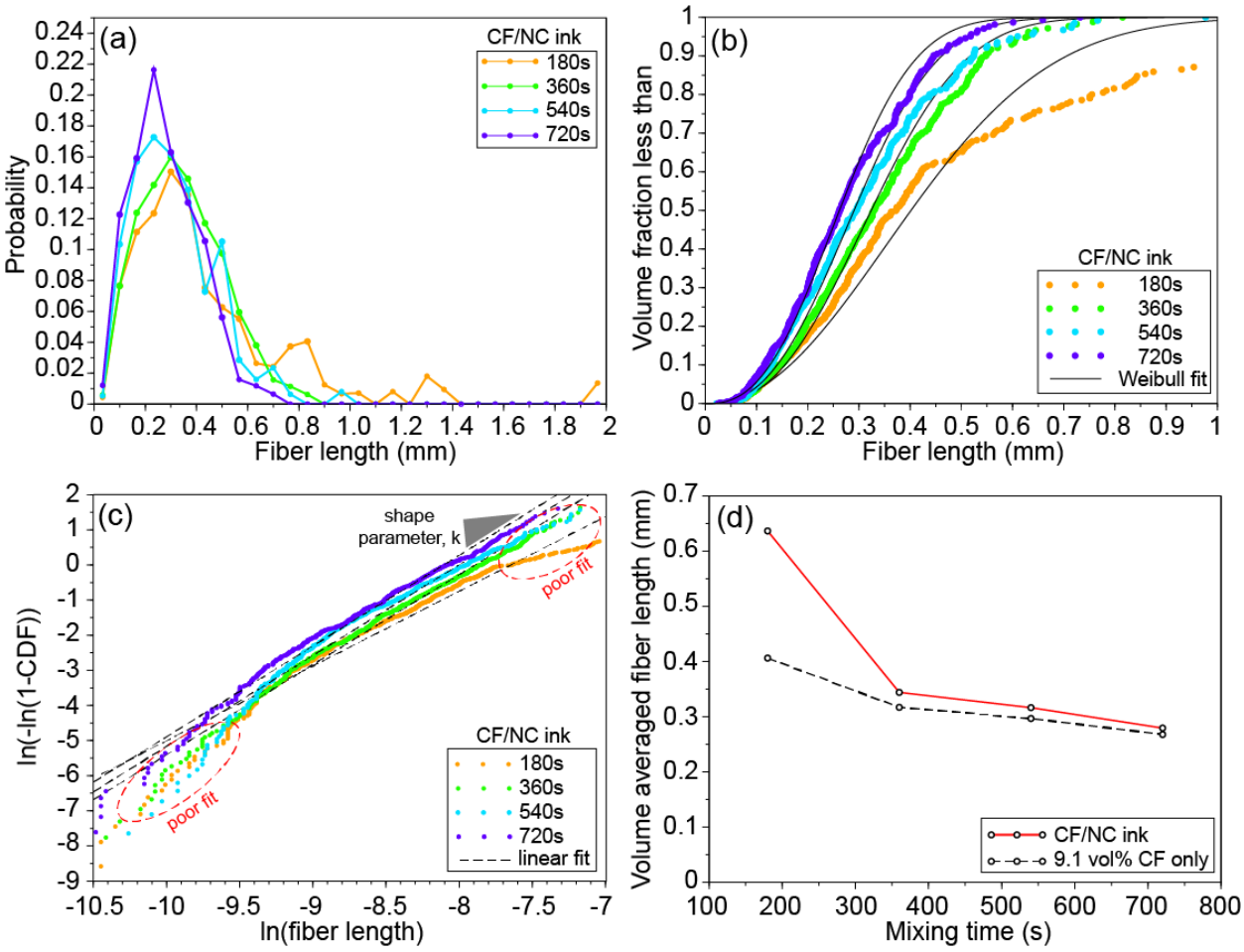

Figure 5.4: Fiber length evolution during processing of CF/NC inks: (a) FLDs for CF/NC inks mixed for different times, (b) CDFs of the corresponding FLDs shown in (a), along with fitted Weibull distributions (solid lines). (c) Weibull fit parameters computation (Eq. 5.1) for the CF/NC inks mixed for different times, along with dashed lines representing the linear regression of each dataset. (d) A comparison between the volume averaged fiber lengths measured for inks containing 9.15 vol% CF and mixed for different times, in the presence and absence of NC.

These observations can provide useful guidance on developing better CF-based inks using tailored compositions and mixing protocols.

5.4.3 Rheological behavior

The rheological behavior of epoxy-based inks of varying compositions and mixing times are shown in Figure 5.5. The unfilled epoxy resin exhibits a Newtonian behavior with a viscosity of ∼10 Pa.s that is nominally independent of shear rate over the range probed (Figure 5.5a). The incorporation of NC platelets significantly increases the viscosity of the base resin by up to three orders of magnitude at low shear rates. However, as the shear rate increases, the viscosity decreases by several orders of magnitude, undergoing strong shear-thinning behavior. This phenomenon is important to facilitate extrusion of highly loaded inks. Upon the incorporation of 9.15 vol.% CF, the CF/NC ink exhibits a viscosity that is only an order of magnitude higher than that of the epoxy/NC ink at any given shear rate below ∼8 s^{-1}, without changing its shear-thinning behavior.

Additionally, it is apparent that the mixing time does not have an impact on the viscosity profile of the epoxy/NC inks with and without CF, as they display similar apparent viscosities and shear-thinning behavior for all mixing times. The shear-thinning behavior can be quantified by fitting the apparent viscosity vs shear rate curves in Figure 5.5a to a standard power law flow model of the form [59]:

$$\eta = K\dot{\gamma}^{n-1} \tag{5.2}$$

where η is the apparent viscosity, $\dot{\gamma}$ is the shear rate, K is the consistency index and n is the flow index. n and K values were computed by linear regression over the range from 0.01 to 1 s^{-1} for all inks. n values range from 0.25 to 0.266 for the epoxy/NC inks, and from 0.188 to 0.237 for the CF/NC inks. These values indicate good shear-thinning behavior, and fall within the range of many successful DIW inks reported in literature [22, 60, 20, 59, 105, 121]. The consistency index was also computed for these inks. Table 5.3 summarizes the numerical values computed for both n and K.

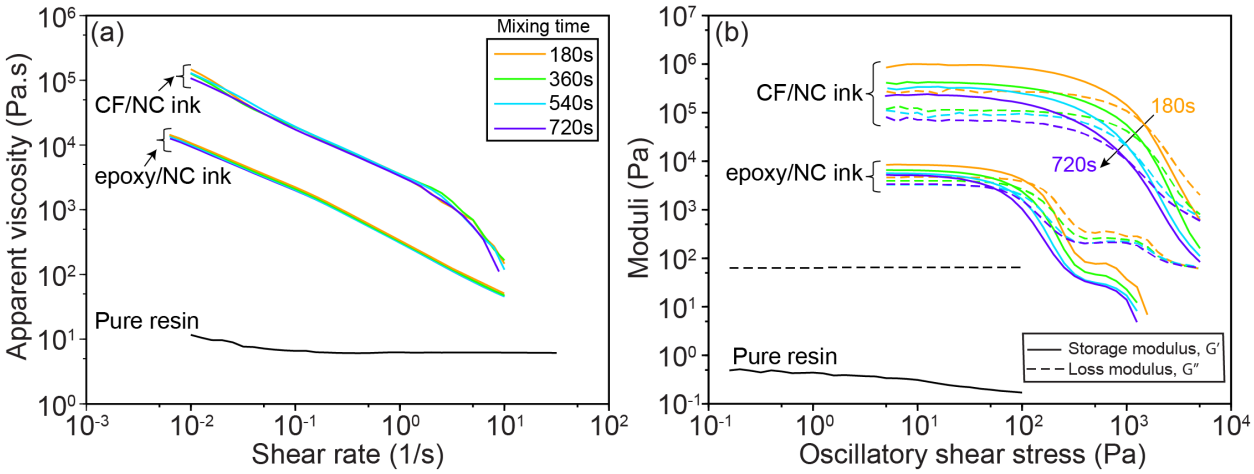

Figure 5.5: Rheological behavior of epoxy-filled inks as a function of mixing time. (a) Log-log plots of apparent viscosity as a function of shear rate. (b) The corresponding storage and loss moduli as a function of oscillatory shear stress for the inks shown in (a).

Table 5.3: Effect of mixing time on the rheological properties of epoxy/NC and epoxy/NC/CF inks

	epoxy/NC inks				CF/NC inks			
Mixing time (seconds)	n	K (Pa.s^n)	G'_0 (kPa)	τ_y (Pa)	n	K (Pa.s^n)	G'_0 (kPa)	τ_y (Pa)
180	0.254	372.3	8.443	113.3	0.188	3423.7	956.2	1519
360	0.250	352.2	6.513	82.6	0.237	3357.7	414.5	1516
540	0.250	336.5	5.614	77.0	0.212	3344.7	334.0	1101
720	0.266	343.8	5.150	56.3	0.230	3178.7	223.7	1015

Plots of the storage (G') and loss (G'') moduli of the corresponding inks are shown in Figure 5.5b. The pure resin exhibits a storage modulus (G') that is about two orders of magnitude lower than its loss modulus (G''), and both moduli are nearly independent of the applied oscillatory shear stress, indicating a liquid-like material. Upon the addition of filler materials to the pure resin, both moduli increase considerably for all inks. Inks exhibit predominantly solid-like behavior at low shear stresses, where $G' > G''$, with a well-defined shear yield stress, τ_y, represented here by the crossover point between the two moduli. At shear stresses greater than the yield stress, the ink behaves predominantly as a liquid. In contrast to the shear-thinning behavior (Figure 5.5a), the mixing time has a strong effect on the viscoelastic properties of the inks, where the storage and loss moduli and the shear yield stress are observed to decrease with increased mixing time (Figure 5.5b). The presence of CF leads to more pronounced dependence on mixing time. The steady-state, stress-independent value of the storage modulus curve before yielding ($G' > G''$) is referred to as the equilibrium storage modulus (${G'}_0$). The CF/NC ink displays higher ${G'}_0$ and τ_y values than the epoxy/NC ink across the different mixing times. ${G'}_0$ and τ_y values for each ink are summarized in Table 5.3.

The decrease in the elastic stiffness and shear yield stress of these inks with mixing time may be attributed to variations in the degree of NC exfoliation and CF length and dispersion within the epoxy resin. The shear-mixing process was reported to improve the degree of dispersion and exfoliation of filler materials within base polymers [129, 68]. At low mixing times, longer fibers tend to entangle and bundle, and the probability of the presence of non-exfoliated agglomerates of NC increases [129, 9]. This, in turn, can result in stiff inks that require higher extrusion pressure – due to the associated high shear yield stress – to enable flow through a given nozzle diameter. However, at higher mixing times, shorter fibers can disperse more easily throughout the carrier resin with less entanglement and the resin can intercalate between the NC platelets to exfoliate them to a higher degree [68, 27].

5.4.4 Printing behavior

Through a series of extrusion and printing tests, it was observed that inks containing CF alone (without NC) did not possess sufficiently solid-like behavior and viscosity to enable

printing self-stable parts. In addition, they were not able to be extruded reliably without frequently clogging the deposition nozzle, as fibers tend to entangle as they approach the nozzle exit [29]. In contrast, favorable printing behavior was obtained with the CF/NC inks. Figure 5.6a shows representative, as-printed flexural specimens printed with the CF/NC ink at varying mixing times. These inks were extruded reliably through a 864-micron-diameter nozzle at and below an extrusion pressure of 1186 kPa (172 psi) without fiber clogging. As mixing time increased, a lower pressure value was required to extrude the ink as a result of the decreased yield stress. The extrusion pressure values for the CF/NC ink as a function of mixing time are summarized in Table A.3. Moreover, all CF/NC inks were able to recover sufficient solid-like behavior after deposition, enabling flexural test specimens to be printed with minimal material spreading (Figure 5.6a). However, poor print quality is observed at the lowest mixing time.

Optical images of representative as-printed samples are shown in Figure 5.6 for the lowest and highest mixing times. Although the same nozzle size and CF content are employed, the mixing time along with the resulting FLD has a significant effect on the surface character and the quality of the printed part. At the lowest mixing time (180 s) (Figure 5.6b,d,f,h), the surface features are rough and irregular and individual fibers can be seen protruding from the printed material (Figure 5.6h). In contrast, at the highest mixing time (720 s) (Figure 5.6c,e,g,i), the as-printed surfaces are smooth, without any fibers protruding, and the printed lines appear to be mostly coalesced, potentially leading to better adhesion of the epoxy matrix between adjacent filaments compared to the mixing time of 180 s.

5.4.5 Mechanical behavior vs. mixing time

The flexural strength and flexural modulus for unidirectional composites tested along the print direction are shown in Figure 5.7 for various mixing times and numerical values are summarized in Table 5.4. Flexural strength decreases monotonically with increasing mixing time from 193.6 MPa down to 180.1 MPa for mixing times of 180s and 720s, respectively (Figure 5.7). This is consistent with composite theory that predicts higher composite strength with longer fibers [41]. However, flexural modulus values are not influenced by mixing time, with values ranging from 12.7 to 12.85 GPa.

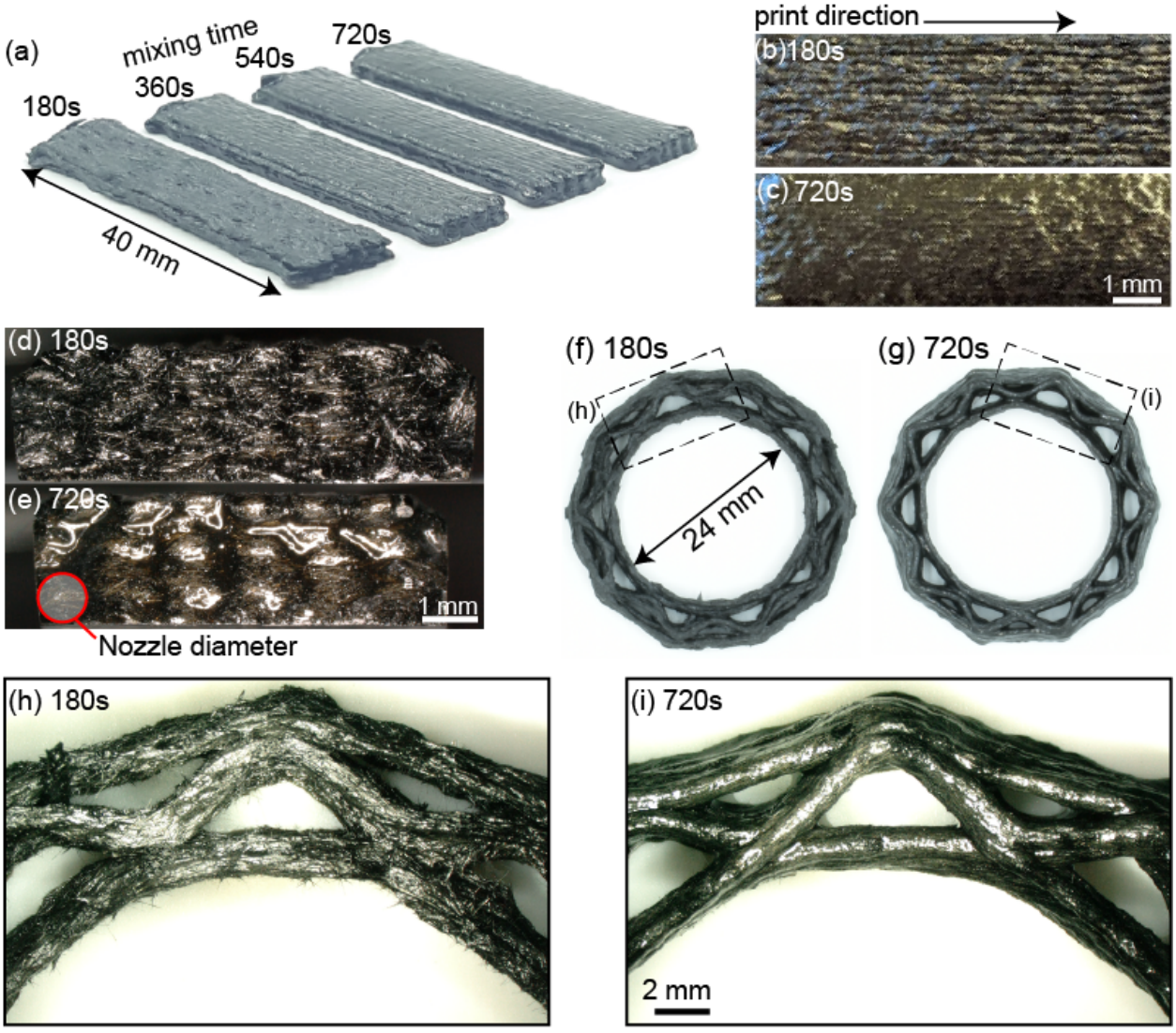

Figure 5.6: (a) Representative optical micrographs of as-printed CF/NC longitudinal flexural test specimens. (b and c) Top-view optical micrographs of as-printed longitudinal specimens for mixing times of 180 s and 720 s, as well as (d and e) end views of the same bars, and (f-i) optical micrographs of printed complex geometries for the same mixing times of 180 s and 720 s.

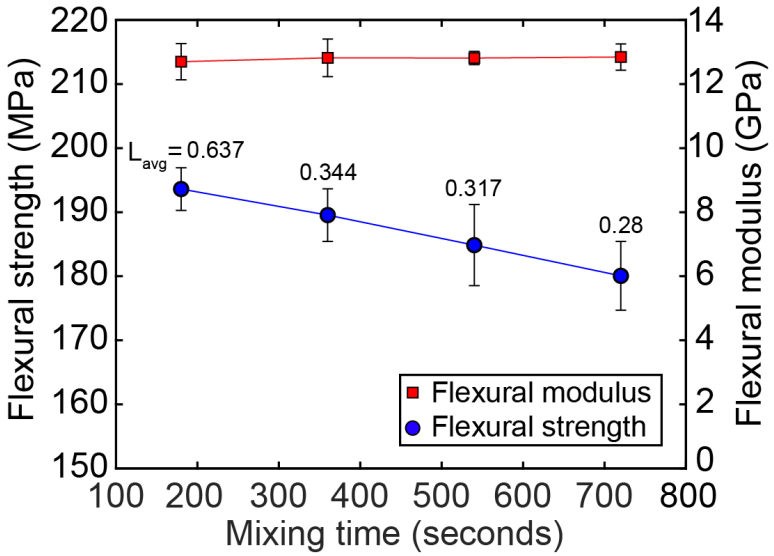

Figure 5.7: Flexural strength and stiffness of 3D-printed CF/NC longitudinal specimens as a function of mixing time.

Table 5.4: Flexural properties of printed epoxy/NC/CF composites at different mixing times

Mixing time (seconds)	Nozzle size (mm)	Print speed (mm/s)	Print path*	Flexural modulus (GPa)	Flexural strength (MPa)	Strain-to-failure (%)
180	0.864	40	L	12.70 ± 0.568	193.6 ± 3.330	1.60 ± 0.070
360	0.864	40	L	12.82 ± 0.587	189.5 ± 4.112	1.68 ± 0.080
540	0.864	40	L	12.81 ± 0.205	184.9 ± 6.335	1.60 ± 0.113
720	0.864	40	L	12.85 ± 0.411	180.1 ± 5.379	1.65 ± 0.052

*L: Longitudinal; between 7 to 10 specimens tested for each case.

5.4.6 Microscopy

Optical micrographs of representative fracture planes for longitudinal specimens are shown in Figure 5.8, looking parallel to the fracture plane (Figure 5.8a-d) and normal to the fracture plane (Figure 5.8e-h). In the parallel views, fiber pull-out is clearly visible, and the fibers are predominantly oriented along the print direction. In addition, variations in the pull-out lengths of the fibers can be observed for the different mixing times, with longer fiber pull-out lengths corresponding to the lowest mixing time (180 s) and progressively shorter pull-out length with increasing mixing time (Figure 5.8a-d), consistent with the variations in the average fiber length measured for each case.

Looking normal to the fracture plane, the fracture surface for the 180-s sample has a rougher appearance compared to the other fracture surfaces (Figure 5.8e), indicating a higher crack bifurcation rate and higher energy consumption achieved with longer fibers during fracture. Moreover, interfaces between individual filaments are not apparent in any of the fracture surfaces, and there is no delamination observed between printed layers, indicating strong matrix bonding throughout the bulk of the specimens. However, a small amount of porosity (indicated with yellow arrows) exists within the printed specimens for the lower two mixing times (Figure 5.8e,f). This porosity is attributed to the longer fibers that are more prone to forming fiber bundles and inhibiting complete dispersion. With air pressure extrusion, even though no clogging was observed with the inks of low mixing times, the variation in fiber dispersion can cause uneven flow-rate as the fiber bundles pass through the nozzle, which can lead to void formation. Part of the observed porosity could result from entrapped air pockets in the ink, introduced during loading the inks into the syringe, also leading to discontinuities during printing. Measured density values corroborate the increase in observed porosity with decreasing mixing time, as the density of the printed specimens increases from 1.248 $\pm$ 0.01 g/cm^3 to 1.262 $\pm$ 0.003 g/cm^3 as mixing time increases from 180 s to 720 s (Figure A.12).

Figure 5.9 displays representative SEM images of the select points on the fracture surfaces (indicated with white squares in Figure 5.8e-h). Fiber pull-outs are visible as exposed fibers or heart-shaped voids, matching the shape of the fiber cross-sections, distributed within the

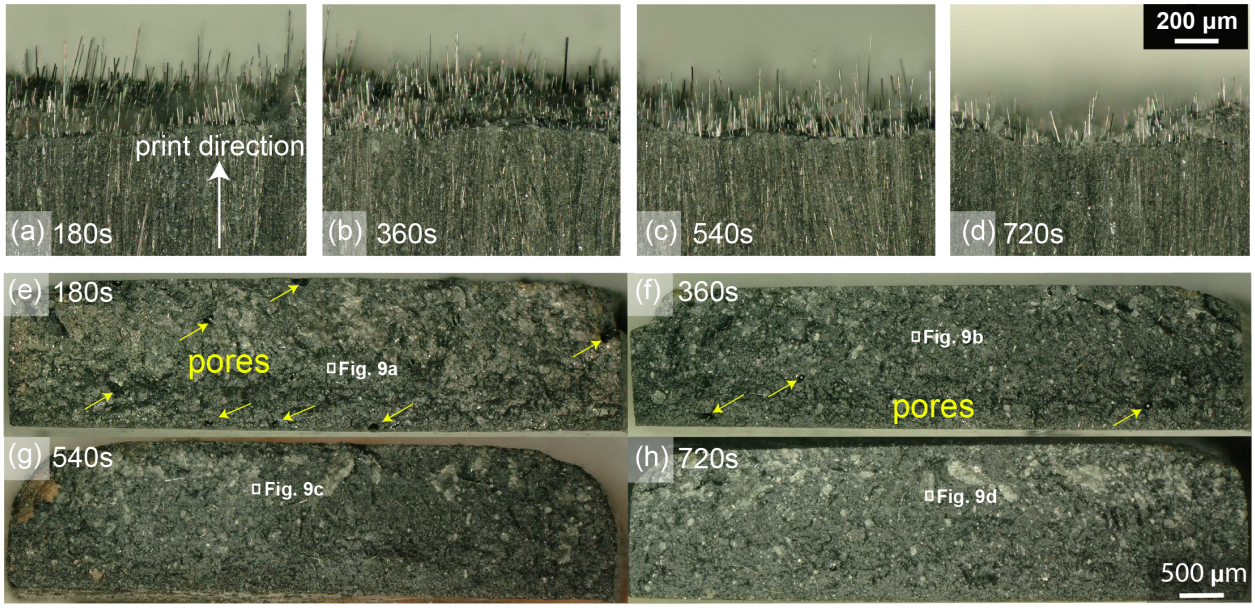

Figure 5.8: (a-d) Representative optical micrographs of the parallel-views of fracture surfaces for CF/NC longitudinal specimens showing variations in the pull-out lengths. (e-h) Representative optical micrographs of the end-views of the corresponding fracture surfaces shown in (a-d).

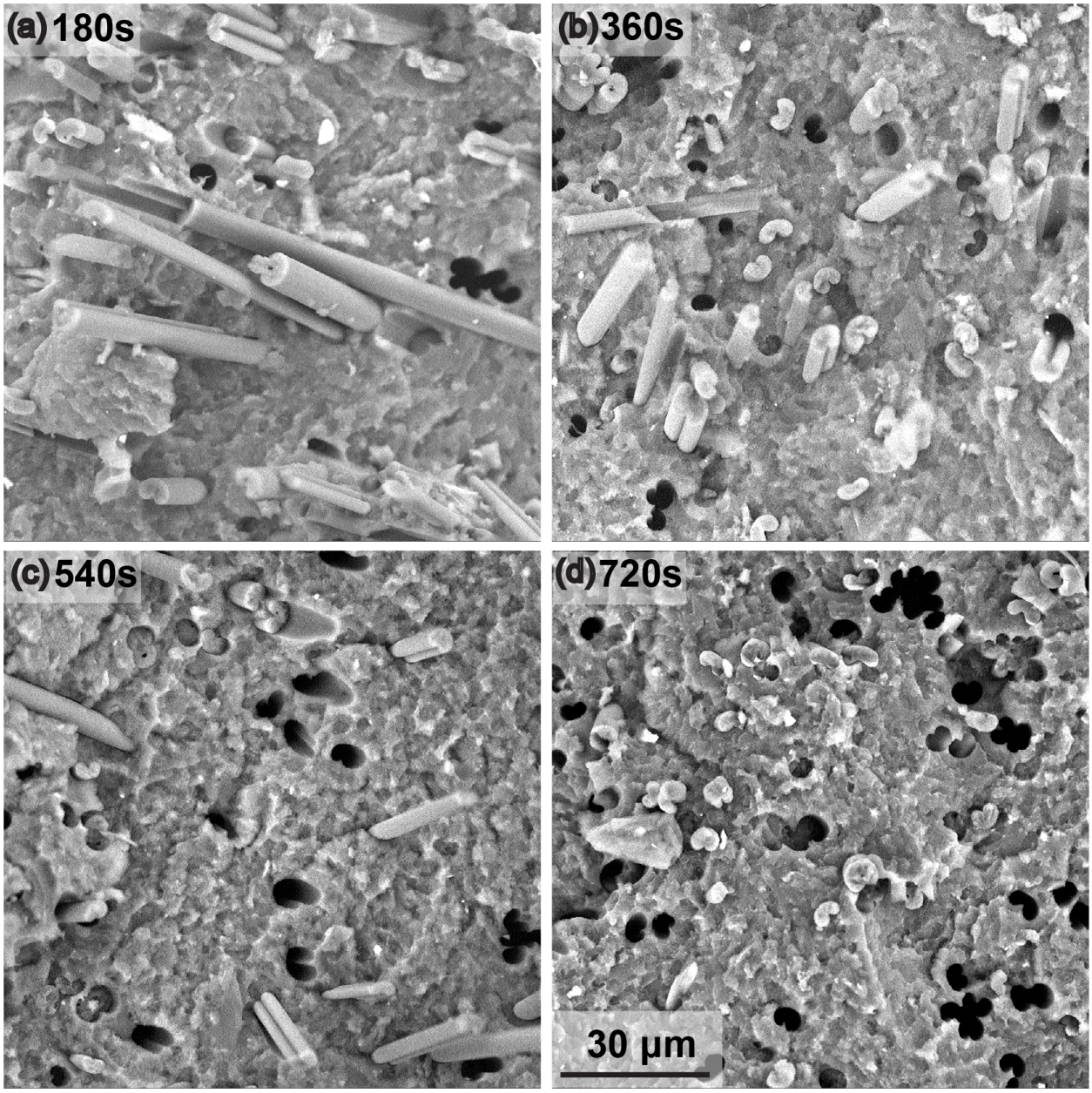

Figure 5.9: Representative SEM micrographs of selected fracture surfaces for CF/NC unidirectional flexural specimens printed with varying mixing times: (a) 180 s, (b) 360 s, (c) 540 s and (d) 720 s.

epoxy/NC matrix. It is noteworthy that the number of fibers that have been pulled from the fracture surface appears to increase with mixing time. This may be a result of the fact that a higher proportion of fibers are below the critical fiber length – discussed in the following section – with increased mixing time.

5.4.7 Mechanical property prediction vs. mixing time

Fu and Lauke proposed a modified rule-of-mixtures composite model that incorporates the effects of a realistic FLD and FOD on the composite strength through a fiber orientation factor and fiber length factor [39, 40]:

$$\sigma_{cu} = \chi_1 \chi_2 \sigma_{fu} V_f + \sigma_m V_m \tag{5.3}$$

where χ_1 is the fiber orientation factor, χ_2 is the fiber length factor, V_f is the volume fraction of fibers within the composite, σ_{fu} is the ultimate strength of the fiber, V_m is the volume fraction of the matrix, and σ_m is the strength of the matrix. This model has proven successful in predicting the mechanical properties of short fiber composites fabricated via extrusion and injection molding processes [39, 40]. More recently, Van de Werken et al. have validated the suitability of the model for predicting the strength of 3D-printed short-fiber thermoplastic composites [116]. In the following , this model is assessed against the printed composites studied here, using their measured FLD.

For unidirectional composites with fibers perfectly oriented parallel to the loading direction, $\chi_1 = 1$ [39]. In 3D-printed short fiber composites, alignment is not perfect and has been shown to depend on deposition nozzle size, print speed, and fiber content [91, 60, 110]. In the present set of experiments, because the nozzle size, print speed, and fiber content were held constant, χ_1 is assumed to adopt a constant value. On the other hand, χ_2 is expected to decrease with decreasing average fiber length or increasing mixing time. χ_2 can be directly calculated as:

$$\chi_2 = \int_{L_{min}}^{L_c} \left[L^2/(2L_c L_{average})\right] f(L)\, dL + \int_{L_c}^{L_{max}} (L/L_{average})\,(1 - L_c/2L)\, f(L)\, dL \tag{5.4}$$

where $L_{average}$ is the average fiber length, L_c is the critical fiber length, and $f(L)$ is a version of the Weibull distribution, known as the Tung distribution [39, 17]:

$$f\left(L\right) = abL^{b-1}\ exp\ \left[-aL^{b}\right] \tag{5.5}$$

where a = λ^{-k} and b = k, and λ and k are the scale and shape parameters of the Weibull distribution described in section 5.4.1. The critical fiber length, (L_c) – the minimum fiber length required to transfer sufficient load from the matrix to the fiber for fiber fracture to occur – can be defined as [39, 41]:

$$L_c = \frac{r_f\ \sigma_{fu}}{\tau_i} \tag{5.6}$$

where r_f is the fiber radius and τ_i is the interfacial shear strength between fiber and matrix. τ_i can be approximated by assuming that the interfacial shear strength is equal to the shear strength of the matrix. Assuming yield occurs according to the Tresca yield criterion:

$$\tau_i = \frac{\sigma_m}{2} \tag{5.7}$$

where σ_m is given as 100 MPa for the epoxy/NC matrix, following [59]. Therefore, from equation 5.6, the estimated value of L_c is 0.275 mm. Table 5.5 summarizes the mechanical properties of the fiber and matrix constituents.

Combing the preceding equations, the following equation is obtained:

$$\begin{aligned}\chi_2 = &\int_{L_{min}}^{L_c} \left[L^2/(2L_c a^{-1/b}\Gamma\left[(1/b)+1\right])\right] abL^{b-1}\ exp\ \left[-aL^{b}\right] dL \\ + &\int_{L_c}^{L_{max}} \left[L/(a^{-1/b}\Gamma\left[(1/b)+1\right])\right] (1-(L_c/2L))abL^{b-1}\ exp\ \left[-aL^{b}\right] dL\end{aligned} \tag{5.8}$$

From the FLDs of the CF/NC inks in Figure 5.4a, L_{min} = 5 x 10^{-6} m and L_{max} = 3 x 10^{-3} m. Based on the fitted Weibull parameters for different mixing times and CF contents (Table 5.2), k is assumed to be constant for any given volume fraction of fibers and any mixing time, while λ is assumed to decrease linearly with both mixing time and fiber volume

Table 5.5: Properties of composite constituents

Property	Value	Unit
Fiber ultimate strength, σ_{fu}	2750	MPa
Fiber elastic modulus, E_f	275.1	GPa
Fiber initial length, L_i	$\sim$6	mm
Fiber critical length, L_c	0.275	mm
Fiber radius, r_f	$\sim$5	μm
Matrix ultimate strength, σ_m	100*	MPa
Matrix elastic modulus, E_m	3.24*	GPa
Interfacial shear stress, τ_i	50*	MPa

*for the epoxy/NC base ink (5 wt% NC)

fraction (see Figure A.13 and Table A.4). Using these assumptions, χ_2 can be calculated as a function of mixing time. For the present set of experiments (V_f = 9.15 vol%), k = 2.55, and $\lambda = -0.0003\ x\ t + 0.513$, where t is the mixing time (Table A.4). Based on these inputs, χ_2 is plotted in Figure 5.10a. Computed χ_2 values are 0.64, 0.61, 0.57 and 0.53 for mixing times of 180 s, 360 s, 540 s and 720 s, respectively. Additionally, the percentage of fibers that are above L_c are 40.7%, 39%, 32% and 25.6% for the mixing times of 180 s, 320 s, 540 s, and 720 s, respectively.

Using these values for χ_2 and the fiber and matrix properties summarized in Table 5.5, experimental strength values are plotted in Figure 5.10b along with model predictions for a range of χ_1 values. The model predictions are in excellent agreement with experimental results when χ_1 = 0.65. Although the FLD clearly has an effect on the strength of the printed composites, the model predictions show that substantially greater gains in strength may be accomplished by increasing χ_1 through greater alignment of fibers along the loading direction. This will be addressed in the following section.

5.4.8 Mechanical anisotropy

To investigate the effect of nozzle size (D), print speed (ν), and print path orientation on the mechanical anisotropy in printed epoxy/CF composites, two sets of flexural specimens were printed, one with the print path oriented along (longitudinal) the long dimension of the specimen, and another oriented transverse to the long dimension of the specimen (Figure A.5). These were printed with varying combinations of nozzle size and translation print speed. Only the CF/NC ink at 720s mixing time was chosen to print the composites, since this formulation possessed the most favorable printing behavior. Figure 5.11 displays plots of the flexural properties as a function of the print speed over the nozzle diameter (ν/D).

The longitudinal samples display a slight increase in the flexural modulus with increasing ν/D ratio with values ranging from 12.57 GPa to 13.02 GPa, for ν/D = 9.6 s^{-1} and ν/D = 65.7 s^{-1}, respectively (Figure 5.11a). Conversely, the transverse samples show a slight decrease in the flexural modulus, with values ranging from 5.0 GPa to 4.7 GPa, for ν/D = 9.6 s^{-1} and ν/D = 65.7 s^{-1}, respectively. The ν/D ratio has a more pronounced effect on

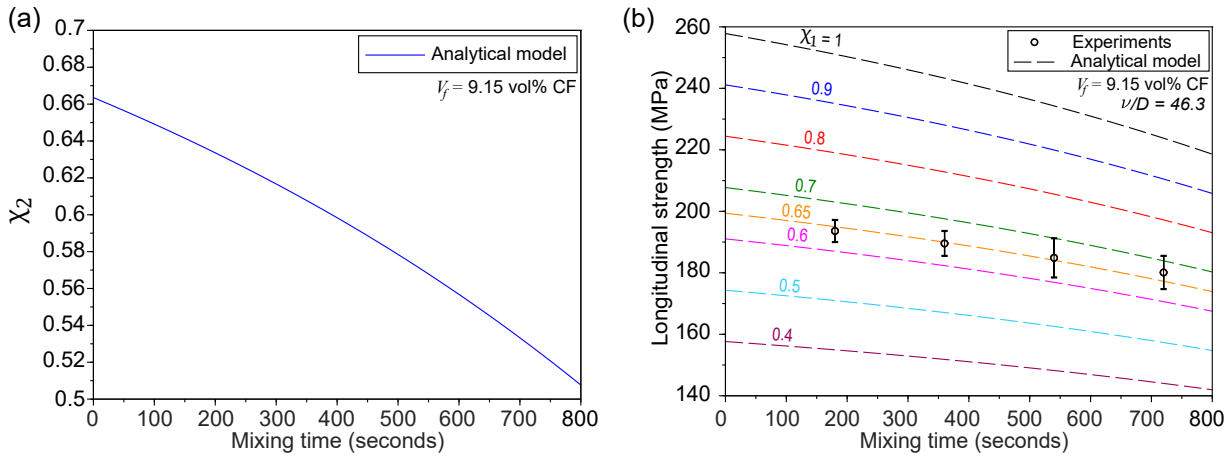

Figure 5.10: (a) χ_2 as a function of mixing time, and (b) model predictions (dashed lines) of the longitudinal composite strength as a function of mixing time and χ_1 value, plotted along with the experimental strength values.

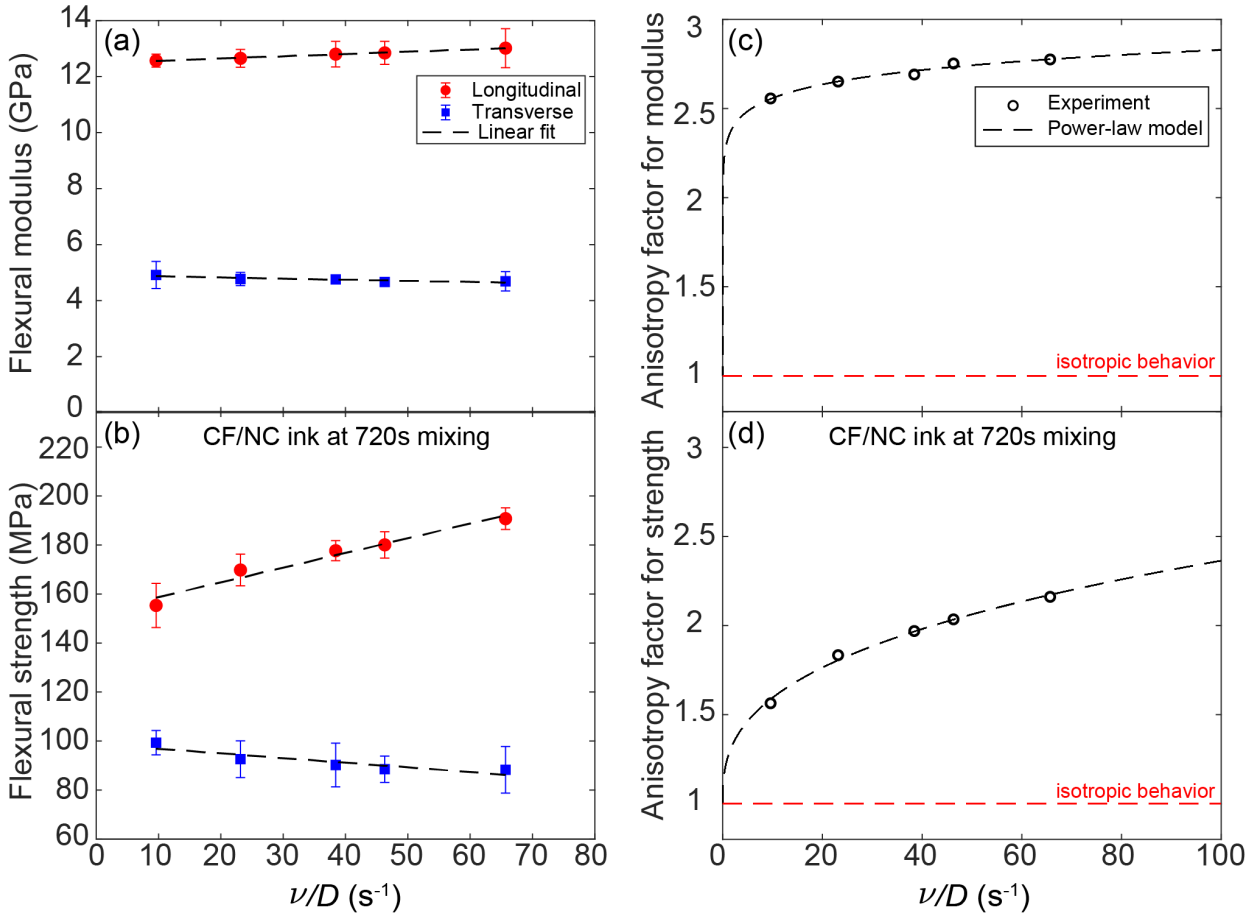

Figure 5.11: Flexural properties of longitudinal and transverse CF/NC composites printed with constant mixing time (720 s) and varying ν/D ratios. (a) Flexural modulus and (b) flexural strength. (c) and (d) Corresponding master curves of mechanical anisotropy as a function of ν/D ratio.

the strength of the printed CF/NC composites. The longitudinal strength increases linearly with increasing ν/D ratio from 155.3 MPa up to 190.7 MPa for $\nu/D = 9.6\ s^{-1}$ and $\nu/D = 65.7\ s^{-1}$, respectively. The transverse strength, on the other hand, decreases linearly from 99.3 MPa down to 88.3 MPa for $\nu/D = 9.6\ s^{-1}$ and $\nu/D = 65.7\ s^{-1}$, respectively (Figure 5.11b). All flexural measurements are summarized in Table 5.6.

The ratio of the longitudinal to transverse mechanical property can be utilized to define an anisotropy factor (ψ), following [60].The anisotropy factor for modulus ranges from 2.55 to 2.77 (Figure 5.11c), while the anisotropy factor for strength ranges from 1.56 to 2.16 (Figure 5.11d) with increasing ν/D ratio. Additionally, the two-parameter power-law model (equation 5.9) proposed in [60] is used to fit the anisotropy data:

$$\psi = 1 + A(\nu^*)^B \tag{5.9}$$

where A and B are the fitting parameters computed using non-linear regression. The computed values of A and B for this material system are 1.33 and 0.07 for modulus, and 0.26 and 0.36 for strength, respectively. The model predictions (solid lines) are plotted along with the data points in Figure 5.11c,d. In addition, a comparison between the anisotropy data of the current CF/NC material system and both the NC- and SiC-based material systems investigated in our earlier work [60] is shown in Figure A.14.

These characteristic master curves (Figure 5.11c,d and Figure A.14), which are highly dependent on the ink viscosity, the morphology of filler materials and nozzle geometry [60], can be employed to guide the optimal selection of nozzle size and print speed. This is critical to enabling the rigorous engineering design of printed composites with tailored anisotropy level and spatially programmed properties. It should be noted that an upper limit of the anisotropy factor is not predicted by the power law model, but the anisotropy factor is expected to adopt a steady-state value upon achieving maximum fiber alignment along the print direction.

These results highlight and corroborate inferences made from the composite model presented in section 5.4.7: for the epoxy/CF composites studied here, the strength of the composite is more sensitive to the extent of alignment of the short fibers than it is to the

Table 5.6: Flexural properties of printed epoxy/NC/CF composites at different print parameters

Mixing time (seconds)	Nozzle size (mm)	Print speed (mm/s)	Print path*	Flexural modulus (GPa)	Flexural strength (MPa)	Strain-to-failure (%)
	0.864	40	L	12.85 ± 0.411	180.1 ± 5.379	1.65 ± 0.052
	0.864	40	T	4.670 ± 0.093	88.50 ± 5.388	2.68 ± 0.240
	0.864	20	L	12.65 ± 0.317	169.8 ± 6.464	1.52 ± 0.098
	0.864	20	T	4.770 ± 0.235	92.60 ± 7.506	2.80 ± 0.424
720	0.609	40	L	13.02 ± 0.696	190.7 ± 4.421	1.58 ± 0.078
	0.609	40	T	4.690 ± 0.347	88.30 ± 9.525	2.75 ± 0.451
	1.041	40	L	12.80 ± 0.457	177.7 ± 4.104	1.60 ± 0.071
	1.041	40	T	4.760 ± 0.147	90.20 ± 8.930	2.65 ± 0.265
	1.041	10	L	12.57 ± 0.231	155.3 ± 9.022	1.15 ± 0.117
	1.041	10	T	4.920 ± 0.484	99.30 ± 4.982	2.75 ± 0.191

*L: Longitudinal; *T: Transverse; etween 4 to 8 specimens tested for each case.

length distribution of the fibers. Because shorter fibers lead to markedly better printing behavior, which enables printing with smaller nozzles or at higher speeds, it appears that higher fiber alignment, and thus higher mechanical properties can be achieved when inks are mixed for longer times. The relationship between fiber orientation and print parameters is evaluated in the following section.

5.4.9 Fiber orientation distribution

The improvements in mechanical properties with increasing ν/D ratio discussed in section 5.4.8 is attributed to increased fiber alignment in the printed composite. Similar trends in the flexural strength and flexural modulus have also been documented in printed epoxy composites containing either NC or a combination of NC and SiC microfibers [60]. In that work, microfiber alignment was observed with scanning electron microscopy (SEM) and quantified for the NC using small/wide angle x-ray-scattering (SAXS/WAXS) through Herman's orientation parameter. To quantify the orientation of CF for the present study, high-resolution xCT was conducted on CF/NC composites printed at $\nu/D = 9.6$ s^{-1} and $\nu/D = 65.7$ s^{-1} with a mixing time of 720s. The scanned domain comprises a 1.2 mm x 1.2 mm x 2 mm prism, with the longer dimension oriented parallel to the print direction (Figure 5.12a). After segmentation and analysis, fibers were color-coded by their angle to the print direction to give a visual representation of orientation (Figure 5.12b,c). Fibers oriented at 0° are represented by dark blue color, at 45° with green, and at 90° with red color. Qualitatively, it is apparent that fiber alignment is higher in the composite printed at $\nu/D = 65.7$ s^{-1} compared to the composite at $\nu/D = 9.6$ s^{-1}, as indicated by larger number of fibers with dark blue color (Figure 5.12c).

A histogram of fiber orientation for each sample (Figure 5.12d) quantifies the increase in fiber alignment with print speed. For example, 65% of fibers are oriented within 0°-10° of the print direction for the faster print speed, whereas only 51% of fibers have that orientation for the slower print speed. At greater mis-orientation angles, the trend is reversed, and the sample printed at a slower speed has a higher percentage of fibers at any given orientation. Orientation data and fiber counts are tabulated in Table A.5.

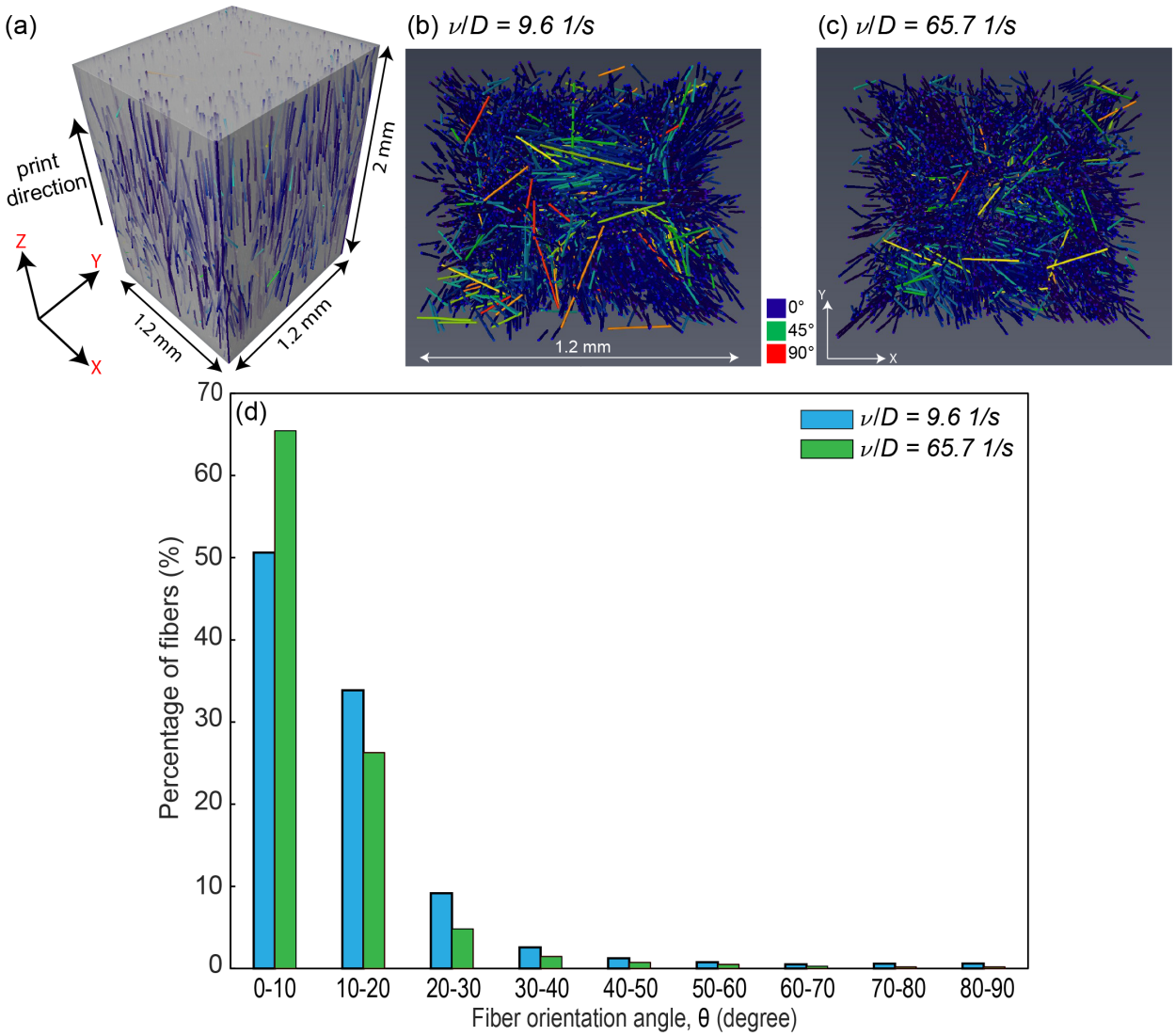

Figure 5.12: (a) xCT reconstructions showing the scanned domain of the printed specimen and the coordinate system used. (b-c) X-ray computed tomography scan data for the printed composites with $\nu/D = 9.6$ s^{-1} and $\nu/D = 65.7$ s^{-1}, respectively, with fibers colored by their angle with the Z-axis (i.e., print direction).(d) Histogram of fiber orientation calculated from xCT reconstructions.

5.5 Summary and Conclusions

In this work we have investigated the processability, rheological behavior, and mechanical properties of CF-reinforced epoxy composites for DIW 3D printing. The evolution of the fiber length during ink processing was characterized using a wide range of ink compositions and mixing times. Additionally, we have characterized the effect print parameters on mechanical anisotropy and fiber orientation in the printed composites. The key findings of this work can be summarized as follows:

- Fiber length decreases with increasing mixing time and CF content for epoxy/CF DIW composite inks. The incorporation of a rheology-modifier, such as NC platelets, into CF-filled inks allows longer fibers survive the mixing process for longer times. It was found that the FLD can be fit reasonably well using a two-parameter Weibull-type distribution function.

- Mixing time has a significant effect on the rheological properties of both epoxy/NC and CF/NC inks. Both the storage modulus and the shear yield stress of these inks decrease with increasing mixing time, while the apparent viscosity and shear-thinning behavior appears to be independent of mixing time.

- The flexural strength of the printed CF/NC composites decreases with increasing mixing time as a result of decreased fiber length, while the flexural modulus is independent of mixing time.

- Longer mixing time and shorter fibers leads to improved printing behavior and smoother printed surfaces.

- The composite model developed by Fu and Lauke that incorporates FLD and FOD to predict composite strength provides a good fit for the observe flexural strength of printed short fiber composites.

- Smaller nozzle sizes and higher print speeds lead to greater mechanical anisotropy in the printed CF/NC composites and better properties along the print direction. This is attributed to better alignment of fibers that was quantified using xCT measurements.

- For the materials and print parameters probed in this study, better mechanical properties were achieved by printing inks with shorter fibers at higher speeds or out of finer nozzles compared to inks containing longer fibers printed at lower speeds or out of larger nozzles.

5.6 Acknowledgments

This research was supported through funding from NSF under grant no. CMMI-1825815, and Honeywell Federal Manufacturing and Technologies through Contract DE-NA0002839, administrated by Dr. Jamie Messman, Mr. Steven Patterson, and Dr. Eric Eastwood. NSH and BGC would like to acknowledge partial support from the Tennessee Higher Education Commission Center for Materials Processing. Dr. Vipin Kumar would like to acknowledge support by the US Department of Energy, Office of Energy Efficiency and Renewable Energy, Advanced Manufacturing Office, under contract DE-AC05- 00OR22725 with UT-Battelle, LLC.

Chapter 6

Conclusions

6.1 Overall conclusions

The overarching goal of this dissertation was to elucidate process–structure–property relationships in 3D printed polymer composites, and to gain a better understanding of the parameters that govern microstructure, anisotropy and mechanical performance in 3D printed polymer composites. Specifically, this dissertation focused on understanding relationships between ink constituents (i.e. filler morphology and loading), ink processing conditions, ink rheology, printing parameters (i.e. nozzle size and print speed), filler orientation, and mechanical properties in 3D printed epoxy composites produced via direct ink writing (DIW) AM technology. Establishing such relationships is crucial to enabling rigorous engineering design of 3D printed composite parts, as well as optimal selection of processing parameters to obtain 3D printed composites with desirable properties. It is hoped that the work developed in this dissertation contributes to that effort.

In Chapter 3, epoxy/nanoclay (NC) inks were formulated in the absence of fiber reinforcements using different contents of NC for the use as feedstock materials for DIW 3D printing. The effects of the deposition process on the orientation/arrangements of NC platelets, thermomechanical properties and anisotropy in the 3D printed composites were investigated. The following conclusions can be drawn:

- NC platelets impart the rheological properties (i.e. shear-thinning and shear yield stress) required for DIW 3D-printing. Rheological characterization of ink formulations using a parallel plate rheometry is useful for identifying good printing behavior for DIW printing. Good printing behavior was observed in NC inks with shear yield stress and plateau elastic modulus values greater than $\sim$300 Pa and $\sim$60 kPa, respectively. It was also demonstrated that both shear yield stress and viscosity of the ink formulation dictate the surface definition and print quality of the printed composites.

- The deposition process in DIW does impart preferential and spatial orientation on high-aspect-ratio nanoscale filler materials (i.e. NC), resulting in strong mechanical anisotropy in 3D printed components. The overall alignment and final arrangements of the NC platelets in printed composites are influenced by both the shear field

experienced by the ink during extrusion and the road-to-road shear upon deposition onto the build plate (i.e. substrate).

- Epoxy/NC printed composites achieve flexural strength values up to 143 MPa and 100 MPa along and transverse to the print direction, respectively. These epoxy/NC composites demonstrate high potential for future use as a matrix material for high-strength short fiber composites.

- Despite NC content (up to 12.5 wt%) and observed mechanical anisotropy, fully dense, pore-free components can be successfully printed without inter-filamentary voids between printed layers, compared to 3D printed thermoplastics that suffer from high porosity and weak layer-to-layer bonding. However, the printing parameters, such as flow rate, layer height, and print speed must to be chosen appropriately to eliminate void formation between printed layers. In addition, the fracture surfaces of 3D printed epoxy/NC composites show no evidence of the original print path, suggesting a strong layer-to-layer bonding and thorough cross-linking between printed layers and filaments.

- Thermal properties in these 3D printed epoxy/NC materials appear to be unaffected by the printing process. However, a wide range of thermal properties should be achievable by utilizing other curing agents that impart different thermal properties.

- POM technique has proven invaluable in revealing clear evidence of microstructural architecture that correlates to individual print paths. In addition, POM has proven useful in providing information about the resulting road (or filament) geometry, mapping the road boundaries in printed composites, as well as providing qualitative information about the spatial microstructural heterogeneity in printed polymer composites.

- Nanoindentation mapping has proven beneficial in probing the local mechanical proprieties in printed composites, which correlate reasonably well with visible birefringence patterns observed in POM, as well as spatial NC arrangements probed by μSAXS.

In Chapter 4, the effects of filler morphology, nozzle size, and print speed on the mechanical properties and extent of anisotropy in 3D printed epoxy composites fabricated

via DIW were explored. Furthermore, the effects of different combinations of filler materials on the rheological requirements for DIW 3D printing were investigated. The following conclusions can be drawn:

- Explicit links between ink composition, printing parameters, mechanical properties and anisotropy in printed composites were established. Establishing such links is essential to apply any rigorous engineering principles to the design of additively manufactured parts.

- The mechanical behavior of printed epoxy/fumed silica (FS) composites display a remarkable insensitivity to printing parameters (i.e. nozzle size and print speed) and print path, with flexural strength and modulus values of 107 MPa and 3.1 GPa, respectively. This is an important finding and it demonstrates the potential that thermoset feedstocks have to address shortcomings associated with printed thermoplastics, such as weak bonding between printed layers/filaments and porosity.

- The mechanical properties (i.e. strength and stiffness) of printed composites containing high-aspect-ratio filler materials (i.e. NC and SiC) display strong sensitivity to both nozzle size and print speed. In these composites, greater mechanical anisotropy is achieved when smaller deposition nozzles and higher printing speeds are employed. X-ray scattering measurements and scanning electron microscopy (SEM) confirmed the orientation and dependence on print parameters of NC platelets and SiC whiskers in the printed composites, respectively.

- The printed SiC whisker-reinforced epoxy composites exhibit flexural strength values up to 215 MPa and $\sim$118 MPa along and transverse to the print direction, respectively. To our knowledge, these values are currently the highest reported flexural strength values for a 3D-printed whisker-reinforced polymer composite.

- For each combination of filler material and resin, we have shown that an anisotropy master curve can be constructed to describe the relationship between mechanical anisotropy and printing parameters (i.e. print speed and nozzle diameter). These

master curves allow one to make predictions of mechanical properties and anisotropy over a broad range of print parameters.

- Both NC and FS are effective at imparting the rheological requirements for DIW (i.e. strong shear-thinning and yield stress behavior). However, NC appears to be more effective than FS when combined with larger-scale filler materials (e.g., SiC whiskers).

- Finally, the findings and insights from this chapter highlight the possibility of 3D printing geometrically-complex composite components with tailored mechanical anisotropy through systematically varying print parameters (i.e. nozzle size and print speed) and ink constituents (i.e. filler morphology).

In Chapter 5, the effects of ink formulation and processing parameters on the evolution of FLD, ink rheology, and mechanical properties in 3D printed epoxy/CF composites were investigated. In addition, the effects of printing parameters (i.e. nozzle size and print speed) on FOD and mechanical anisotropy in printed composites were also characterized. The following conclusions can be drawn:

- For CF-filled DIW composite inks, fiber length decreases with increasing CF content and mixing time. However, the addition of a rheology-modifier, such as NC platelets, allows longer fibers survive the shear mixing process for longer times.

- The evolution of FLD in DIW inks can be modeled using a two-parameter Weibull-type distribution function.

- The storage modulus and the shear yield stress of DIW inks decrease with increasing mixing time, whereas the apparent viscosity and shear-thinning behavior remain unchanged.

- As opposed to CF/NC DIW inks, CF inks formulated without the incorporation of a rheology modifier cannot maintain shape after deposition as they do not possess sufficient solid-like behavior. In addition, they cannot be extruded reliably without frequently clogging the deposition nozzle, due to fiber entanglements.

- The mixing time along with the resulting FLD in significantly affects the print quality and surface character of printed CF/NC composite components. As compared to high mixing times, low mixing times result in rough surface features with protruding fibers.

- The mechanical properties of 3D printed CF/NC display pronounced dependence on mixing time. The flexural strength of printed CF/NC composites decreases monotonically with increasing mixing time, but the flexural modulus is independent of mixing time. Using an existing composite model, which predicts composite strength based on FLD and FOD, an excellent prediction of the strength of printed CF/NC composites is achieved as a function of mixing time.

- Higher normalized translation rates (i.e. smaller nozzle size and higher print speeds) lead to increased fiber alignment in the printed CF/NC composites, resulting in greater anisotropy and improved flexural properties along the print direction. X-ray computed tomography measurements confirmed fiber alignment and dependence on printing parameters in the printed composites.

- Finally, the findings and observations gained from this chapter provide useful guidance on processing and developing of CF-filled DIW inks with tailored compositions, mixing protocols and mechanical properties.

6.2 Mechanical properties

The mechanical properties (elastic modulus and fracture strength) values of all 3D printed composites presented in this work are plotted in Figure 6.1 and compared to other 3D printed thermoset polymer composites presented in section 2.5.

- The 3D printed epoxy/NC composites achieve longitudinal flexural strength and modulus values up to 173 MPa and 4.4 GPa, respectively, using a nozzle size of ~200 μm and print speed of 20 mm/s. In addition, these composites achieve transverse strength and modulus values up to 106 MPa and 3.6 GPa, respectively.

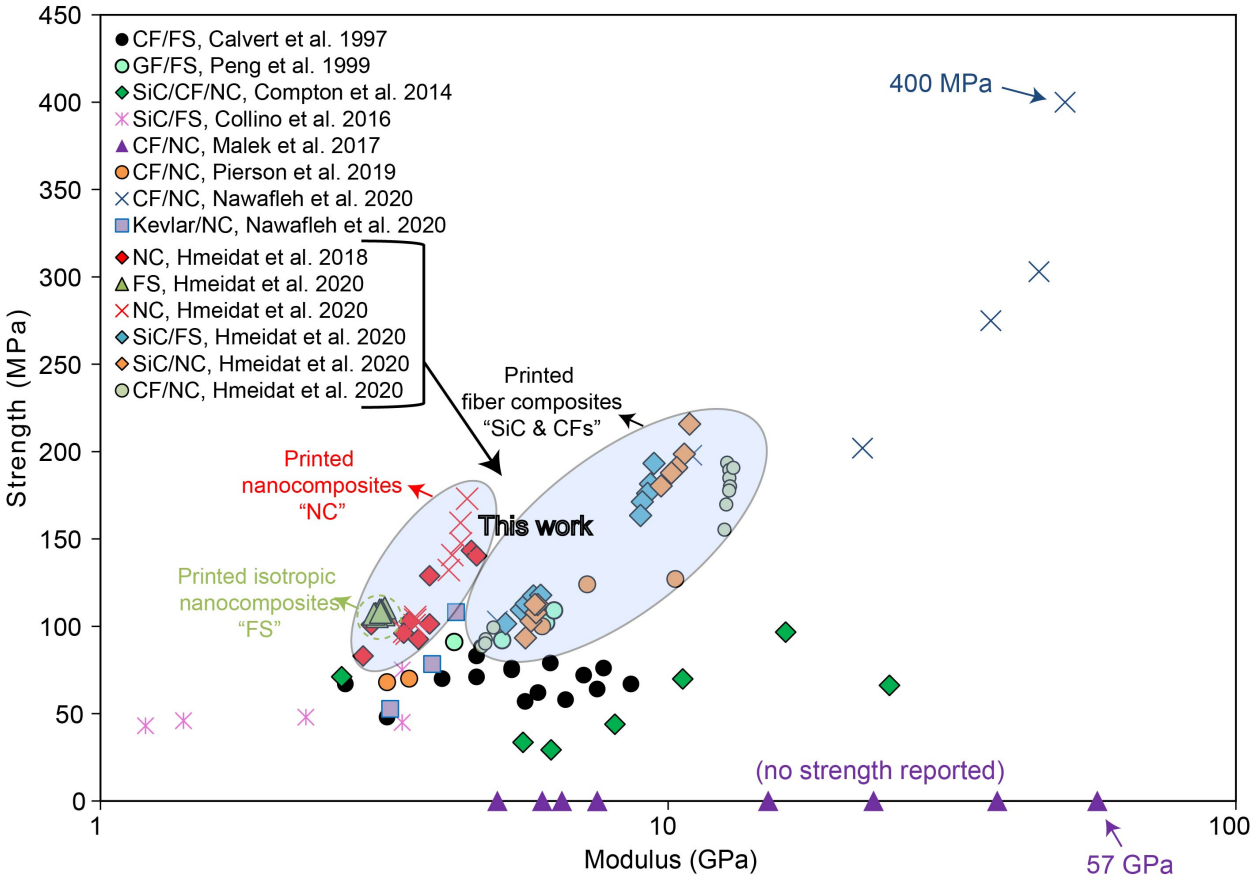

Figure 6.1: Property space map of strength versus modulus, which compare our printed epoxy-based composites in this work to other polymer composites fabricated by DIW.

- The 3D printed epoxy/FS composites exhibit isotropic flexural strength and modulus values of 107 MPa and 3.1 GPa, respectively.

- The 3D printed epoxy/SiC/NC composites achieve longitudinal flexural strength and modulus values up to 216 MPa and 11 GPa, respectively, using a nozzle size of ∼600 μm and print speed of 40 mm/s.

- The 3D printed epoxy/SiC/FS composites achieve longitudinal flexural strength and modulus values up to 193 MPa and 9 GPa, respectively, using a nozzle size of ∼600 μm and print speed of 40 mm/s.

- The 3D printed epoxy/CF/NC composites achieve longitudinal flexural strength and modulus values up to ∼194 MPa and 13 GPa, respectively, using a mixing time of 180 seconds, a nozzle size of ∼860 μm and a print speed of 40 mm/s.

- The transverse strength of the SiC whiskers- and CF-based formulations matches the strength of the isotropic fumed silica-containing formulation, but with transverse elastic modulus values up to 6 GPa.

6.3 Publications

This research has yielded four journal publications:

- **Hmeidat, N.S.**, Kemp, J.W. and Compton, B.G., (2018). High-strength epoxy nanocomposites for 3D printing. *Composites Science and Technology*, 160, pp.9-20.

- **Hmeidat, N.S.**, Pack, R.C., Talley, S.J., Moore, R.B. and Compton, B.G., (2020). Mechanical anisotropy in polymer composites produced by material extrusion additive manufacturing. *Additive Manufacturing*, 34, p.101385.

- Trigg, E. B., **Hmeidat, N. S.**, Smieska, L. M., Woll, A. R., Compton, B. G., and Koerner, H. (2021). Revealing filler morphology in 3D-printed thermoset nanocomposites by scanning microbeam X-ray scattering. *Additive Manufacturing*, 37, 101729.

- **Hmeidat, N.S.**, Elkins, D.S., Peter, H., Kumar, V., and Compton, B.G., (2021). Processing and mechanical characterization of carbon fiber-reinforced epoxy composites for material extrusion additive manufacturing. Submitted to *Composites Part B: Engineering*.

Bibliography

[1] Advani, S. G. and Tucker III, C. L. (1987). The use of tensors to describe and predict fiber orientation in short fiber composites. *Journal of rheology*, 31(8):751–784. 23, 70

[2] Agarwala, M. K., Jamalabad, V. R., Langrana, N. A., Safari, A., Whalen, P. J., and Danforth, S. C. (1996). Structural quality of parts processed by fused deposition. *Rapid prototyping journal*. 3, 69

[3] Ahn, S.-H., Montero, M., Odell, D., Roundy, S., and Wright, P. K. (2002). Anisotropic material properties of fused deposition modeling abs. *Rapid prototyping journal*. 2, 10, 31, 73

[4] Ajinjeru, C., Kishore, V., Liu, P., Lindahl, J., Hassen, A. A., Kunc, V., Post, B., Love, L., and Duty, C. (2018). Determination of melt processing conditions for high performance amorphous thermoplastics for large format additive manufacturing. *Additive Manufacturing*, 21:125–132. 10

[5] Alexandre, M. and Dubois, P. (2000). Polymer-layered silicate nanocomposites: preparation, properties and uses of a new class of materials. *Materials science and engineering: R: Reports*, 28(1-2):1–63. 32

[6] ASTM, C. (1958). Astm standards. American Society for Testing Materials Philadelphia. 79

[7] ASTM, I. (2007). Standard test methods for flexural properties of unreinforced and reinforced plastics and electrical insulating materials. *ASTM D790-07*. 36, 114

[8] Ausias, G., Agassant, J.-F., and Vincent, M. (1994). Flow and fiber orientation calculations in reinforced thermoplastic extruded tubes. *International Polymer Processing*, 9(1):51–59. 69

[9] Azeez, A. A., Rhee, K. Y., Park, S. J., and Hui, D. (2013). Epoxy clay nanocomposites–processing, properties and applications: A review. *Composites Part B: Engineering*, 45(1):308–320. 28, 32, 124

[10] Bell, J. P. (1969). Flow orientation of short fiber composites. *Journal of Composite Materials*, 3(2):244–253. 23, 69

[11] Bellini, A. and Güçeri, S. (2003). Mechanical characterization of parts fabricated using fused deposition modeling. *Rapid Prototyping Journal*. 2, 73

[12] Bose, S., Ke, D., Sahasrabudhe, H., and Bandyopadhyay, A. (2018). Additive manufacturing of biomaterials. *Progress in Materials Science*, 93:45–111. 8

[13] Calvert, P. and Crockett, R. (1997). Chemical solid free-form fabrication: making shapes without molds. *Chemistry of materials*, 9(3):650–663. 13

[14] Calvert, P., Lin, T. L., and Martin, H. (1997). Extrusion freeform fabrication of chopped-fibre reinforced composites. *High Performance Polymers*, 9(4):449–456. xv, 2, 3, 13, 17, 19, 20, 21, 23, 29, 32, 69, 106, 107

[15] Camino, G., Tartaglione, G., Frache, A., Manferti, C., and Costa, G. (2005). Thermal and combustion behaviour of layered silicate–epoxy nanocomposites. *Polymer Degradation and Stability*, 90(2):354–362. 54

[16] Chan, M.-l., Lau, K.-t., Wong, T.-t., Ho, M.-p., and Hui, D. (2011). Mechanism of reinforcement in a nanoclay/polymer composite. *Composites Part B: Engineering*, 42(6):1708–1712. 28

[17] Chin, W.-K., Liu, H.-T., and Lee, Y.-D. (1988). Effects of fiber length and orientation distribution on the elastic modulus of short fiber reinforced thermoplastics. *Polymer Composites*, 9(1):27–35. 116, 133

[18] Collino, R. R., Ray, T. R., Fleming, R. C., Cornell, J. D., Compton, B. G., and Begley, M. R. (2016). Deposition of ordered two-phase materials using microfluidic print nozzles with acoustic focusing. *Extreme Mechanics Letters*, 8:96–106. xv, 2, 3, 17, 20, 22, 25, 29, 69, 105

[19] Collino, R. R., Ray, T. R., Fleming, R. C., Sasaki, C. H., Haj-Hariri, H., and Begley, M. R. (2015). Acoustic field controlled patterning and assembly of anisotropic particles. *Extreme Mechanics Letters*, 5:37–46. 3, 69

[20] Compton, B. G., Hmeidat, N. S., Pack, R. C., Heres, M. F., and Sangoro, J. R. (2018a). Electrical and mechanical properties of 3d-printed graphene-reinforced epoxy. *Jom*, 70(3):292–297. 2, 3, 10, 13, 15, 17, 29, 69, 105, 121

[21] Compton, B. G., Kemp, J. W., Novikov, T. V., Pack, R. C., Nlebedim, C. I., Duty, C. E., Rios, O., and Paranthaman, M. P. (2018b). Direct-write 3d printing of ndfeb bonded magnets. *Materials and Manufacturing Processes*, 33(1):109–113. 2, 10, 13, 17, 18, 29

[22] Compton, B. G. and Lewis, J. A. (2014). 3d-printing of lightweight cellular composites. *Advanced materials*, 26(34):5930–5935. xv, 2, 3, 10, 15, 17, 18, 19, 20, 22, 23, 24, 25, 28, 29, 31, 33, 69, 78, 80, 82, 105, 106, 107, 112, 121

[23] Compton, B. G., Post, B. K., Duty, C. E., Love, L., and Kunc, V. (2017). Thermal analysis of additive manufacturing of large-scale thermoplastic polymer composites. *Additive Manufacturing*, 17:77–86. 2, 10, 29

[24] Compton, B. G., Wilt, J. K., Kemp, J. W., Hmeidat, N. S., Maness, S. R., Edmond, M., Wilcenski, S., and Taylor, J. (2021). Mechanical and thermal properties of 3d-printed epoxy composites reinforced with boron nitride nanobarbs. *MRS Communications*, pages 1–6. 105

[25] Dinkgreve, M., Paredes, J., Denn, M. M., and Bonn, D. (2016). On different ways of measuring "the" yield stress. *Journal of non-Newtonian fluid mechanics*, 238:233–241. 40

[26] Dinwiddie, R. B., Love, L. J., and Rowe, J. C. (2013). Real-time process monitoring and temperature mapping of a 3d polymer printing process. In *Thermosense: Thermal Infrared Applications XXXV*, volume 8705, page 87050L. International Society for Optics and Photonics. 29

[27] Drummy, L. F., Koerner, H., Farmer, K., Tan, A., Farmer, B., and Vaia, R. A. (2005). High-resolution electron microscopy of montmorillonite and montmorillonite/epoxy nanocomposites. *The Journal of Physical Chemistry B*, 109(38):17868–17878. 124

[28] Dunkerley, E., Koerner, H., Vaia, R. A., and Schmidt, D. (2011). Structure and dynamic mechanical properties of highly oriented ps/clay nanolaminates over the entire composition range. *Polymer*, 52(4):1163–1171. 28

[29] Duty, C., Ajinjeru, C., Kishore, V., Compton, B., Hmeidat, N., Chen, X., Liu, P., Hassen, A. A., Lindahl, J., and Kunc, V. (2018). What makes a material printable? a viscoelastic model for extrusion-based 3d printing of polymers. *Journal of Manufacturing Processes*, 35:526–537. 8, 10, 125

[30] Duty, C. E., Ajinjeru, C., Kishore, V., Compton, B., Hmeidat, N., Chen, X., Liu, P., Hassen, A. A., Lindahl, J. M., and Kunc, V. (2017a). A viscoelastic model for evaluating extrusion-based print conditions. Technical report, Oak Ridge National Lab.(ORNL), Oak Ridge, TN (United States). 8

[31] Duty, C. E., Kunc, V., Compton, B., Post, B., Erdman, D., Smith, R., Lind, R., Lloyd, P., and Love, L. (2017b). Structure and mechanical behavior of big area additive manufacturing (baam) materials. *Rapid Prototyping Journal*. 2, 10, 31, 69, 105

[32] Ennis, B. L., Norris, B., Das, S., and Miller, D. (2019). Evaluation of low-cost carbon fiber materials for use in wind turbine blade design seminar. Technical report, Sandia National Lab.(SNL-NM), Albuquerque, NM (United States). 109

[33] Farahani, R. D., Dubé, M., and Therriault, D. (2016). Three-dimensional printing of multifunctional nanocomposites: manufacturing techniques and applications. *Advanced Materials*, 28(28):5794–5821. 28

[34] Farkash, M. and Brandon, D. (1994). Whisker alignment by slip extrusion. *Materials Science and Engineering: A*, 177(1-2):269–275. 23, 69, 71

[35] Fernandez-Francos, X., Kazarian, S. G., Ramis, X., and Serra, À. (2013). Simultaneous monitoring of curing shrinkage and degree of cure of thermosets by attenuated total reflection fourier transform infrared (atr ft-ir) spectroscopy. *Applied spectroscopy*, 67(12):1427–1436. 29

[36] Folgar, F. and Tucker III, C. L. (1984). Orientation behavior of fibers in concentrated suspensions. *Journal of reinforced plastics and composites*, 3(2):98–119. 23, 70

[37] Frazier, W. E. (2014). Metal additive manufacturing: a review. *Journal of Materials Engineering and performance*, 23(6):1917–1928. 8

[38] Friedrich, L., Collino, R., Ray, T., and Begley, M. (2017). Acoustic control of microstructures during direct ink writing of two-phase materials. *Sensors and Actuators A: Physical*, 268:213–221. 29, 80, 105

[39] Fu, S.-Y. and Lauke, B. (1996). Effects of fiber length and fiber orientation distributions on the tensile strength of short-fiber-reinforced polymers. *Composites Science and Technology*, 56(10):1179–1190. 4, 18, 105, 107, 116, 132, 133

[40] Fu, S.-Y. and Lauke, B. (1998). An analytical characterization of the anisotropy of the elastic modulus of misaligned short-fiber-reinforced polymers. *Composites Science and Technology*, 58(12):1961–1972. 132

[41] Fu, S.-Y., Lauke, B., Mäder, E., Yue, C.-Y., and Hu, X. (2000). Tensile properties of short-glass-fiber-and short-carbon-fiber-reinforced polypropylene composites. *Composites Part A: Applied Science and Manufacturing*, 31(10):1117–1125. 4, 18, 23, 105, 107, 125, 133

[42] Galgali, G., Agarwal, S., and Lele, A. (2004). Effect of clay orientation on the tensile modulus of polypropylene–nanoclay composites. *Polymer*, 45(17):6059–6069. 28, 57, 71

[43] Giannelis, E. P. (1996). Polymer layered silicate nanocomposites. *Advanced materials*, 8(1):29–35. 28

[44] Giannotti, M. I., Galante, M. J., Oyanguren, P. A., and Vallo, C. I. (2003). Role of intrinsic flaws upon flexural behaviour of a thermoplastic modified epoxy resin. *Polymer testing*, 22(4):429–437. 79

[45] Gibson, I. and Shi, D. (1997). Material properties and fabrication parameters in selective laser sintering process. *Rapid prototyping journal*. 10

[46] Gladman, A. S., Matsumoto, E. A., Nuzzo, R. G., Mahadevan, L., and Lewis, J. A. (2016). Biomimetic 4d printing. *Nature materials*, 15(4):413–418. 69

[47] Goettler, L. A. (1974). Molding of oriented short fiber composites. iii. rate effects on fiber alignment in convergent channels. Technical report, MONSANTO RESEARCH CORP ST LOUIS MO. 70

[48] Goettler, L. A. (1984). Mechanical property enhancement in short-fiber composites through the control of fiber orientation during fabrication. *Polymer composites*, 5(1):60–71. 23, 69, 70

[49] Grejtak, T., Jia, X., Cunniffe, A. R., Shi, Y., Babuska, T. F., Pack, R. C., Vermaak, N., Compton, B. G., and Krick, B. A. (2020). Whisker orientation controls wear of 3d-printed epoxy nanocomposites. *Additive Manufacturing*, 36:101515. 105

[50] Gu, A. and Liang, G. (2003). Thermal degradation behaviour and kinetic analysis of epoxy/montmorillonite nanocomposites. *Polymer Degradation and Stability*, 80(2):383–391. 49, 54

[51] Gurusideswar, S., Velmurugan, R., and Gupta, N. (2017). Study of rate dependent behavior of glass/epoxy composites with nanofillers using non-contact strain measurement. *International Journal of Impact Engineering*, 110:324–337. 91

[52] Ha, S.-R., Rhee, K.-Y., Park, S.-J., and Lee, J. H. (2010). Temperature effects on the fracture behavior and tensile properties of silane-treated clay/epoxy nanocomposites. *Composites Part B: Engineering*, 41(8):602–607. 28

[53] Ham, Y. R., Kim, S. H., Shin, Y. J., Lee, D. H., Yang, M., Min, J. H., and Shin, J. S. (2010). A comparison of some imidazoles in the curing of epoxy resin. *Journal of Industrial and Engineering Chemistry*, 16(4):556–559. 32

[54] Haney, R., Tran, P., Trigg, E. B., Koerner, H., Dickens, T., and Ramakrishnan, S. (2020). Printability and performance of 3d conductive graphite structures. *Additive Manufacturing*, page 101618. 25, 105

[55] Harun, W., Kamariah, M., Muhamad, N., Ghani, S., Ahmad, F., and Mohamed, Z. (2018). A review of powder additive manufacturing processes for metallic biomaterials. *Powder Technology*, 327:128–151. 8

[56] Hassen, A. A., Lindahl, J., Chen, X., Post, B., Love, L., and Kunc, V. (2016). Additive manufacturing of composite tooling using high temperature thermoplastic materials. In *SAMPE Conference Proceedings, Long Beach, CA, May*, pages 23–26. 10

[57] Hassen, A. A., Noakes, M., Nandwana, P., Kim, S., Kunc, V., Vaidya, U., Love, L., and Nycz, A. (2020). Scaling up metal additive manufacturing process to fabricate molds for composite manufacturing. *Additive Manufacturing*, 32:101093. 8

[58] Hinton, T. J., Hudson, A., Pusch, K., Lee, A., and Feinberg, A. W. (2016). 3d printing pdms elastomer in a hydrophilic support bath via freeform reversible embedding. *ACS biomaterials science & engineering*, 2(10):1781–1786. 13

[59] Hmeidat, N. S., Kemp, J. W., and Compton, B. G. (2018). High-strength epoxy nanocomposites for 3d printing. *Composites Science and Technology*, 160:9–20. 27, 69, 75, 78, 79, 80, 82, 88, 105, 109, 112, 121, 133

[60] Hmeidat, N. S., Pack, R. C., Talley, S. J., Moore, R. B., and Compton, B. G. (2020). Mechanical anisotropy in polymer composites produced by material extrusion additive manufacturing. *Additive Manufacturing*, 34:101385. 68, 105, 106, 107, 110, 112, 121, 132, 138, 140

[61] Hofstätter, T., Pedersen, D. B., Tosello, G., and Hansen, H. N. (2017). State-of-the-art of fiber-reinforced polymers in additive manufacturing technologies. *Journal of Reinforced Plastics and Composites*, 36(15):1061–1073. 28

[62] Jeffery, G. B. (1922). The motion of ellipsoidal particles immersed in a viscous fluid. *Proceedings of the Royal Society of London. Series A, Containing papers of a mathematical and physical character*, 102(715):161–179. 23, 70

[63] Johnson, K. J., Wiegart, L., Abbott, A. C., Johnson, E. B., Baur, J. W., and Koerner, H. (2019). In operando monitoring of dynamic recovery in 3d-printed thermoset nanocomposites by xpcs. *Langmuir*, 35(26):8758–8768. 105

[64] Kanarska, Y., Duoss, E., Lewicki, J., Rodriguez, J., and Wu, A. (2019). Fiber motion in highly confined flows of carbon fiber and non-newtonian polymer. *Journal of Non-Newtonian Fluid Mechanics*, 265:41–52. 69, 70, 107

[65] Kelly, A. M., Perkins, E. M., Kauffman, J., and Dolma, T. (2018). Analysis of shape memory properties in 3d printed pla. xv, 11

[66] Kemp, J. W., Hmeidat, N. S., and Compton, B. G. (2020). Boron nitride-reinforced polysilazane-derived ceramic composites via direct-ink writing. *Journal of the American Ceramic Society*. 8, 13

[67] Kishore, V., Ajinjeru, C., Nycz, A., Post, B., Lindahl, J., Kunc, V., and Duty, C. (2017). Infrared preheating to improve interlayer strength of big area additive manufacturing (baam) components. *Additive Manufacturing*, 14:7–12. 10, 31

[68] Koerner, H., Misra, D., Tan, A., Drummy, L., Mirau, P., and Vaia, R. (2006). Montmorillonite-thermoset nanocomposites via cryo-compounding. *Polymer*, 47(10):3426–3435. 124

[69] Kokkinis, D., Schaffner, M., and Studart, A. R. (2015). Multimaterial magnetically assisted 3d printing of composite materials. *Nature communications*, 6(1):1–10. 3, 17, 25, 69, 105

[70] Lan, T. and Pinnavaia, T. J. (1994). Clay-reinforced epoxy nanocomposites. *Chemistry of materials*, 6(12):2216–2219. 28

[71] Langhans, K. and Roeder, E. (1992). Theoretische und experimentelle untersuchungen zur faserausrichtung beim strangpressen von kurzfaser-verbundwerkstoffen. *Materialwissenschaft und Werkstofftechnik*, 23(5):174–179. 23

[72] Lewicki, J. P., Rodriguez, J. N., Zhu, C., Worsley, M. A., Wu, A. S., Kanarska, Y., Horn, J. D., Duoss, E. B., Ortega, J. M., Elmer, W., et al. (2017). 3d-printing of meso-structurally ordered carbon fiber/polymer composites with unprecedented orthotropic physical properties. *Scientific reports*, 7(1):1–14. 3, 29, 69, 107

[73] Lewis, J. A. (2006). Direct ink writing of 3d functional materials. *Advanced Functional Materials*, 16(17):2193–2204. 10, 13, 15, 29, 32

[74] Lewis, J. A., Smay, J. E., Stuecker, J., and Cesarano, J. (2006). Direct ink writing of three-dimensional ceramic structures. *Journal of the American Ceramic Society*, 89(12):3599–3609. 13, 15

[75] Liu, J., Guo, Y., Weng, C., Zhang, H., and Zhang, Z. (2020). High thermal conductive epoxy based composites fabricated by multi-material direct ink writing. *Composites Part A: Applied Science and Manufacturing*, 129:105684. 105

[76] Love, L. J., Kunc, V., Rios, O., Duty, C. E., Elliott, A. M., Post, B. K., Smith, R. J., and Blue, C. A. (2014). The importance of carbon fiber to polymer additive manufacturing. *Journal of Materials Research*, 29(17):1893. 10, 29, 105

[77] Malek, S., Raney, J. R., Lewis, J. A., and Gibson, L. J. (2017). Lightweight 3d cellular composites inspired by balsa. *Bioinspiration & Biomimetics*, 12(2):026014. xv, 18, 19, 20, 29, 106

[78] Manapat, J. Z., Mangadlao, J. D., Tiu, B. D. B., Tritchler, G. C., and Advincula, R. C. (2017). High-strength stereolithographic 3d printed nanocomposites: graphene oxide metastability. *ACS applied materials & interfaces*, 9(11):10085–10093. 8

[79] Manning, K. B., Wyatt, N., Hughes, L., Cook, A., Giron, N. H., Martinez, E., Campbell, C. G., and Celina, M. C. (2019). Self assembly–assisted additive manufacturing: Direct ink write 3d printing of epoxy–amine thermosets. *Macromolecular Materials and Engineering*, 304(3):1800511. 80

[80] Melchert, D. S., Collino, R. R., Ray, T. R., Dolinski, N. D., Friedrich, L., Begley, M. R., and Gianola, D. S. (2019). Flexible conductive composites with programmed electrical

anisotropy using acoustophoresis. *Advanced Materials Technologies*, 4(12):1900586. 2, 3, 25, 69, 105

[81] Mohan, T., Ramesh Kumar, M., and Velmurugan, R. (2005). Rheology and curing characteristics of epoxy–clay nanocomposites. *Polymer international*, 54(12):1653–1659. 28

[82] Murty, K. N. and Modlen, G. (1977). Experimental characterization of the alignment of short fibers during flow. *Polymer Engineering & Science*, 17(12):848–853. 23, 69

[83] Nawafleh, N. and Celik, E. (2020). Additive manufacturing of short fiber reinforced thermoset composites with unprecedented mechanical performance. *Additive Manufacturing*, 33:101109. xv, 2, 3, 17, 18, 19, 20, 22, 69, 105, 106

[84] Nawafleh, N., Chabot, J., Aljaghtam, M., Oztan, C., Dauer, E., Gorguluarslan, R. M., Demir, T., and Celik, E. (2019). Additive manufacturing of kevlar reinforced epoxy composites. In *ASME International Mechanical Engineering Congress and Exposition*, volume 59377, page V02AT02A067. American Society of Mechanical Engineers. xv, 3, 17, 20

[85] Nawafleh, N., Wright, W., Dariavach, N., and Celik, E. (2020). 3d-printed thermoset syntactic foams with tailorable mechanical performance. *Journal of Materials Science*, 55(33):16048–16057. 2, 17

[86] Ning, F., Cong, W., Qiu, J., Wei, J., and Wang, S. (2015). Additive manufacturing of carbon fiber reinforced thermoplastic composites using fused deposition modeling. *Composites Part B: Engineering*, 80:369–378. 12, 106

[87] Nohales, A., Solar, L., Porcar, I., Vallo, C. I., and Gomez, C. M. (2006). Morphology, flexural, and thermal properties of sepiolite modified epoxy resins with different curing agents. *European Polymer Journal*, 42(11):3093–3101. 32, 79

[88] Pack, R. C., Romberg, S. K., Badran, A. A., Hmeidat, N. S., Yount, T., and Compton, B. G. (2020). Carbon fiber and syntactic foam hybrid materials via core–shell material

extrusion additive manufacturing. *Advanced Materials Technologies*, page 2000731. 17, 105

[89] Parandoush, P. and Lin, D. (2017). A review on additive manufacturing of polymer-fiber composites. *Composite Structures*, 182:36–53. 28

[90] Park, J. H. and Jana, S. C. (2003). Mechanism of exfoliation of nanoclay particles in epoxy- clay nanocomposites. *Macromolecules*, 36(8):2758–2768. 28

[91] Peng, J., Lin, T. L., and Calvert, P. (1999). Orientation effects in freeformed short-fiber composites. *Composites Part A: Applied Science and Manufacturing*, 30(2):133–138. xv, 2, 3, 13, 17, 19, 20, 21, 23, 25, 29, 32, 69, 71, 106, 107, 132

[92] Pierson, H., Celik, E., Abbott, A., De Jarnette, H., Gutierrez, L. S., Johnson, K., Koerner, H., and Baur, J. (2019). Mechanical properties of printed epoxy-carbon fiber composites. *Experimental Mechanics*, 59(6):843–857. xv, 2, 3, 17, 18, 20, 22, 23, 69, 105, 107, 119

[93] Pope, D. and Keller, A. (1977). Alignment of macromolecules in solution by elongational flow; a study of the effect of pure shear in a four roll mill. *Colloid and Polymer Science*, 255(7):633–643. 69

[94] Raney, J. R., Compton, B. G., Mueller, J., Ober, T. J., Shea, K., and Lewis, J. A. (2018). Rotational 3d printing of damage-tolerant composites with programmable mechanics. *Proceedings of the National Academy of Sciences*, 115(6):1198–1203. 2, 3, 17, 25, 29, 69, 105

[95] Rau, D. A., Herzberger, J., Long, T. E., and Williams, C. B. (2018). Ultraviolet-assisted direct ink write to additively manufacture all-aromatic polyimides. *ACS applied materials & interfaces*, 10(41):34828–34833. 69

[96] Rios, O., Carter, W., Post, B., Lloyd, P., Fenn, D., Kutchko, C., Rock, R., Olson, K., and Compton, B. (2018). 3d printing via ambient reactive extrusion. *Materials Today Communications*, 15:333–336. 31

[97] Rocha, V. G., Saiz, E., Tirichenko, I. S., and García-Tuñón, E. (2020). Direct ink writing advances in multi-material structures for a sustainable future. *Journal of Materials Chemistry A*, 8(31):15646–15657. 105

[98] Romberg, S. K., Islam, M., Hershey, C. J., DeVinney, M., Duty, C. E., Kunc, V., and Compton, B. G. (2020). Linking thermoset ink rheology to the stability of 3d-printed structures. *Additive Manufacturing*, page 101621. 15, 17

[99] Rose, N., Le Bras, M., Bourbigot, S., and Delobel, R. (1994). Thermal oxidative degradation of epoxy resins: evaluation of their heat resistance using invariant kinetic parameters. *Polymer degradation and stability*, 45(3):387–397. 54

[100] Saber-Samandari, S., Khatibi, A. A., and Basic, D. (2007). An experimental study on clay/epoxy nanocomposites produced in a centrifuge. *Composites Part B: Engineering*, 38(1):102–107. 28

[101] Sames, W. J., List, F., Pannala, S., Dehoff, R. R., and Babu, S. S. (2016). The metallurgy and processing science of metal additive manufacturing. *International materials reviews*, 61(5):315–360. 8

[102] Shen, A., Peng, X., Bailey, C. P., Dardona, S., and Ma, A. W. (2019). 3d printing of polymer-bonded magnets from highly concentrated, plate-like particle suspensions. *Materials & Design*, 183:108133. 69

[103] Shi, Q., Yu, K., Kuang, X., Mu, X., Dunn, C. K., Dunn, M. L., Wang, T., and Qi, H. J. (2017). Recyclable 3d printing of vitrimer epoxy. *Materials Horizons*, 4(4):598–607. 13

[104] Shofner, M., Lozano, K., Rodríguez-Macías, F., and Barrera, E. (2003). Nanofiber-reinforced polymers prepared by fused deposition modeling. *Journal of applied polymer science*, 89(11):3081–3090. 12, 105

[105] Siqueira, G., Kokkinis, D., Libanori, R., Hausmann, M. K., Gladman, A. S., Neels, A., Tingaut, P., Zimmermann, T., Lewis, J. A., and Studart, A. R. (2017). Cellulose

nanocrystal inks for 3d printing of textured cellular architectures. *Advanced Functional Materials*, 27(12):1604619. 15, 17, 82, 121

[106] Spoerk, M., Savandaiah, C., Arbeiter, F., Traxler, G., Cardon, L., Holzer, C., and Sapkota, J. (2018). Anisotropic properties of oriented short carbon fibre filled polypropylene parts fabricated by extrusion-based additive manufacturing. *Composites Part A: Applied Science and Manufacturing*, 113:95–104. 69

[107] Standard, A. et al. (2012). Standard terminology for additive manufacturing technologies. *ASTM International F2792-12a*. 8, 105

[108] Stansbury, J. W. and Idacavage, M. J. (2016). 3d printing with polymers: Challenges among expanding options and opportunities. *Dental Materials*, 32(1):54–64. 69

[109] Takahashi, K. and Choi, N.-S. (1991). Influence of fibre weight fraction on failure mechanisms of poly (ethylene terephthalate) reinforced by short-glass-fibres. *Journal of materials science*, 26(17):4648–4656. 116

[110] Tekinalp, H. L., Kunc, V., Velez-Garcia, G. M., Duty, C. E., Love, L. J., Naskar, A. K., Blue, C. A., and Ozcan, S. (2014). Highly oriented carbon fiber–polymer composites via additive manufacturing. *Composites Science and Technology*, 105:144–150. 4, 10, 12, 18, 23, 25, 69, 105, 106, 107, 132

[111] Therriault, D., White, S. R., and Lewis, J. A. (2007). Rheological behavior of fugitive organic inks for direct-write assembly. *Applied Rheology*, 17(1):10112–1. 29

[112] Travitzky, N., Bonet, A., Dermeik, B., Fey, T., Filbert-Demut, I., Schlier, L., Schlordt, T., and Greil, P. (2014). Additive manufacturing of ceramic-based materials. *Advanced engineering materials*, 16(6):729–754. 8

[113] Trevelyan, B. and Mason, S. (1951). Particle motions in sheared suspensions. i. rotations. *Journal of Colloid Science*, 6(4):354–367. 70

[114] Trigg, E. B., Hmeidat, N. S., Smieska, L. M., Woll, A. R., Compton, B. G., and Koerner, H. (2021). Revealing filler morphology in 3d-printed thermoset nanocomposites

by scanning microbeam x-ray scattering. *Additive Manufacturing*, 37:101729. xviii, 27, 37, 62, 63, 105

[115] Ularych, F., Sova, M., Vokrouhlecy, J., and Turčić, B. (1993). Empirical relations of the mechanical properties of polyamide 6 reinforced with short glass fibers. *Polymer composites*, 14(3):229–237. 116

[116] van de Werken, N., Tekinalp, H., Khanbolouki, P., Ozcan, S., Williams, A., and Tehrani, M. (2020). Additively manufactured carbon fiber-reinforced composites: State of the art and perspective. *Additive Manufacturing*, 31:100962. 8, 105, 132

[117] Wang, T.-M., Xi, J.-T., and Jin, Y. (2007). A model research for prototype warp deformation in the fdm process. *The International Journal of Advanced Manufacturing Technology*, 33(11-12):1087–1096. 29

[118] Wang, X., Jiang, M., Zhou, Z., Gou, J., and Hui, D. (2017). 3d printing of polymer matrix composites: A review and prospective. *Composites Part B: Engineering*, 110:442–458. 8, 28, 69

[119] Warrier, J., Munshi, V., and Chidambareswaran, P. (1987). Calculating herman's orientation factor. *Textile Research Journal*, 57(9):554–555. 91

[120] Watanabe, H., Kimura, T., and Yamaguchi, T. (1989). Particle orientation during tape casting in the fabrication of grain-oriented bismuth titanate. *Journal of the American Ceramic Society*, 72(2):289–293. 71

[121] Wei, T.-S., Ahn, B. Y., Grotto, J., and Lewis, J. A. (2018). 3d printing of customized li-ion batteries with thick electrodes. *Advanced Materials*, 30(16):1703027. 82, 121

[122] Weng, Z., Wang, J., Senthil, T., and Wu, L. (2016). Mechanical and thermal properties of abs/montmorillonite nanocomposites for fused deposition modeling 3d printing. *Materials & Design*, 102:276–283. 12, 105

[123] Williams, J., Post, B., Love, L. J., and Blue, C. (2019). Opportunities for lighter weight and lower total cost component manufacturing. In *Light Weighting for Defense, Aerospace, and Transportation*, pages 1–26. Springer. xv, 9

[124] Wittemann, F., Maertens, R., Kärger, L., and Henning, F. (2019). Injection molding simulation of short fiber reinforced thermosets with anisotropic and non-newtonian flow behavior. *Composites Part A: Applied Science and Manufacturing*, 124:105476. 69

[125] Wu, M. and Messing, G. L. (1994). Fabrication of oriented sic-whisker-reinforced mullite matrix composites by tape casting. *Journal of the American Ceramic Society*, 77(10):2586–2592. 71

[126] Xu, C., Quinn, B., Lebel, L. L., Therriault, D., and L'Esperance, G. (2019). Multi-material direct ink writing (diw) for complex 3d metallic structures with removable supports. *ACS applied materials & interfaces*, 11(8):8499–8506. 13

[127] Xu, C., Wu, Q., L'Espérance, G., Lebel, L. L., and Therriault, D. (2018). Environment-friendly and reusable ink for 3d printing of metallic structures. *Materials & Design*, 160:262–269. 13

[128] Yang, D., Zhang, H., Wu, J., and McCarthy, E. D. (2021). Fibre flow and void formation in 3d printing of short-fibre reinforced thermoplastic composites: An experimental benchmark exercise. *Additive Manufacturing*, 37:101686. 115

[129] Yasmin, A., Abot, J. L., and Daniel, I. M. (2003). Processing of clay/epoxy nanocomposites by shear mixing. *Scripta materialia*, 49(1):81–86. 124

[130] Yeole, P., Hassen, A. A., Kim, S., Lindahl, J., Kunc, V., Franc, A., and Vaidya, U. (2020). Mechanical characterization of high-temperature carbon fiber-polyphenylene sulfide composites for large area extrusion deposition additive manufacturing. *Additive Manufacturing*, page 101255. 12

[131] Zadpoor, A. A. and Malda, J. (2017). Additive manufacturing of biomaterials, tissues, and organs. 8

[132] Zhang, M., Guo, R., Chen, K., Wang, Y., Niu, J., Guo, Y., Zhang, Y., Yin, Z., Xia, K., Zhou, B., et al. (2020). Microribbons composed of directionally self-assembled nanoflakes as highly stretchable ionic neural electrodes. *Proceedings of the National Academy of Sciences*. 174

[133] Zhong, W., Li, F., Zhang, Z., Song, L., and Li, Z. (2001). Short fiber reinforced composites for fused deposition modeling. *Materials Science and Engineering: A*, 301(2):125–130. 12, 105

[134] Zotti, A., Borriello, A., Ricciardi, M., Antonucci, V., Giordano, M., and Zarrelli, M. (2015). Effects of sepiolite clay on degradation and fire behaviour of a bisphenol a-based epoxy. *Composites Part B: Engineering*, 73:139–148. 28, 32, 54

Appendices

A Supplemental Information

A.1 Rheological and printing behavior of epoxy/fumed silica inks

Fumed silica-filled epoxy inks containing up to 10 wt% FS were formulated. Curves of the apparent viscosity vs shear rate are plotted in Figure A.1a for each ink formulation investigated. The corresponding viscoelastic properties of these inks are plotted in Figure A.1b. Using the power law model (equation 3.1), the numerical values for n and K were computed by linear regression over the linear portions of the viscosity curves in Figure A.1a between 0.1 and 1 s^{-1} for all formulations. Table A.1 summarizes all the measured rheological parameters. The consistency index correlates strongly with the amount of FS. For all ink, the presence of FS results in a flow index much less than one, without a strong correlation between the amount of FS and flow index. All formulations containing greater than 2.5wt% FS exhibit flow index values less than 0.2, indicating a strong shear thinning behavior. The plateau elastic modulus, G'_0, values range from 0.227 x 10^3 Pa, for the formulation containing 2.5 wt.% FS, up to 3.975 x 10^4 Pa for the formulation containing 10 wt.% FS. Shear yield stress values increase with increasing FS content from 70 Pa for the 2.5 wt.% formulation to 0.6 x 10^3 Pa for the 10 wt.% formulation.

Through a series of printing tests, it was observed that inks containing 3.5 wt% FS and less, did not possess sufficiently solid-like behavior to print multiple layers without significant flow and spreading of the lower layers. The ink formulation containing 5 wt% FS (τ_y = 220 Pa) did not recover a sufficient solid-like behavior after deposition to enable layers to be printed without geometric distortion. Figure A.2a shows the end view of a printed surface using the ink with 5 wt% FS. It is observed that the surface of the printed part is smooth, and the locations of the individual printed filaments are completely lost. Inks with 7.5 and 10 wt% FS ($\tau_y > 500$ Pa) were able to recover sufficiently solid-like behavior after deposition, enabling the printing of flexure specimens comprising of eight layers with minimal spreading, as shown in Figure A.2b and c, respectively.

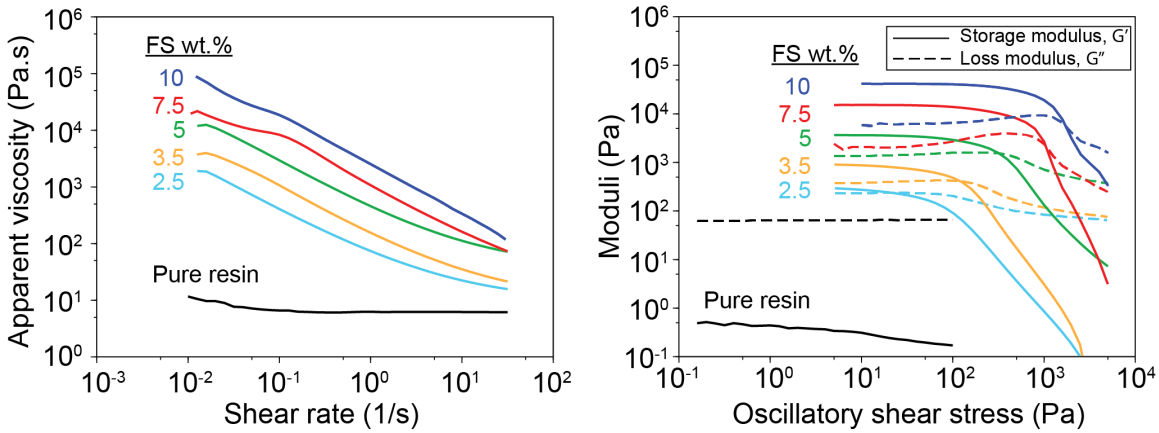

Figure A.1: Rheological behavior of epoxy/fumed silica (FS) inks: (left) log-log plots of apparent viscosity as a function of shear rate and (right) the corresponding storage and loss moduli versus oscillatory shear stress.

Table A.1: Rheological properties of epoxy/FS ink formulations

NC (wt.%)	G_0' (kPa)	τ_y (Pa)	K (Pa.s^n)	n
0.0	–	–	6.24	0.995
2.5	0.227	69.84	71.70	0.2563
3.5	0.784	119.35	151.4	0.1602
5	3.589	219.63	447.8	0.1894
7.5	15.36	517.41	1082.1	0.0789
10	39.75	599.83	2524.0	0.1222

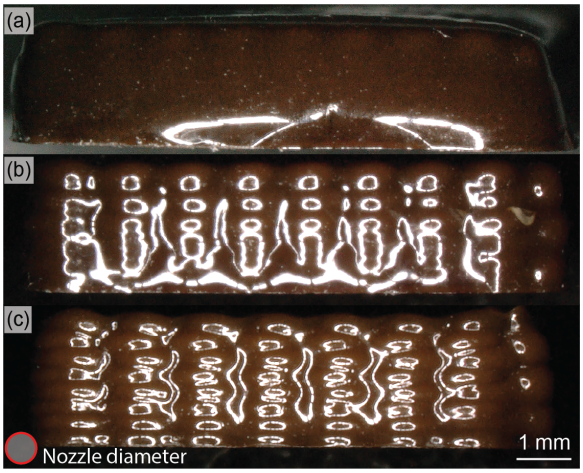

Figure A.2: Optical micrographs of the as-printed ends of representative epoxy/FS longitudinal rectangular bars: (a) contains 5 wt.% FS, (b) contains 7.5 wt.% FS, and (c) contains 10 wt.% FS.

A.2 Finite-element-based COMSOL analysis

To understand the influence of the flow fields in the deposition nozzle on the resultant NC orientation, computational fluid dynamics simulations were conducted using the COMSOL Multiphysics software (version 5.5). The analysis was conducted for the 10 wt% NC epoxy-based ink flowing through the 609 μm metal-tapered nozzle. A 2D axisymmetric laminar flow model is considered in the simulation. The numerical simulation considers the ink to be incompressible and follows the typical non-Newtonian flow behavior. By fitting the viscosity vs shear rate data in Figure 3.2a by the power law model ($\eta = K\ \dot{\gamma}^{n-1}$), we obtain the corresponding parameters $K = 3160$ Pa.s^n and $n = 0.0399$ for the 10 wt% NC epoxy-based ink (see Table 3.2). The computed K and n values are applied to the numerical simulation. The density of the ink is measured to be 1230 kg/cm^3 (see Table 3.1). The Navier-Stokes equation governs the laminar flow in the COMSOL Multiphysics software [132]. This equation is solved with the corresponding geometry of the deposition nozzle shown in Figure A.3. The obtained velocity and shear rate distributions are shown in Figure A.4.

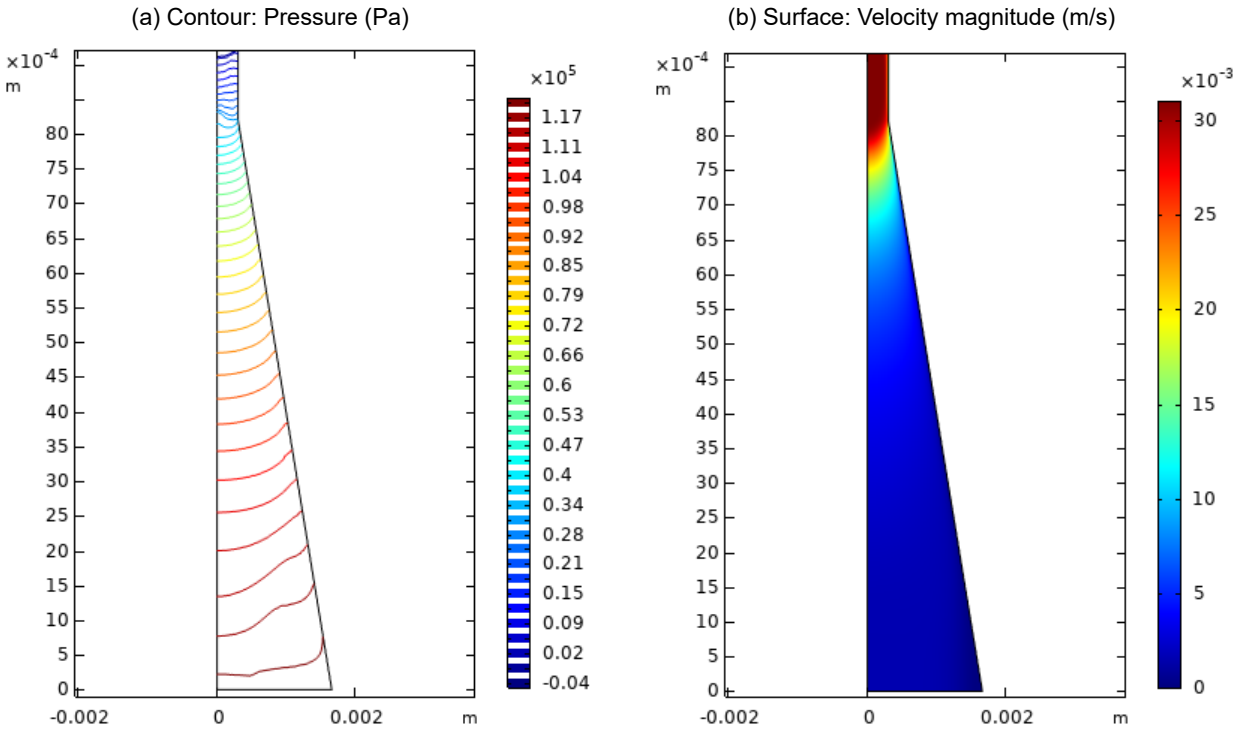

Figure A.3: COMSOL analysis of the flow of the 10 wt% NC epoxy-based ink through a tapered printing nozzle with an outlet diameter of 609 μm: (a) pressure contours and (b) velocity magnitude within the deposition nozzle.

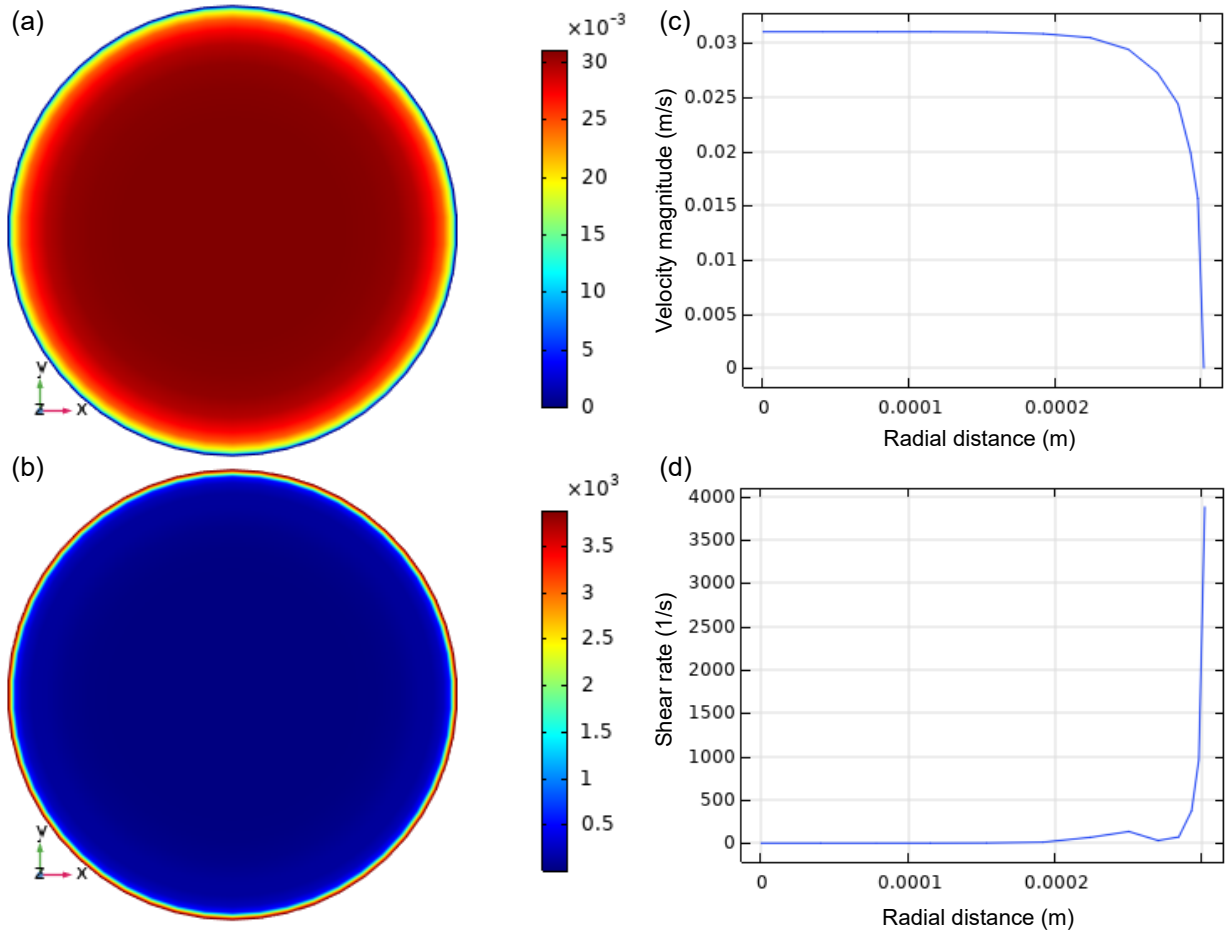

Figure A.4: COMSOL analysis of the flow of the 10 wt% NC epoxy-based ink through a tapered printing nozzle with an outlet diameter of 609 μm. Distributions of (a) the velocity magnitude (m/s) and (b) the shear rate (1/s) at the outlet of the deposition nozzle. 2D profiles of (c) the velocity and (d) the shear rate as a function of radial distance in the deposition nozzle

A.3 Print paths

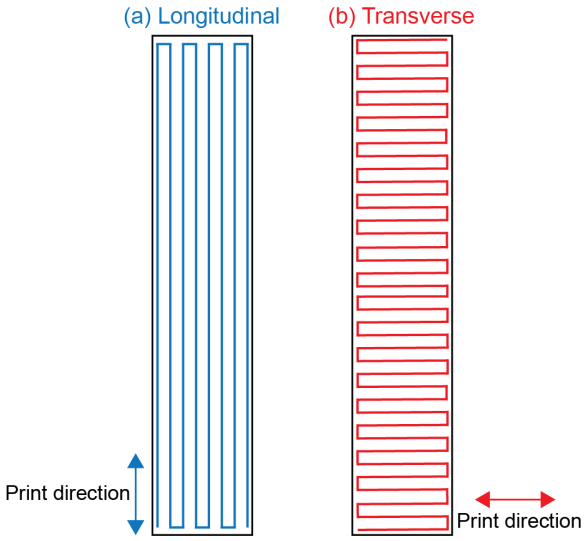

Figure A.5: 2D schematic illustrations of the print paths employed in this work: (a) the longitudinal print path and (b) the transverse print path. It can be observed that the printed filaments or lines are oriented parallel and orthogonal relative to the length of the sample for the longitudinal and transverse print paths, respectively.

A.4 Rheology of single-filler ink materials

Figure A.6 shows the rheological behavior of epoxy-based mixtures with single-filler material. Pure epoxy resin acts as a Newtonian fluid, with a nearly rate-independent viscosity of 10 Pa.s over the shear rate range probed (Figure A.6a). Addition of filler materials (5 wt.% FS, 5 wt.% FS and 34 wt.% SiC) produces a significant increase in viscosity at low shear rates and pronounced shear thinning behavior is observed. Both the FS and NC inks (at low content) display similar apparent viscosities and shear thinning behavior within the shear rate range 10^1 to 10^0. The SiC ink also shows a shear thinning behavior with an apparent viscosity of $\sim 10^4$ Pa.s at the lowest shear rate probed (10^{-2} s^{-1}).

Measurements of storage (G') and loss (G'') moduli are plotted in Figure A.6b. For the pure resin, the shear loss modulus is stress-independent ($\sim$100 Pa) and is about two orders of magnitude higher than its elastic modulus, characteristic of a viscous fluid. As fillers are added to the epoxy resin, both the loss and storage moduli increase, and at low applied stress, both NC and FS inks display solid-like behavior, where the storage modulus is higher than the loss modulus. At higher stresses, the inks yield and flow, indicated by a steep drop in storage modulus. The yield stress approximated by the crossover point of the two moduli, indicates a transition from solid-like to liquid-like behavior. Compared to FS, the NC ink imparts a higher storage modulus with a lower yield strength (τ_y = 100 Pa), whereas FS imparts a higher yield strength (τ_y = 320 Pa) at a lower storage modulus. Although the 5wt.% NC and 5wt.% FS inks are shown to have shear-thinning, viscoelastic, and yielding properties, they were not stiff enough to print flexure specimens without considerable sagging and flowing of the lower layers. Although the SiC ink imparts good shear thinning, it is not sufficient by itself to formulate stable (i.e. printable) inks for direct ink writing, since it does not impart a yield stress ($\tau_y = 0$) and it behaves predominantly as a viscos fluid, indicated by its loss modulus that is higher than its storage modulus ($G'' > G'$) over the entire range of shear stress probed. Thus, a second filler material (NC or FS) is required to be added along with SiC whiskers to act as a rheology modifier.

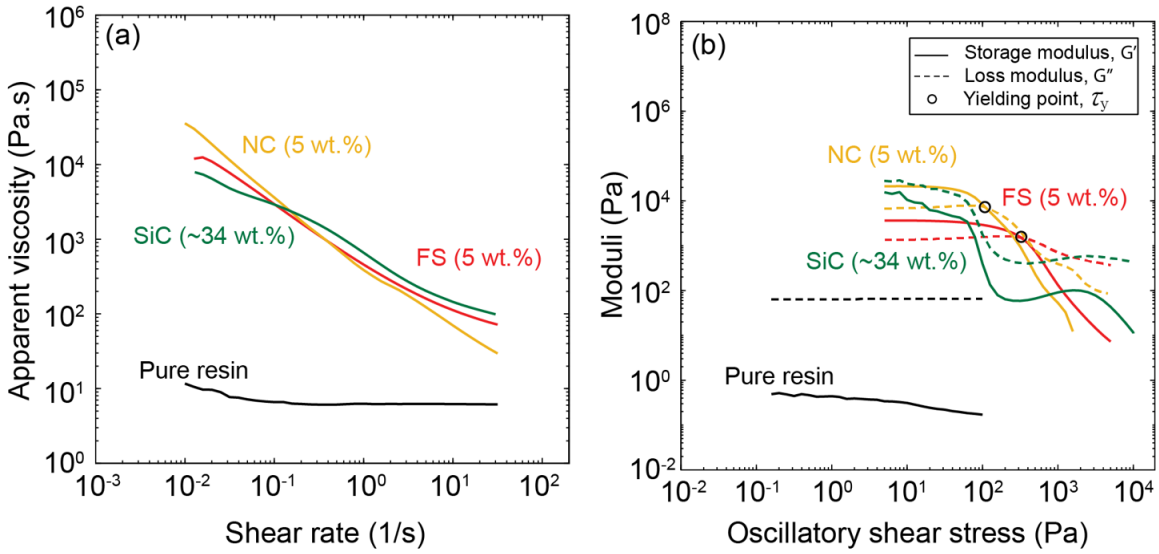

Figure A.6: Rheological behavior of epoxy-based mixtures with single-filler material. (a) log-log plots of apparent viscosity as a function of shear rate and (b) the corresponding storage and loss moduli versus oscillatory shear stress for the inks shown in (a). The shear yield stress values are measured from the crossover point between the two moduli shown in (b).

A.5 Extrusion pressure values – Chapter 4

Table A.2: Extrusion pressure values for each material system and print parameters

Filler material	Nozzle size, D (μm)	Print speed, ν (mm/s)	Extrusion pressure (psi)	ν/D (s^{-1})
FS	233	20	75	85.84
	609	20	39	32.84
	1041	20	35	19.21
	609	10	36	16.42
	609	40	55	65.70
NC	233	20	70	85.84
	609	20	38	32.84
	1041	20	32	19.21
	609	10	34	16.42
	609	40	53	65.70
SiC/NC*	609	20	188	32.84
	864	20	168	23.15
	1041	20	140	19.21
	609	10	160	16.42
	609	40	228	65.70
SiC/FS	609	20	40	32.84
	864	20	30	23.15
	1041	20	28	19.21
	609	10	30	16.42
	609	40	55	65.70

*a pressure adapter (HP3, Nordson EFD, Westlake, OH) was used for this ink.

A.6 Fracture surfaces

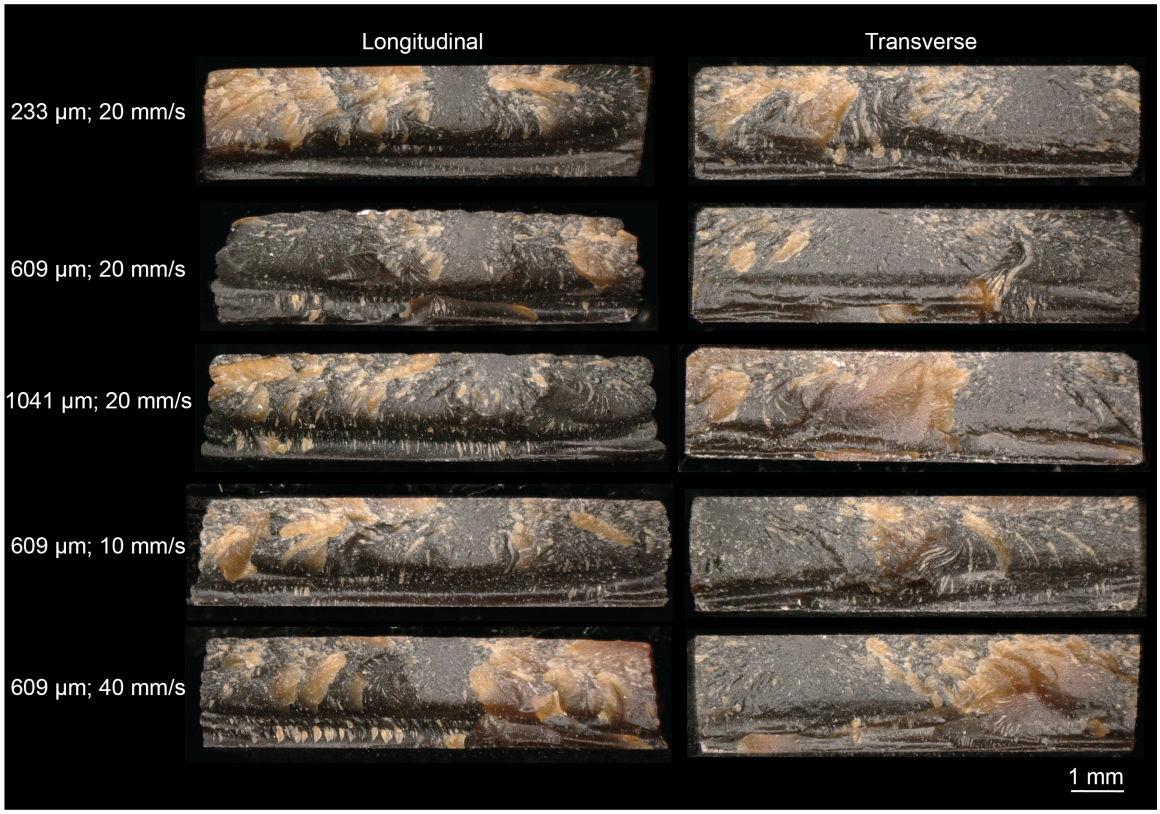

Figure A.7: Optical micrographs of representative fracture surfaces for longitudinal and transverse flexural specimens printed with the NC ink at varying nozzle sizes and print speeds. These micrographs demonstrate that all prints with different combinations of nozzle size and print speed yield fully-dense parts without any intrafilamentary voids, providing that the extrusion pressure was chosen appropriately. There is no evidence of the original print path or any delamination between layers, indicating complete coalescence and strong adhesion between printed filaments.

A.7 Polarized optical microscopy (POM) of epoxy/fumed silica 3D-printed composites

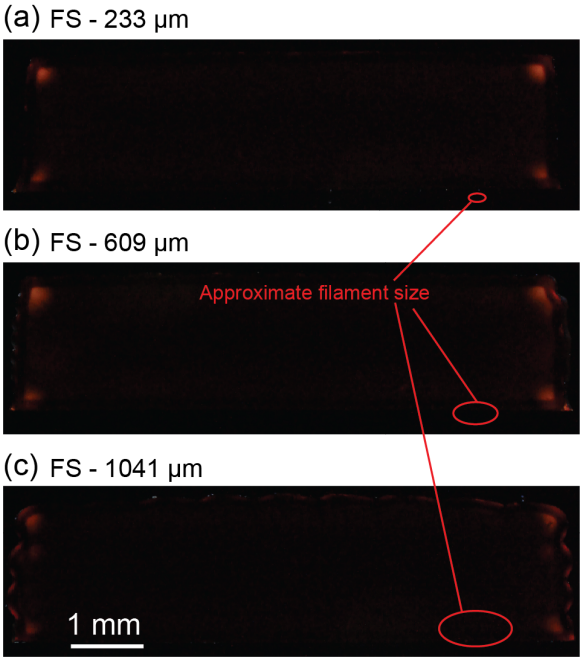

Figure A.8: Representative optical transmitted light micrographs of polished thin slices (<1 mm thick) cut from printed specimens containing FS filler, observed using crossed polarizers. Specimens printed with nozzle diameters of (a) 233 μm, (b) 609 μm and (c) 1041 μm. These printed FS specimens do not exhibit any birefringence whatsoever, regardless of nozzle size. The approximate filament size is indicated by the red oval, which corresponds to the size of nozzle used for printing. The axis of the printed filaments is normal to the plane of the image.

A.8 Annular average of 2D scattering pattern

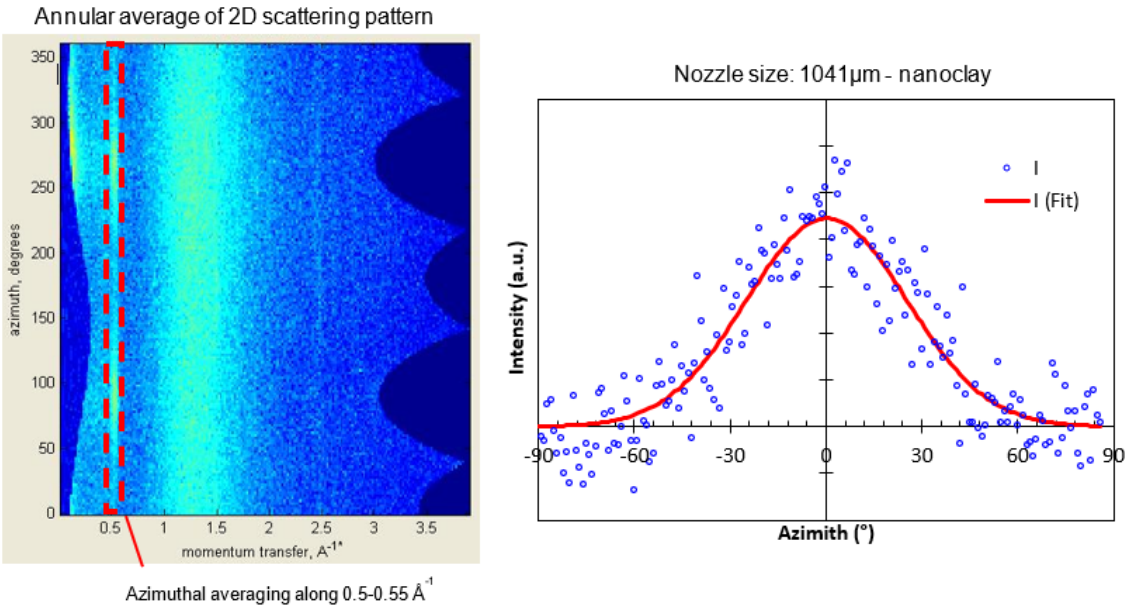

Figure A.9: Representative fit of scattering intensity between 0.5 $\mathring{A}^{-1} < q < 0.55$ $\mathring{A}^{-1}$ as a function of azimuthal angle. Scattering data were fit using a Gaussian function centered about 0°.

A.9 Scanning electron microscopy of carbon fiber bundles

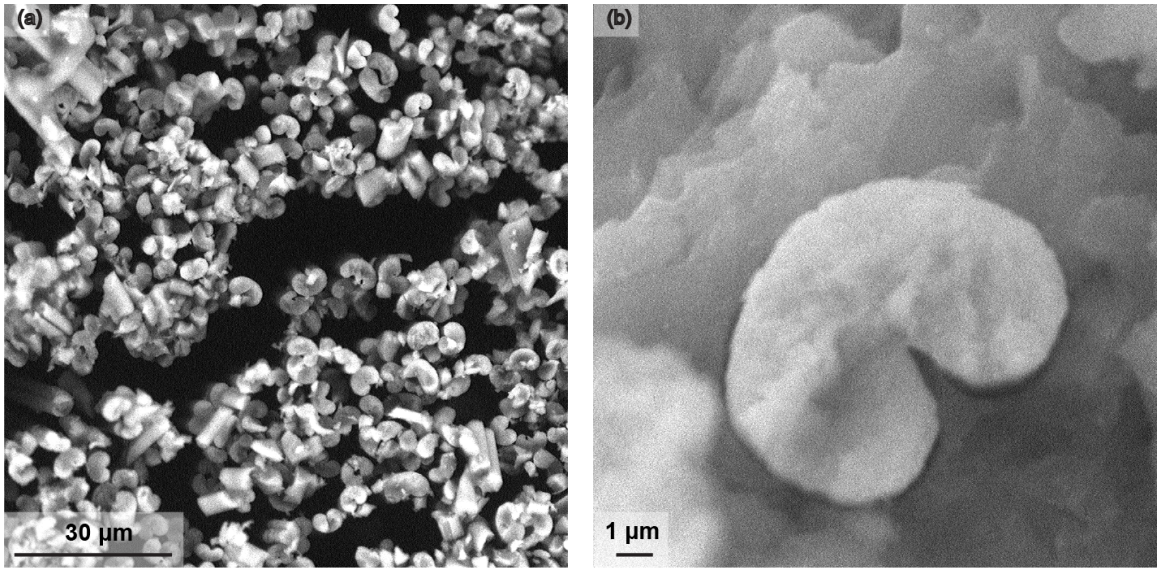

Figure A.10: SEM micrographs of the chopped carbon fibers used in this study. (a) Carbon fiber bundles and (b) single carbon fiber in the printed composite.

A.10 Fiber length measurements

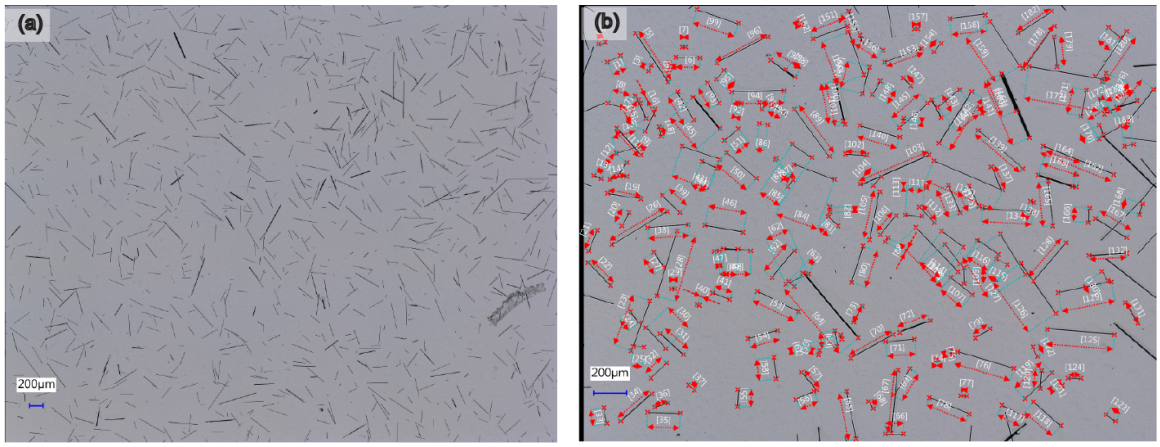

Figure A.11: (a) Distributed carbon fibers after centrifugal planetary mixing and diluting in acetone. (b) Fiber length measurements in optical microscopy.

A.11 Extrusion pressure values – Chapter 5

Table A.3: Extrusion pressure values for the NC/CF ink at different mixing time and print parameters

Mixing time (seconds)	Nozzle size (mm)	Print speed (mm/s)	Extrusion pressure (psi)
180	0.864	40	172*
360	0.864	40	70
540	0.864	40	65
720	0.864	40	60
720	0.864	20	50
720	0.609	40	63
720	1.041	40	58
720	1.041	10	45

*Extruded via a 4x pressure multiplier (HP3, Nordson EFD, Westlake, OH) was used for this ink.

A.12 Density of printed epoxy/CF/NC composites vs. mixing time

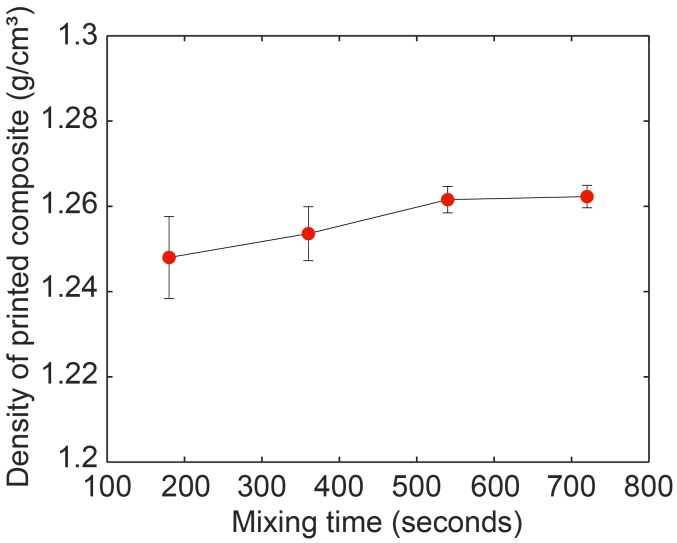

Figure A.12: Density measurements of the 3D-printed and cured CF/NC composites (9.15 vol.% CF).

A.13 Weibull fit parameters

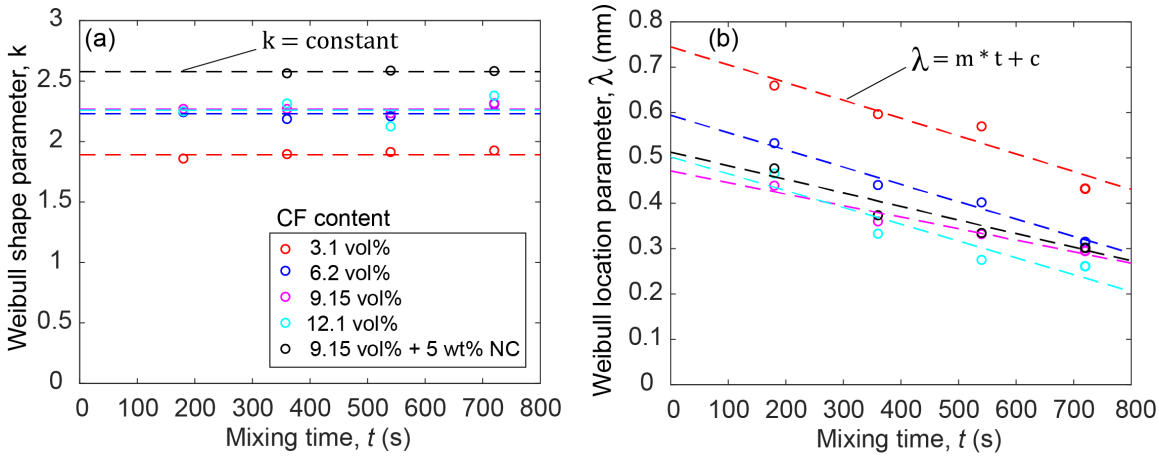

Figure A.13: (a) Weibull shape parameter (k) as a function of mixing time, and (b) Weibull scale parameter, λ, as a function of mixing time. Dashed lines represent the linear regression of each dataset.

A.14 Linear fitting parameters for the plots in Figure A.13– Chapter 5

Table A.4: Linear fitting parameters for the plots in Figure A.13

CF content (vol%)	k	m	c
3.1	1.89	0.00039	0.745
6.2	2.23	0.00038	0.594
9.15	2.27	0.00025	0.471
12.1	2.26	0.00037	0.502
9.15 + 5 wt% NC	2.55	0.00030	0.513

A.15 Anisotropy master curves

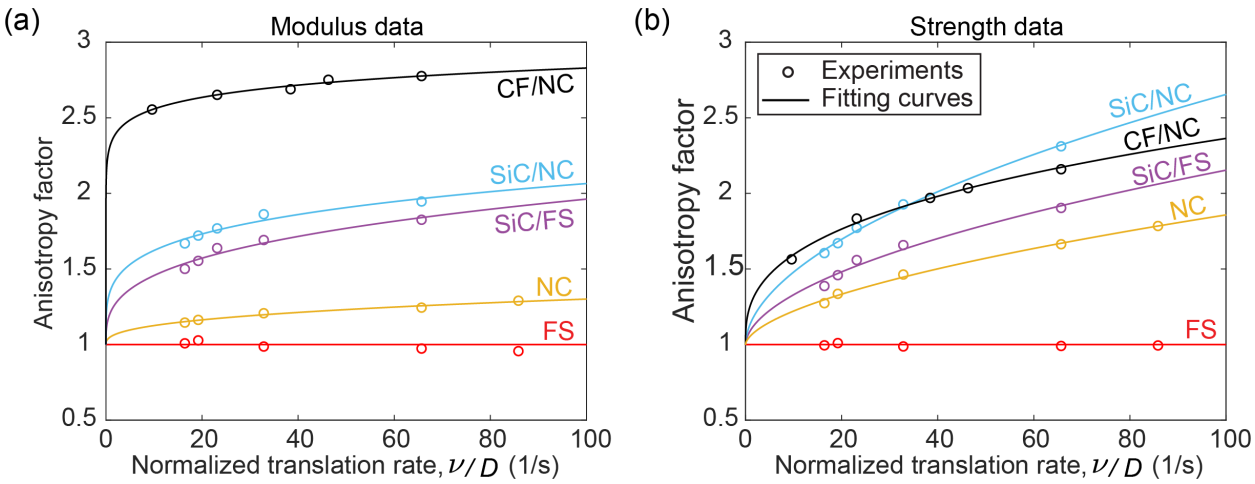

Figure A.14: Master curves of mechanical anisotropy as a function of ν/D ratio in (a) modulus and (b) strength for epoxy-filled material systems.

A.16 Fiber orientation distribution (FOD)

Table A.5: Fiber orientation, fiber count and relative frequency distribution in printed NC/CF composites printed at $\nu/D = 9.6$ s^{-1} and $\nu/D = 65.7$ s^{-1}.

	$\nu/D = 9.6$ s^{-1}		$\nu/D = 65.7$ s^{-1}	
Orientation angle (degrees)	Fiber count	Frequency (%)	Fiber count	Frequency (%)
0 – 10	3147	50.63	23074	83.58
10 – 20	2106	33.88	2433	8.81
20 – 30	569	9.15	466	1.69
30 – 40	160	2.57	368	1.33
40 – 50	78	1.25	362	1.31
50 – 60	48	0.77	288	1.04
60 – 70	33	0.53	225	0.81
70 – 80	37	0.60	223	0.81
80 – 90	38	0.61	169	0.61

Vita

Nadim Saleh Hmeidat was born in Jerusalem, the capital of the State of Palestine. Nadim received a bachelor of science in Mechatronics Engineering from An-Najah National University (NNU) in Palestine in 2013. Upon completion of undergraduate studies, he moved to the U.S. to purse higher education. In 2016, Hmeidat enrolled in the PhD program in the Mechanical, Aerospace and Biomedical Engineering department at the University of Tennessee where he received a research assistantship in the research group of Assistant Professor Brett G. Compton to conduct research in the area of material extrusion additive manufacturing. Nadim's main research focus has been on the development of printable epoxy-based feedstocks, specifically for direct ink writing (DIW), as well as understanding relationships between process parameters, filler orientation, and mechanical properties of the resulting 3D-printed composites. Continuing his graduate studies, Nadim received his concurrent Masters of Science degree in Mechanical Engineering in 2017, and advanced to doctoral candidacy in Spring 2019. Nadim got married to his beautiful wife, Rufaida, in January 2017, and two years later, their first rainbow son, Eyas, was born. In October 2020, Nadim accepted a Post-Doctoral Research Associate position in the laboratory of Professor Mark Dadmun at the University of Tennessee and Oak Ridge National Laboratory to conduct research in the area of reactive material extrusion additive manufacturing. After receiving his Ph.D in the Spring of 2021, Nadim will continue his passion for research as a Postdoctoral Associate in Dadmun's group.